CHARACTERIZING A NEUTRON ENERGY SPECTRUM USING A "FORWARD EDGE" NEUTRON TIME-OF-FLIGHT SPECTROSCOPY TECHNIQUE

THESIS

Jeffrey S. Spear, Major, USA

AFIT/GNE/ENP/05-14

DEPARTMENT OF THE AIR FORCE
AIR UNIVERSITY

AIR FORCE INSTITUTE OF TECHNOLOGY

Wright-Patterson Air Force Base, Ohio

APPROVED FOR PUBLIC RELEASE; DISTRIBUTION UNLIMITED

AFIT/GNE/ENP/05-14

CHARACTERIZING A NEUTRON ENERGY SPECTRUM USING A "FORWARD EDGE" NEUTRON TIME-OF-FLIGHT SPECTROSCOPY TECHNIQUE

THESIS

Presented to the Faculty

Department of Engineering Physics

Graduate School of Engineering and Management

Air Force Institute of Technology

Air University

Air Education and Training Command

In Partial Fulfillment of the Requirements for the

Degree of Master of Science (Nuclear Science)
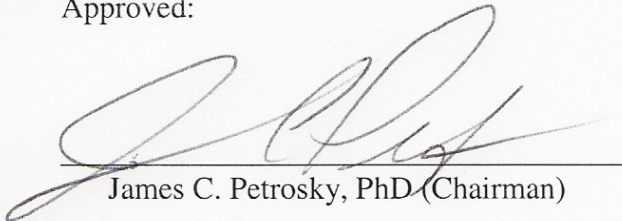
Jeffrey S. Spear, BS

Major, USA

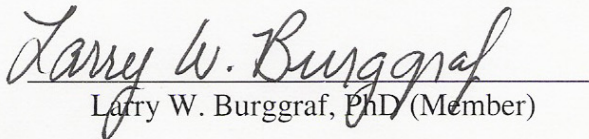March 2005

AFIT/GNE/ENP/05-14

CHARACTERIZING A NEUTRON ENERGY SPECTRUM USING A "FORWARD EDGE" NEUTRON TIME-OF-FLIGHT SPECTROSCOPY TECHNIQUE
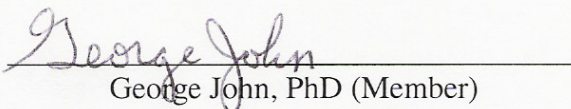
Jeffrey S. Spear, BS
Major, USA

Approved:

_____
James C. Petrosky, PhD (Chairman)

O9MAR05
date

_____
Larry W. Burggraf, PhD (Member)

9 Mar '05
date

_____
George John, PhD (Member)

9 March 2005
date

AFIT/GNE/ENP/05-14

Abstract

The ability to identify a neutron-emitting source through passive interrogation is an area of great interest to various governmental agencies responsible for the security of this nation. Furthermore, the ability to characterize the neutron-emitting source as special nuclear material (SNM) would provide a significant tool in the arsenal of counter-proliferation.

A Fermi-style thermal neutron disc chopper was designed, constructed, and calibrated in conjunction with a boron-loaded organic scintillator for use in creating a *forward edge* neutron time-of-flight spectrometer. The *forward edge* neutron time-of-flight spectroscopy technique will be able to infer the characteristics of a neutron energy spectrum. The system analyzed the spectrum of a moderated and unmoderated PuBe source with the aid of a MATLAB code.

Through the use of pulse shape analysis techniques and energy spectroscopy the thermal neutron capture event was identified and isolated. Data analysis provided positive feedback in the disc chopper's ability to partially attenuate higher energy neutrons in the PuBe spectrum. The analyzed data from the MATLAB code indicates the *forward edge* neutron spectroscopy technique works; however, in terms of an application useful for passive interrogation the system's low efficiency and cumbersome size prove too prohibitive.

To My Wife

Acknowledgments

I would like to express my sincere appreciation to my faculty advisor, Dr. James Petrosky, without whom this effort would have never succeeded. His broad knowledge base, subtle reassurance, and continuous interaction provided the necessary guidance to see this endeavor from start to finish.

The efforts of my thesis committee members are also greatly appreciated. Dr. Larry Burggraf provided helpful suggestions in working with the various electronics and the analysis of their outputs. His continuous interest and concern in the progress of this experiment were duly noted. Dr. George John, a prominent figure in this field, offered excellent direction and guidance. I am particularly grateful for his taking time away from his other responsibilities as a professor emeritus.

The fabrication of various components would not have been possible without the expert skills of the men in the AFIT fabrication shop, thus I'd like to offer my sincere appreciation to Condie Inman, Robert Jarusiewic, and Jan LeValley.

Foremost, I want to offer my utmost gratitude to my family. My wife and children made the very best of my absences as a husband and father. I love you all and cannot capture in words the appreciation I wish to express to you for your support, encouragement and patience.

Jeffrey S. Spear

Table of Contents

Page

List of Figures

x

List of Tables

List of Symbols

Symbol	Description	Unit
θ or φ	Angle	° or radians
E_p	Proton Energy	eV
E_n	Neutron Energy	eV
$Q(t)$	Time Dependent Neutron Flux	n/cm^2-s
a_x	Average Neutron Yield Per Alpha Particle for isotope x	n/α
λ_x	Decay Constant of Isotope x	1/s
N_x	Number of Atoms of Isotope x	unitless
σ	Microscopic Cross-section	cm^2 or barn
I	Time Independent Neutron Flux	n/cm^2-s
x	Absorber Thickness	cm
Σ	Macroscopic Cross-section	1/cm
N_0	Avogadro's Number	atoms/mole
A	Atomic Weight	gm/mole
λ	Mean Free Path	cm
ω	Angular Velocity	radians/s
Ω	Solid Angle	steradians
a	Radius of Detector	cm
s	Radius of Source (axial radius)	cm
d	Distance from Source to Detector	cm
ε_{abs}	Absolute Efficiency	See Eq (11)
ε_{int}	Intrinsic Efficiency	See Eq (12)
R_1	Radius of Disc Chopper	cm
r_0	Radius of Hole in Disc Chopper	cm
ψ or ξ	Angle	See Figure 11
c	Speed of Light	m/s
E_0	Rest Mass of Neutron	MeV/c^2
ΔQ_{Max}	Maxium Energy Transferred in Collision of nuclei	MeV
m	Mass of Stationary Nucleus	MeV/c^2
$h\nu$	Incident Gamma Energy	MeV
$m0c2$	Rest Mass of Electron	MeV

List of Abbreviations

Abbreviation	Description
TOF	Time-of-flight
α	Alpha Particle (He+)
n	Neutron
DoD	Department of Defense
DTRA	Defense Threat Reduction Agency
WMD	Weapon of Mass Destruction
SNM	Special Nuclear Material
eV	Electron Volt
MCNP	Monte Carlo N-Particle
Ci	Curie
PuBe	Plutonium-Beryllium
$\beta-$	Beta Particle (electron)
γ	Gamma Particle
p	Proton
f	Fission
RPM	Revolutions Per Minute
S_x	x^{th} Singlet State
T_x	x^{th} Triplet State
H^+	Proton Recoil
Li^+	Ionized Lithium Nucleus
LET	Linear Energy Transfer
eVee	Electron Volt Electron Equivalent
PSA	Pulse Shape Analysis
HV	High Voltage
PMT	Photomultiplier Tube
pF	Picofarad
DLA	Delay Line Amplifier
DLA (P)	Delay Line Amplifier – Pulse Shape Analysis Branch
DLA (E)	Delay Line Amplifier – Energy Branch
TSCA	Timing Single-Channel Analyzer

LLD	Lower Level Discriminator
ULD	Upper Level Discriminator
TAC	Time-to-Amplitude Converter
MCA	Multi-Channel Analyzer
ADC	Analog-to-Digital Converter
AIM	Acquisition Interface Module
NIM	Nuclear Instrumentation Module
LG&S	Linear Gate and Stretcher
VaryAC	Variable Autotransformer
MATLAB	Matrix Laboratory

CHARACTERIZING A NEUTRON ENERGY SPECTRUM USING A "FORWARD EDGE" TIME-OF-

FLIGHT NEUTRON SPECTROSCOPY TECHNIQUE

I. Introduction

Background

Since the discovery of the neutron by James Chadwick in 1932, a host of experiments have been

conducted to determine the energy spectra of different neutron sources. A number of different

spectrometers have been developed over the years; however, only a few have covered a sizable enough

spectrum of energy to be practical. The time-of-flight (TOF) system, which measures the time it takes the

neutron to travel from point A to point B, has emerged as the premier choice for determining the energy

spectrum. Theoretically this system can provide the energy spectrum of any source, such as that emitted by

spontaneous fission, by an (α,n) reaction, or by any number of nuclear reactions; however, in practice, as

will be shown, this technique has limiting constraints. Given the time of travel for a fixed distance, the use

of kinematics yields the energy of a neutron for this method.

Motivation

With the events that unfolded on September 11, 2001, the United States Government fully realized

the coordinated efforts of a terrorist attack within U.S. borders. All levels of public office up to and

including the President of the United States immediately implemented plans to help thwart any further

immediate attacks, while outlining broad changes that would prevent future attacks. In his 2002 State of the

Union Address President Bush stated:

> Time and distance from the events of September the 11th will not make us safer unless we act on
> its lessons. America is no longer protected by vast oceans. We are protected from attack only by
> vigorous action abroad, and increased vigilance at home. [We must] prevent regimes that sponsor
> terror from threatening America or our friends and allies with weapons of mass destruction
> [through a] sustained strategy of homeland security focus[ing] on four key areas: bioterrorism,
> emergency response, airport and border security, and improved intelligence. [1]

President Bush not only created the new Office of Homeland Security, but increased the budget and streamlined other already established Department of Defense (DoD) offices. One such office, the Defense Threat Reduction Agency (DTRA), "safeguards America's interests from weapons of mass destruction (WMD's) by controlling and reducing the threat and providing quality tools and services for the warfighter". [2] In addition, DTRA has the mission to monitor and verify treaty compliance for the United States. [3:27] One of DTRA's crucial research areas is in the area of passive or active identification of special nuclear material (SNM) such as Uranium-235 or Plutonium-239. Special Nuclear material lies at the heart of every nuclear weapon *pit*.

The ability to detect SNM has several applications, two of which include border security and treaty verification. The detection of SNM at the point of entry to the U.S., whether that be via vehicle, rail, or ship, must occur efficiently and reliably to ensure minimal economic disruption and preclude *false positive* identification. The second application requires the ability to verify treaty compliance through no obtrusive means. The current method entails verification through gamma detection, which can be more readily faked or *spoofed* than neutron detection. Again, however, the method of neutron detection must be both reliable and efficient.

Uranium-235 and Plutonium-239 are both members of the actinide family and have a unique radioactive decay known as *spontaneous fission* whereby the nucleus spontaneously splits into fission fragments, neutrons and gammas. Although the half-lives for spontaneous fission for Uranium-235 and Plutonium-239 are 1.9×10^{17} years and 5.5×10^{15} years, respectively, the volume of SNM required for a weapon's pit, and thus the number of atoms present, produces a measurable number of neutrons to be passively detected by a neutron detector. [4:35] In addition to their ability to spontaneously decay, the above SNM have high fission cross-sections and thus produce fission fragments, neutrons and gammas when bombarded with neutrons. This form of active detection provides a much higher flux of neutrons than spontaneous fission alone, which can thus be detected by a neutron detector. The flux of neutrons by the SNM is not enough information, as other industrial and medical isotopes such as Californium-252 and Curium-245 can provide the same results given active or passive detection, thus providing a false positive.

2

However, the flux of neutrons by energy provides a characteristic signature, as shown in Figure 1 below, and thus the energy of the neutrons must be determined. In particular, the features in Figure 1 from thermal energies up to 1 keV can provide useful information not only about the type of SNM, but also about the geometric configuration of the weapon's pit.
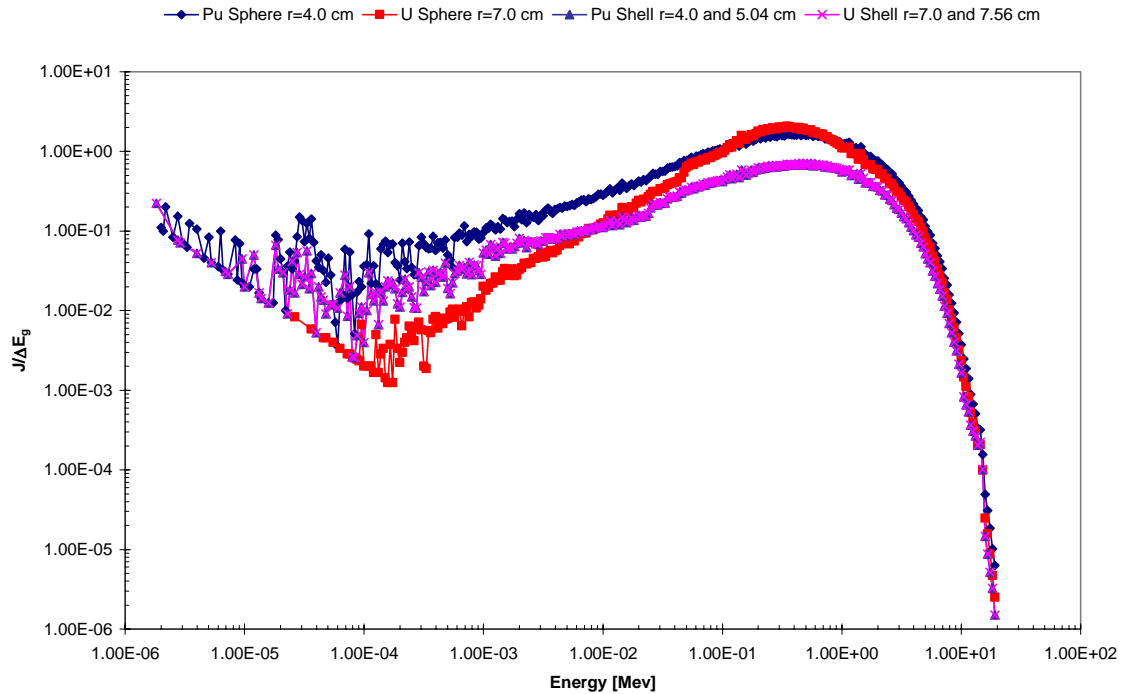
Figure 1: Neutron leakage spectra from outer surface of Pu-239 and U-235 spheres and shells [5]

Current Knowledge

Neutron detection and spectrometry is one means of identifying SNM, but neutrons are elusive particles. Neutrons live up to their name in that they are neutral in charge and therefore do not leave a well-documented signature. Protons, beta particles, and alpha-particles, on the other hand, are heavy charged particles that provide a well defined signature through the effects of columbic interaction. Adding even more difficulty to the task of detection is that neutron energies can span over 14 decades (10^{-6} to 10^{8} eV) of energy as evidenced from the neutron leakage spectra of the SNM in Figure 1 above. Because the cross-section for neutron interactions in most materials is a strong function of neutron energy, rather different techniques have been developed for neutron detection in different energy regions.

Most present day neutron detection and spectrometry methods fall under one of the four following categories:

1. measurement of the energies of charged particles produced by neutron interactions, e.g., nuclear emulsions, damage track detectors, recoil proton telescopes, proportional counters, sandwich spectrometers, lithium glass scintillators, and organic scintillators; [6:126]

2. measurement of the flight time of neutrons over a given distance, e.g., Time-of-Flight (TOF) spectrometers; [7:541]

3. measurement of attenuation and moderation of neutrons in various thicknesses of hydrogenous material, e.g. Bonner spheres; [8:95] and

4. measurement of activation or fission reactions in a set of detectors having different energy responses, e.g., threshold detectors or activation foils. [9:749]

The energy spectrum covered by some of the aforementioned detectors is depicted in Figure 2 below.
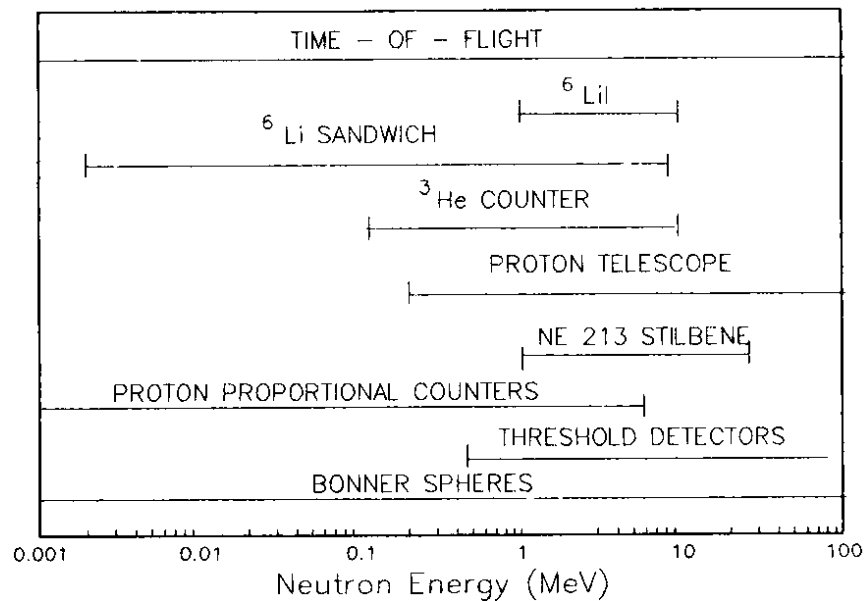
Figure 2: Energy Ranges for Neutron Spectrometers [10:13]

Examining the lower energy neutron detectors, the proportional counter spans a large portion of the lower energy spectrum. One of the more favored proportional detectors for slow neutrons is the BF_3 proportional tube. Boron-trifluoride serves both as the target for slow neutron conversion into secondary particles as well as a proportional gas. In most commercial detectors, the gas is highly enriched in ^{10}B,

4

resulting in efficiency much higher than if the gas were comprised of naturally occurring boron. The ^{10}B reaction for the conversion of slow neutrons into directly detectable particles is the ^{10}B(n,α) reaction, which may be written as

$$^{10}_{5}B + ^{1}_{0}n \rightarrow \begin{cases} ^{7}_{3}Li + ^{4}_{2}\alpha \\ ^{7}_{3}Li* + ^{2}_{4}\alpha \end{cases}. \tag{1}$$

Because the Q-value of this reaction is so large (e.g. 2.792 MeV ground state and 2.310 MeV excited state) compared with the incoming energy of the slow neutron (e.g. thermal), all information about the neutron energy is lost, thus the proportional counter is simply that…a counter. [9:517] Although fast neutrons (i.e. > 0.5 MeV) can be counted by producing recoil nuclei in the proportional gas, it is a far less likely reaction than the thermal capture by ^{10}B and thus proportional counters are not especially suited for fast neutrons. In principle, any slow neutron detection system could be applied to detecting fast neutrons; however, the probability that a neutron will interact by one of these (n,α) reactions decreases rapidly with increasing neutron energy as shown in Figure 3. As a result, BF$_3$ tubes have extremely low detection efficiencies for *unmoderated* fast neutrons and thus are almost never used for this purpose. Instead an entirely different detection scheme is required.
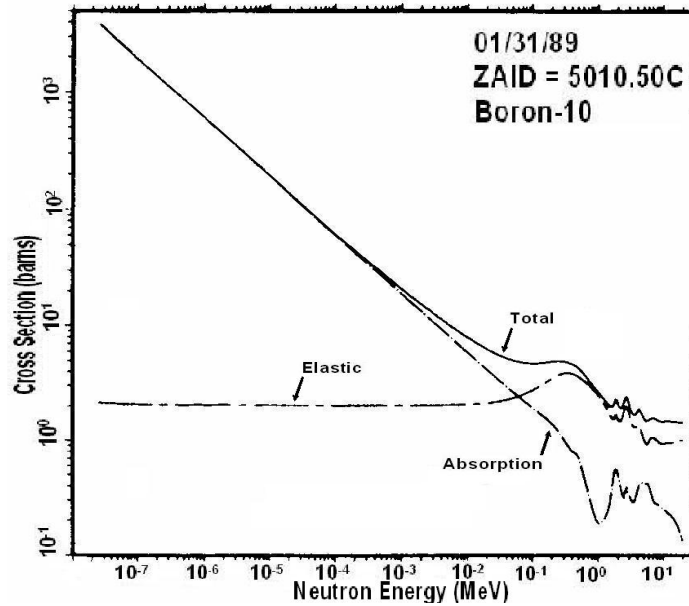
Figure 3: Boron-10 total, elastic, and absorption cross-sections for neutrons [11:37]

5

The most important additional conversion process useful for detection of fast neutrons is elastic neutron scattering. In this interaction the incident neutron transfers part of its kinetic energy to the scattering nucleus, yielding a *recoil nucleus*. The scattering nucleus is typically one of a hydrogenous material since hydrogen has a relatively high scattering cross-section and is also capable of reducing the neutron energy to zero in only one collision. The slow neutrons transfer very little energy to the recoil nucleus, and thus the recoil nucleus is too low in energy to generate a usable signal. Because of this inadequacy, proton recoil detectors are only useful at neutron energies above 100 keV as noted in Figure 2.

An important aspect present in fast neutron detectors is the ability to discern the energy of the incoming neutron. Slow neutron detectors can provide no information about the neutron's initial energy due to the overwhelming energy released in the nuclear interaction (i.e. Q-value); however, as neutron energies increase (e.g. 10-100 keV), the energy of the reaction products begins to change. An accurate measurement of the reaction product energies can then, in principle, be used to deduce the incoming neutron energy. The target nuclei are essentially at rest, and thus the sum of the kinetic energies of the recoil nucleus and scattered neutron must equal that of the initially incident neutron [9:553]. If the proton recoil energies are measured irrespective of direction (e.g. 4π steradians), then the spectrum of the recoil protons must be determined with the aid of a computer program; however, an improvement can be made by observing only those protons that recoil in a particular direction, which is typically close to 0° [7:539]. When observations of a fixed angle are used, the device is known as a proton recoil telescope and the energy of the recoil proton observed at an angle θ with respect to the incident neutron direction is given by

$$E_p = E_n \cos^2 \theta. \qquad (2)$$

In addition to its limitations of determining the energy of only high energy neutrons and their corresponding protons ejected at a fixed angle, the proton recoil telescope can only be applied to a collimated source where the direction of the incident neutron is known.

Two types of neutron detectors have been examined from Figure 2 above; however, in both cases the detectors were limited to either high or low neutron energy ranges. The detector required to discern the flux of broad neutron energies depicted in Figure 2 requires the ability to observe all energies

6

simultaneously. The Bonner Sphere and time-of-flight (TOF) detector are both detectors which span the entire neutron energy spectrum.

The Bonner Sphere is based on the use of hydrogenous material in slowing down or *moderating* the neutron prior to detection. By surrounding a slow neutron detector, such as the BF_3 proportional tube or similar ^{3}He proportional counter, with a few centimeters of hydrogenous material such as polyethelene, the slow neutron detector can become a quite efficient fast neutron detector. The incident fast neutrons lose a fraction of their energy through the collisions with the hydrogen nuclei prior to reaching the detector, thus the lower energy neutron *observes* a larger absorption cross-section and the detector efficiency is increased. Increasing the moderator thickness increases the number of collisions made by the neutron prior to reaching the detector; however, increasing the moderator also decreases the detector volume-to-moderator volume ratio. A decrease in this ratio means the neutron has a lower probability of reaching the detector and thus a lower probability of being counted. Furthermore, a neutron may be absorbed within the thicker moderating material prior to reaching the detector. Due to the ability to fabricate any thickness of moderator, the Bonner Sphere has the ability to detect neutrons across the entire energy spectrum, but through the process of moderation, any information about the neutron's initial energy, less its minimum energy, are lost prior to detection.

The ideal neutron spectrometer for measuring the energy of the neutron flux along its entire spectrum comes in the form of the TOF neutron spectrometer. The TOF spectrometer measures the flight time of a neutron between two fixed points. There are a number of variations of TOF spectrometers; however, the principle is generally the same. Neutrons are pulsed out of the source by means of pulsing the source itself, as in a pulse generator or neutron cannon, or by pulsing the stream of neutrons from a source with a *chopping* mechanism, such as a rotating disc. Using either one of the methods, the start and stop time of the neutrons flight time over a fixed distance is measured. This time is collected and the time spectrum converted into the energy spectrum of the neutron source.

The initial high expense and difficult operating requirements of the pulse generator led to the development of the *disc chopper* method. The original *disc chopper* or *Fermi chopper*, named after its inventor, Enrico Fermi, consisted of a multiple sandwich of aluminum and cadmium foils which fit tightly

into a steel cylinder about 1½ inches in diameter as noted in Figure 4. The cylinder, driven by a Dumore grinder motor, rotated at speeds up to 15,000 RPM, thus allowing bursts of neutrons to go through the aluminum channels. The neutron gate was open for an interval of 5.4°. The spinning cylinder was viewed with two photocells, one giving a direct measure of the rotation and the other sending to the neutron detector a signal used for the measurement of the TOF of the transmitted neutrons. Four BF_3 filled proportional detectors were used as the neutron detector. A nest of four detectors was connected in parallel and mounted 146 cm from the shutter. A ½" thick layer of boron carbide provided the necessary shielding from background neutrons for the detectors [12:194]. Fermi's chopper, however, was a "slow" chopper and functioned only in the presence of thermal neutrons collimated from a graphite pile.
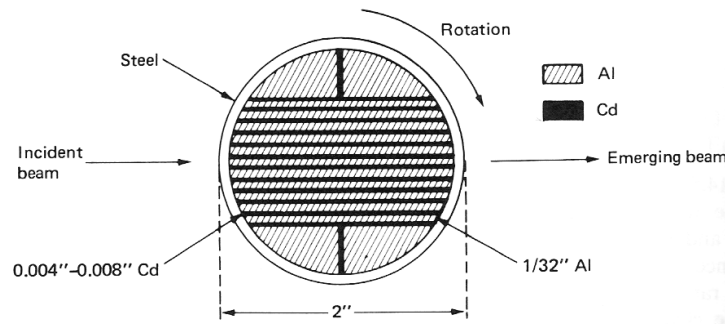
Figure 4: The Fermi chopper

Another variation of the Fermi chopper is the *multi-chopper* as shown in Figure 5 below. The multi-disc chopper uses two or more discs separated by a fixed distance. The discs have slits that are slightly offset and rotate at a known angular frequency. All neutron energies pass through the slit of the first disc, thus providing a pulsed source. Neutrons residing in a specific energy range traverse the fixed distance in the appropriate time to pass through the slit of the other rotating disc. Those neutrons traveling faster (more energetic) arrive at the second disc before the opening has arrived are therefore moderated or attenuated. Neutrons moving too slowly meet the same fate. The first downfall to this system resides in its ability to only permit the observation of a discrete neutron energy flux for each set angular shift of the respective slits, thereby causing immense inefficiency in the application of full spectral analysis. In addition, the requirement for a lengthy flight tube, relative to the energy window and detector resolving time, is a must, which prohibits the packing of this system in a portable configuration.
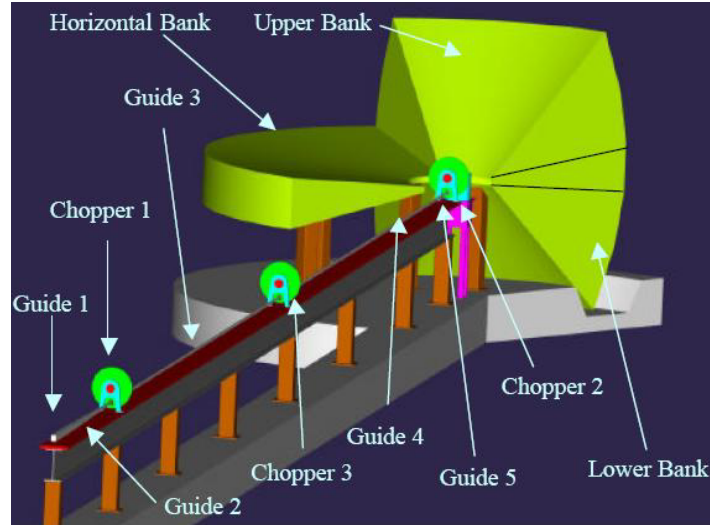
Figure 5: Three-dimensional rendering of a Multi-chopper Spectrometer [13:7]

Problem Statement

Can a thermal neutron disc chopper system be designed, constructed, and calibrated in order to identify the characteristics of a neutron energy spectrum using a *forward edge*$^{\oplus}$ neutron time-of-flight spectroscopy technique?

Hypothesis

The forward edge neutron time-of-flight spectroscopy technique will yield characteristics of the neutron source energy spectrum. Shifts in the thermal neutron flux relative to all neutron energies through adjustments to the amount of moderation present will produce changes in the characteristics of the forward edge TOF spectrum. These shifts allow inferences to be made about the neutron energy spectrum of the source.

Objectives

1. Select an appropriate detector, to include dimensions, based on neutron modeling

---

$^{\oplus}$ The *forward edge* concept considers the arrival of thermal neutrons (i.e. flux) at the detector as a function of time, starting with those corresponding to the neutron gate opening and finishing with the last neutron of interest arriving at the detector.

2. Design and produce a neutron disc chopper system

3. Calibrate the system in terms of timing and detector energy characterization

4. Analyze the data in order to produce a *forward edge* neutron time-of-flight spectrum

5. Determine the viability of the forward edge TOF spectroscopy technique in DTRA related applications.

Scope

This project considers the various aspects of the TOF spectrometer setup, calibration, and use. It entails an understanding of basic neutron physics. Appropriate analysis of microscopic and macroscopic materials properties will be conducted in construction of the disc, its housing mechanism, and surrounding moderation. A detailed analysis of the physical geometry of the setup will be considered. A code will be devised to analyze the collected data. An attempt to improve upon the Fermi Chopper will be made in that the neutron spectrum of interest will include the presence of all energy neutrons, rather than 1 eV neutrons and below. The research effort will be concluded when successful correlation is achieved between the applicable theory, modeling, and experimental measurements.

Approach

The general research approach included theoretical development, modeling, and experimental measurements. The theoretical development continued non-stop throughout the entire project. Modeling of the neutron behavior in various materials consisted of static geometry analyzed with a Monte Carlo Neutron Program (MCNP). The experimental approach consisted of a 5 Curie (Ci) ^{239}Pu-Be source used to test the detector and verify the geometry and electronics. Moderation of the ^{239}Pu-Be source *softened* the high-energy spectrum. The moderated neutron energy of interest was thermal in nature (i.e. ~ 0.0253 eV). A single gate Fermi-style neutron chopper was designed, constructed and calibrated to provide a pulsing of thermal neutrons. The thermal energy lent itself to the limited angular velocity of the disc chopper (i.e. inability to gate out low energy neutrons) and coincidentally took advantage of the most characteristic features of Figure 1. The neutron events were measured using a very sensitive boron-loaded organic scintillator with moderate energy resolution. A system of nuclear instrumentation modules provided the

necessary output to conduct data collection via a fast digital oscilloscope. A small MATLAB code massaged the collected data for final analysis.

Assumptions

A number of assumption were required in order to continue forward during the development of the experimental portion of the thesis effort. These following assumptions apply throughout all discussion and calculations in this document.

1. The *birth date* of the PuBe source is taken as 4/25/61 (See Appendix B)

2. The peak neutron flux in the PuBe spectrum of Figure 6 was 3.1 MeV [14:176].

3. The isotopic concentration of the source is as listed in Appendix B.

4. The 3-phase variable motor maintained a constant angular velocity after initial spin up of the disc chopper assembly.

5. The attenuation/moderation of air was negligible for all neutron energies considered.

6. Thermal neutrons were categorized as those neutrons with energies of approximately 0.0253 eV.

7. The cadmium foil interlaced along the circumference of the disc chopper (See Appendix C) permitted negligible thermal neutron leakage.
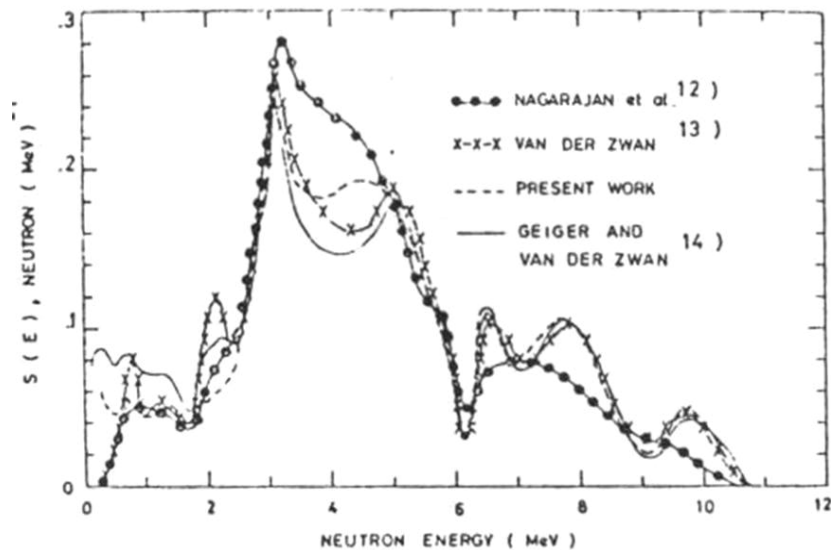
Figure 6: Pu-Be source neutron energy spectrum [14:175]

II. Theory

Chapter Overview

In order to properly conduct a neutron TOF experiment, there are several processes that must be understood. This chapter lays out those methods in detail. The methods covered in this chapter will be referred to throughout the remainder of this document. In order to easily establish these fundamental mechanisms that provide the means to conduct forward edge neutron TOF spectroscopy, it is best to start at the beginning of the chronological chain of events, which in this case is the source of neutrons.

The Neutron Source

The PuBe neutron source used in this experiment produces neutrons through the (α,n) reaction,

$$\,^{4}_{2}\alpha + \,^{9}_{4}Be \rightarrow \,^{12}_{6}C + \,^{1}_{0}n \tag{3}$$

Because energetic alpha particles are available from the direct decay of Pu-239, as well as many other heavy nuclides, fabrication of a small self-contained neutron source is possible by mixing an alpha-emitting isotope with a suitable target material. The neutron yield is maximized when beryllium is used for the target material. The source consists of the stable alloy $^{239}\text{Pu}^{13}\text{Be}$, where the ^{239}Pu is homogenously distributed. The alpha particles, through collisions, lose a variable amount of energy prior to interacting with the beryllium nucleus, thus their continuous energy distribution *washes out* much of the structure that would otherwise be observed from monoenergetic alpha particles. In addition, the various peaks and valleys present in the PuBe source spectrum in Figure 6 can be explained in terms of the various excitation states in which the ^{12}C product nucleus is left [9:22]. Furthermore, this particular type of source (See Appendix A) produces neutrons through not only the (α,n) reaction, but also through secondary processes such as (n,2n) reactions in beryllium and (n,fission) events within the plutonium, all of which introduce some dependence of the energy spectrum on the physical size of the source. These three mechanisms establish the dynamic neutron spectrum observed in Figure 6. Due to its relatively low gamma-ray background, ^{239}Pu is the most widely used of the (α,n) isotopic neutron sources; however, because

approximately 16g of the material is required for 1 Ci of activity, sources a few centimeters in dimension are limited to approximately 10^7 n/s [9:21].

Another interesting feature of the neutron source is its *increase* in radioactivity over time. The neutron flux of a PuBe source increases due to the buildup of ^{241}Am, an alpha emitting member of the actinide family. Americium-241 is produced through the β decay of ^{241}Pu [15:48], which is typically present in a PuBe source in concentrations up to 0.7% [16:142]. Sources typically have initial rates of increase of up to 2% per year; however, the following formula was devised to calculate neutron yields for any time, t, from the date of fabrication:

$$Q(t) = (a_1 \lambda_1 N_1 + a_2 \lambda_2 N_2)(1 + \frac{a_4}{a_1} \frac{\lambda_4 \lambda_3 N_3 (e^{-\lambda_4 t} - e^{-\lambda_3 t})}{(\lambda_1 N_1 + \lambda_2 N_2)(\lambda_3 - \lambda_4)}) \tag{4}$$

where   a = average neutron yield per alpha particle$^{\oplus}$,

λ = the decay constant [1/s], and

N = the number of atoms present at t=0 [16:143].

In Appendix B, the measured flux of the PuBe source on 3/9/1962, the date of receipt, was 9.04×10^6 neutrons/second. Nearly 43.4 years has elapsed since that measurement and the flux has increased to 1.13×10^7 neutrons/second. Thus, the initial reported activity of 5 Ci in 1962 has increased to 6.25 Ci in 2004. As shown earlier in Figure 6, the neutrons emitted from the PuBe source are predominantly fast neutrons with energies greater than 0.5 MeV, thus moderation must be used to slow the neutrons down.

Moderation

Neutrons carry no charge and thus cannot interact with matter by means of the coulombic force, which is the primary energy loss mechanism for charged particles. When a neutron interacts, it is with a nucleus of the absorbing material, in one of two forms: scattering and absorption.

In a scattering reaction, the neutron loses energy and is thereby *moderated* or slowed to a lower energy [9:56]. Scattering can be further subdivided into elastic and inelastic scattering. In the process of

$^{\oplus}$ Subscripts 1,2,3, and 4 refer to ^{239}Pu, ^{240}Pu, ^{241}Pu, and ^{241}Am, respectively

elastic scattering, the struck nucleus receives a portion or all of the neutron's energy in the form of kinetic energy of motion, while the scattered neutron carries away the remainder of the energy. A neutron that undergoes an inelastic scattering event divides its energy in three ways: part of the energy goes towards kinetic energy of the struck nucleus, part into the kinetic energy of the scattered neutron, and part into the excitation of the struck nucleus [17:20]. It is clear from conservation of energy that a neutron will lose a greater fraction of its energy in an inelastic collision than in an _equivalent_ elastic collision. Inelastic scattering takes place with neutrons of sufficiently high energy. In an absorption reaction, the neutron is captured by the struck nucleus. This capture can result in the subsequent emission of a gamma ray (n,γ), a proton (n,p), an alpha particle (n,α), a fission event (n,f), or other reactions such as (n,2n).

The probability of each of the aforementioned interactions is given by the cross-section per nucleus σ_e (elastic), σ_f (fission), σ_c (capture), etc., which is expressed in units of 10^{-24} cm^2, also known as a _barn_. The total cross-section, σ_T, is merely a sum of all possible cross-sections (i.e. $\sigma_T = \sigma_e + \sigma_f + \sigma_c + \ldots$). Cross-sections vary from nuclei to nuclei and depend strongly on neutron energy as shown in Figure 3, the cross-section for Boron-10. If the absorber or moderator is composed of a single type of nucleus, then the transmitted neutron flux is given by the relationship

$$I = I_0 e^{-\sigma_T N x} \tag{5}$$

where   I = the transmitted flux [n/cm^2-s],

I_0 = the incident neutron flux [n/cm^2-s],

N = number of absorber nuclei [1/cm^3],

x = absorber thickness [cm], and

σ_T = total cross-section [cm^2] [17:20].

The product of σ_T and N in Equation 5 is known as the macroscopic cross-section, Σ, and has the dimensions of reciprocal centimeters [cm^{-1}], such that

$$\Sigma = \sigma_T N = \sigma_T \frac{\rho N_0}{A} \tag{6}$$

where ρ = density of absorber [gm/cm^3],

N_0 = Avogadro's number [6.023 x 10^{23}], and

14

A = the atomic number of the absorber [17:20].

It is important to note that Equation 5 is valid only when the absorber is composed of one material and the incident neutrons are monoenergetic. In the case where the absorber consists of a number of different types of nuclei, each will have an effect proportional to its concentration in the absorber and to its total cross-section at a given energy. Thus, Equation 5 may be rewritten as

$$I = I_0 e^{-x(N_1\sigma_1 + N_2\sigma_2 + N_3\sigma_3 + ...)} \tag{7}$$

where N_1 = the number of absorber nuclei of constituent #1 [$1/cm^3$]

σ_1 = the total cross-section of absorber nuclei of constituent #1 at that energy [cm^2] [17:20].

Under *good geometry* conditions, the number of detected neutrons will fall off exponentially with increased moderator thickness.

Another useful piece of information comes from the macroscopic cross-section, Σ. The reciprocal of Σ is the mean free path, also denoted by λ. The mean free path represents the average distance traveled in the absorber before the neutron undergoes one of the possible interactions such as scatter, absorption, etc. The mean free path varies with material and neutron energy and can range from microns to several meters.

The Pulsing Mechanism

After leaving the moderator, these lower energy neutrons continue their path toward the pulsing mechanism. The pulsing mechanism is a solid disc with a hole bored radially through the disc as shown in Figure 7.
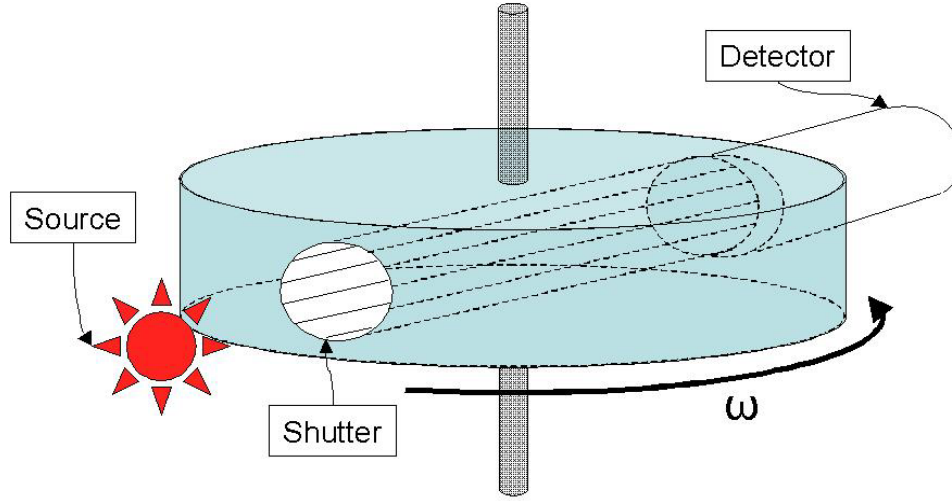
Figure 7: Neutron Chopper Assembly

The disc rotates at an average angular velocity, ω_{avg}. The average angular velocity governs both how often and how long the shutter opens. The average angular velocity (rad/s) is given by

$$\omega_{avg} = \frac{\Delta\theta}{\Delta t} \tag{8}$$

where θ = angle in radians *swept out* by the disc over some time interval, Δt.

The average angular velocity is quickly converted into RPMs as

$$RPM = \frac{60\omega_{avg}}{2\pi} \cdot ^{\oplus} \tag{9}$$

The disc choppers final design considered both the mechanical and nuclear properties of the aluminum alloy used (See Appendices J and I). The disc chopper functions in the same fashion as the moderators discussed above. When the hole of the disc is off axis from the source-detector line of sight, the aluminum both moderates and attenuates the neutrons; however, the mean free path of a *thermal* neutron in aluminum is ~9.65 cm. Due to this lengthy mean free path, the hole bored in the disc will appear much larger to a thermal neutron; therefore, thin pieces of cadmium were added near the circumference of the disc as depicted in Figure 61, Appendix C.

$^{\oplus}$ Equation 9 assumes that the time, t, in Equation 8 is in seconds.

The cadmium foils take advantage of a high neutron absorption cross-section at thermal energies as shown in Figure 8. Thus, from the standpoint of a thermal neutron the *neutron gate* will appear to be the width of the separation of the cadmium foils on each side of the bored hole. The aluminum and cadmium work in tandem; the aluminum moderates higher energy neutrons and attenuates lower energy neutrons, while the cadmium attenuates those neutrons thermalized by the aluminum. The end state results in higher energy neutrons passing through the entire disc chopper mechanism when it is closed and both thermal and higher energy neutrons passing through it when it is open.
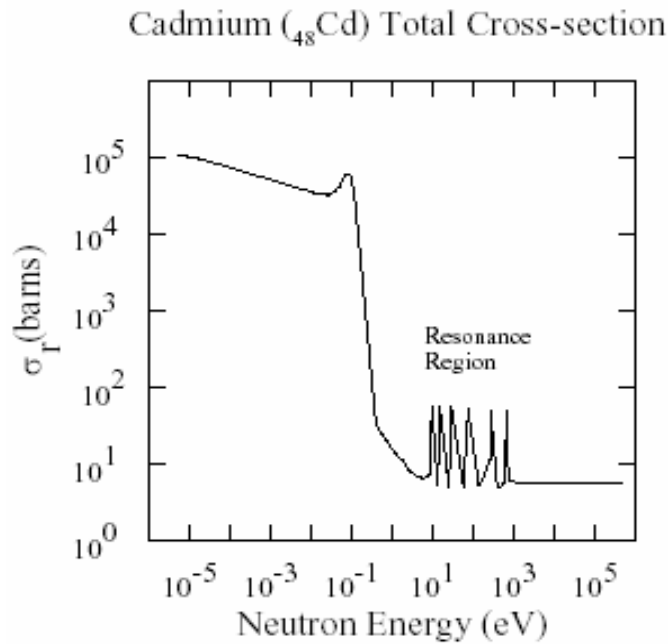
Figure 8: Cadmium-48 total cross-section for neutrons [18]

A shutter opening time can be determined with the use of a light source and photodiode, which produces a start pulse when the disc is 90° off axis from the source-to-detector line of sight. Assuming a constant angular velocity, Equation 5 can be used to determine the time elapsed from the photodiode start pulse until the opening of the neutron gate. Because of the slow angular velocity of the disc coupled with the large neutron gate opening, once a neutron of a given energy has traversed the distance of the neutron tunnel, that energy neutron has the possibility of showing up throughout the remaining neutron gate opening.

In addition to the length of the shutter tunnel, there is an additional space, added from the end of the disc chopper to the face of the detector. This space allows for more spread in the traversing time of the neutrons from the chopper to the detector; therefore, the error associated with the lack of knowledge of where the neutron capture event took place in the depth of the detector decreases.

Further complicating matters is the fact that the exposed area of the detector face changes as the shutter window sweeps across its face. From the neutron reference frame, the face of the detector, as shown in Figure 9 below, appears to wax and wane as the disc chopper rotates.
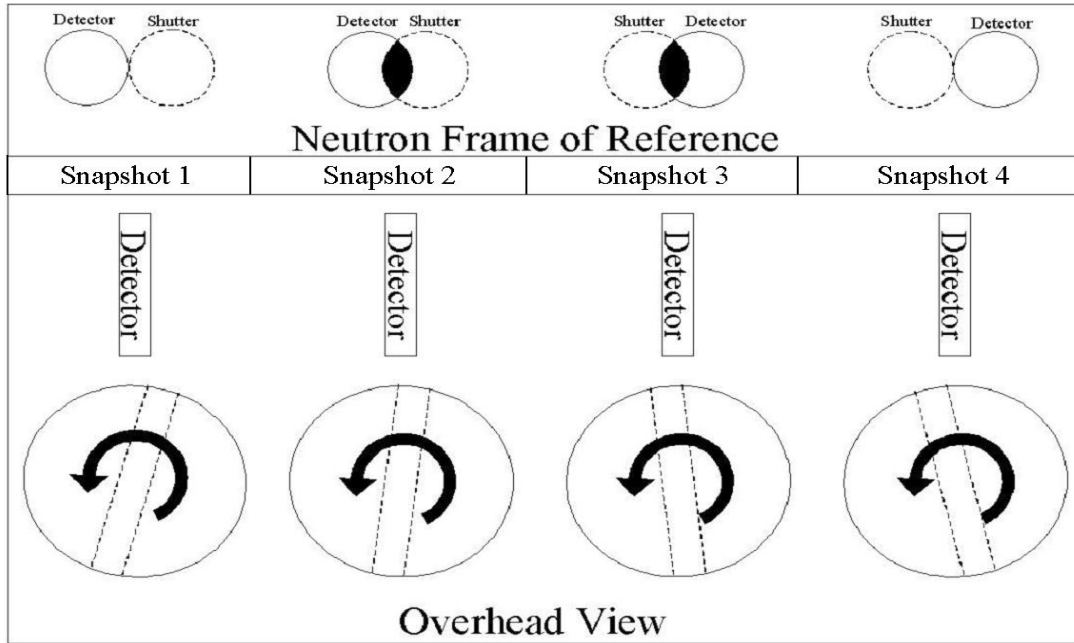
Figure 9: Snapshots of detector-shutter phasing

The area exposed at any given instant directly affects the intrinsic efficiency of the detector through the solid angle, Ω (steradians). The solid angle subtended by the detector from the standpoint of the source is given as

$$\Omega = \frac{4\pi a}{s} \int_0^\infty \frac{\exp(-dk) J_1(sk) J_1(ak)}{k} dk \qquad (10)$$

where a, s, and d are defined as in Figure 10 below [9:119].
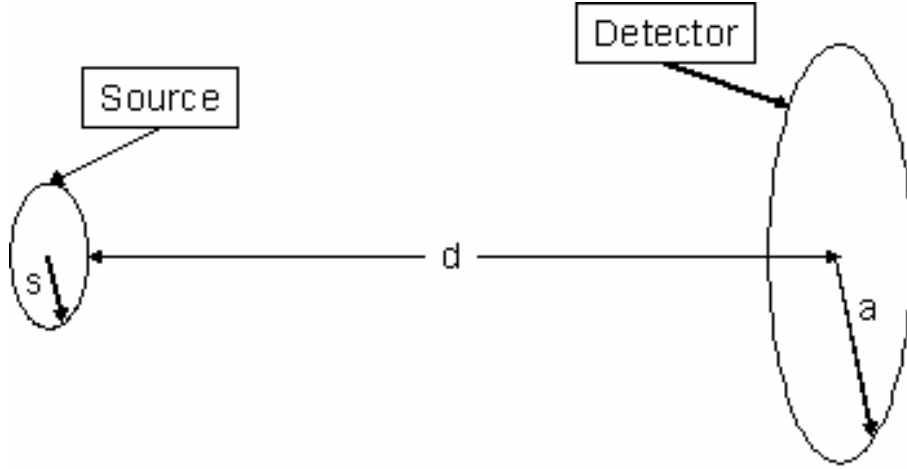
Figure 10: Solid angle subtended by detector [9:118]

The detector efficiency is measured in either absolute efficiency (ε_{abs}) or intrinsic efficicncy (ε_{int}) where

$$\varepsilon_{abs} = \frac{\text{Number of pulses recorded}}{\text{Number of radiation quanta emitted by source}} \qquad (11)$$

$$\varepsilon_{int} = \frac{\text{Number of pulses recorded}}{\text{Number of radiation quanta incident on detector}} \qquad (12)$$

The intrinsic efficiency of the detector is related to the absolute efficiency as

$$\varepsilon_{int} = \varepsilon_{abs}\left(\frac{4\pi}{\Omega}\right) \qquad (13)$$

From Equations 10 and 13 it is obvious that the number of radiation quanta incident on the detector is directly proportional to the area of the detector exposed to the source. Because the area of the detector exposed to the source varies over time, the number of radiation quanta incident on the surface of the detector, and thus the efficiency, will vary in the same fashion.

As shown in Figure 11 the exposed area of the detector is a complicated trigonometric function. In order to deduce the overlapping area (segments) of the shutter and detector, the relationship between the angle (θ) swept out by the rotating disc and the angle (φ) identified by the overlapping segments must first be deduced.

19
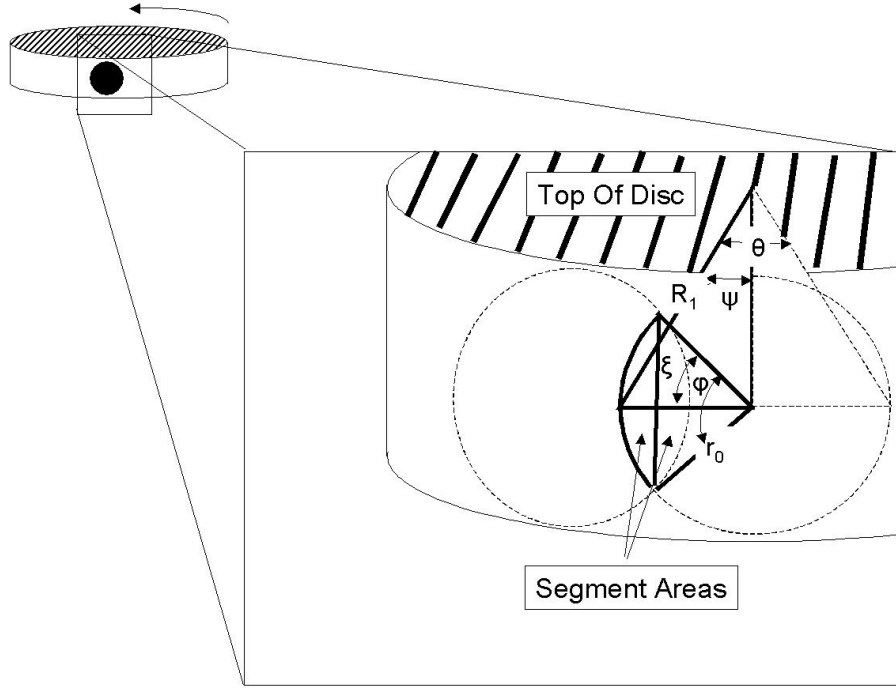
Figure 11: Trigonometric relationship of detector-shutter overlap

As seen from Figure 11 above, a common side of the triangles is related to the angles subtended by

$$R_1 Sin(\psi) = r_0 Sin(\xi) \tag{14}$$

where $\psi = \dfrac{\theta}{2}$ and $\xi = \dfrac{\phi}{2}$.

The area of one segment is given by

$$Area = \frac{1}{2} r_0^{\,2} (\phi - Sin(\phi)) \; , \tag{15}$$

which reduced in the following two steps to

$$Area = r_0 \xi - \frac{1}{2} r_0^{\,2} Sin(2\xi) \text{ and}$$

$$Area = r_0^{\,2} \xi - r_0 Sin(\xi) r_0 Cos(\xi) \; [19{:}125]. \tag{16}$$

Substituting Equation 15 into Equation 16 yields

20

$$Area = r_0{}^2 \xi - r_0 Sin(\xi)R_1 Sin(\psi). \tag{17}$$

Solving for α in Equation 14, then substituting into Equation 17 yields

$$Area = r_0{}^2 ArcCos(\frac{R_1}{r_0} Sin(\psi)) - r_0 Sin(ArcCos(\frac{R_1}{r_0} Sin(\psi)))R_1 Cos(ArcCos(\frac{R_1}{r_0} Sin(\psi))); \tag{18}$$

however, recall that $\psi = \dfrac{\theta}{2}$. The area of both segments, and thus the total area exposed, can now be defined

completely in terms of θ as

$$Area = r_0{}^2 ArcCos(\frac{R_1}{r_0} Sin(\frac{\theta}{2})) - r_0 Sin(ArcCos(\frac{R_1}{r_0} Sin(\frac{\theta}{2})))R_1 Cos(ArcCos(\frac{R_1}{r_0} Sin(\frac{\theta}{2}))). \tag{19}$$

Figure 12 is a graphical representation of Equation 19. As you will recall, given a constant angular

velocity, ω, Equation 8, coupled with Equation 19 allows the area exposed to be mapped out over time.
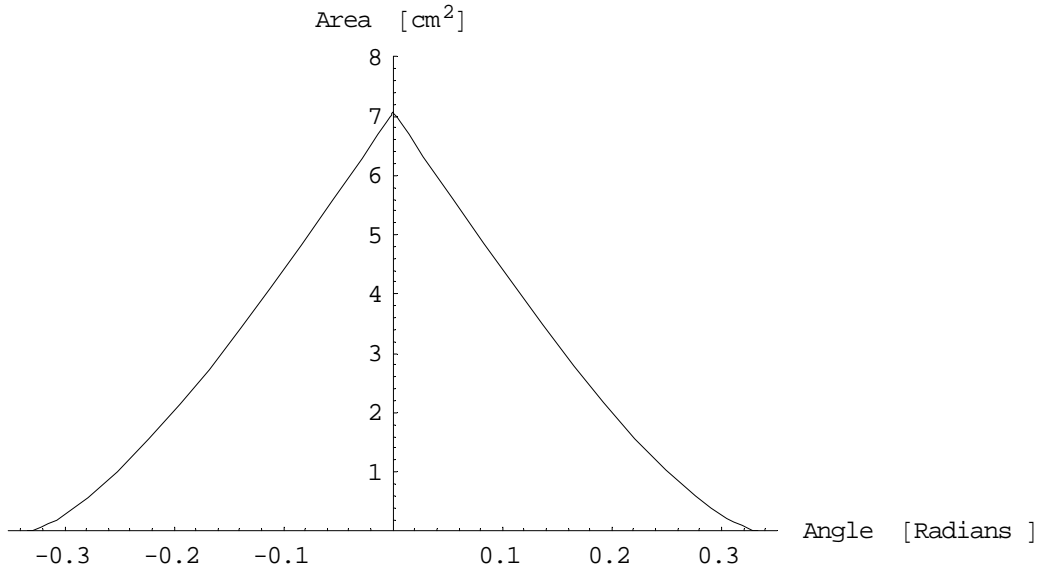
Figure 12: Area of exposed detector versus θ for the rotating disc chopper

Time-of-Flight Calculations

For non-relativistic neutrons, the flight time in seconds from the source end of the shutter tunnel to

the detector is given by the relationship

$$\Delta t = \frac{7.23 \times 10^{-8} d}{E_n^{\frac{1}{2}}} \tag{20}$$

where   d = length of the flight path [m] and E_n = energy of the neutron [MeV].

By determining the values of Δt over a fixed distance d, the energy spectrum for any neutron source can be determined. For neutrons approaching the speed of light, Equation 20 is no longer valid and the kinetic energy of the neutron, E_n, is given by the familiar result of special relativity:

$$E_n = E_0 [(1 - \frac{v_n^2}{c^2})^{\frac{-1}{2}} - 1] \tag{21}$$

where E_0 = rest mass of the neutron or 939.57 MeV/c^2 and c = speed of light (3 x 10^8 m/s) [20:45]. Substituting $v = d/\Delta t$ yields

$$E_n = E_0 [(1 - \frac{d^2}{\Delta t^2 c^2})^{\frac{-1}{2}} - 1] \tag{22}$$

For length d (m) and energy E (MeV), the time Δt (s) it takes for the neutron to travel distance d, is

$$\Delta t = \frac{3.36 \times 10^{-9} d}{[1 - (\frac{E_0}{E_n + E_0})^2]^{\frac{1}{2}}} \tag{23}$$

In this thesis, however, the neutron energies of interest will not begin to approach relativistic speeds. Likewise, the calculation of neutron energies is not the focus of this experiment, but rather the inference of an original neutron spectrum based on the change in flux with moderation.

Functioning of an Organic Scintillator

After passing through the pulsing mechanism, the neutrons continue toward a Boron-Loaded Organic Scintillator. Knoll states, "the ideal scintillation material should possess the following properties:

1. It should convert the kinetic energy of charged particles into detectable light with high scintillation efficiency.

2. This conversion should be linear – the light yield should be proportional to deposited energy over as wide a range as possible.

3. The medium should be transparent to the wavelength of its own emission for good light collection.

4. The decay time of the induced luminescence should be short so that fast signal pulses can be generated.

5. The material should be of good optical quality and subject to manufacture in sizes large enough to be of interest as a practical detector.

6. Its index of refraction should be near that of glass (~1.5) to permit efficient coupling of the scintillation light to a photomultiplier tube or other light sensor." [9:219]

Many organic scintillators are based on organic molecules which give rise to different decaying light pulses depending on the radiation quanta incident on the detector. The fluorescence process is the prompt emission of visible radiation (i.e. light) from a substance following its excitation by charged particle interaction. The electron is excited from the ground state to a higher singlet state, which rapidly de-excites through radiationless internal conversion to the S_1 electron state. The primary scintillation light, or prompt fluorescence, is emitted as the molecule transitions from the S_1 state to one of the vibrational states of the ground electronic state and is typically on the order of a few nanoseconds for most organic scintillators.

The prolonged decay of radiation from a triplet state is known as *phosphorescence*. The lifetime for the first triplet state, T_1, however, can be as long as milliseconds. The T_1 state occurs through the process of intersystem crossing in which some excited singlet states are converted to triplet states. While in the T_1 state, some molecules may be thermally excited back to the S_1 state and subsequently decay through normal fluorescence, but at much later time. This process produces *delayed fluorescence* [9:221].

For a charged particle entering the scintillation material, a small part of the kinetic energy is converted into fluorescent energy. The remainder of the particle energy will be lost through alternative de-excitation modes no involving light output, otherwise known as *quenching* [9:222]. The converted portion of the particle energy is dependent on the particle type and the particle's energy. For organic scintillators, the response to electrons (i.e. Compton scattered electrons) is linear for particle energies above 125 keV. The response of the scintillator to heavy charged particles such as H^+, α, or Li^+ is always less for equivalent energies due to their higher linear energy transfer (LET) and is nonlinear at much higher initial energies [9:225].

The term electron volt equivalent was created to relate the non-linear energy response of heavy charged particles to that of electrons and is denoted, for example, by keVee or kilo-electron volt electron equivalent. For heavier charged particles, the increased LET produces long-lived triplet states along the

track of the ionizing particle, thus a different decay in the light output is produced between light and heavy charged particles as seen Figure 13, where the electrons are denoted by β.
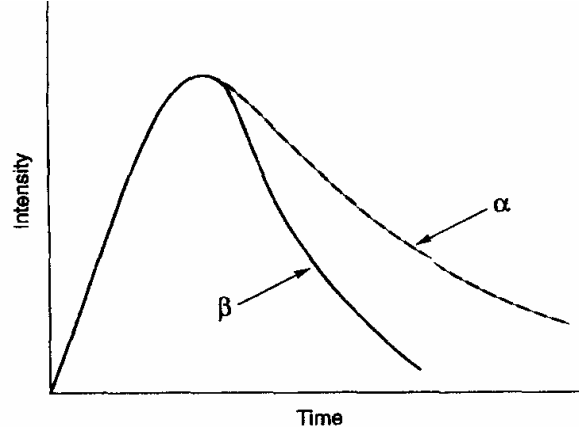
Figure 13: α and β pulse decay in a liquid scintillator [21:488]

In terms of the uncertainty in the neutron ToF, the delay of the organic scintillation molecules that are excited to the T_1 state can cause a high degree of error. Unlike the gamma-induced events that decay by fluorescence, the delayed fluorescence and phosphorescence decay of neutron events may not register until thousands of microseconds after the excitation by the incident radiation.

The liquid scintillation cocktail most often used for the detection and measurement of neutrons is an organic solution high in hydrogen content, which enhances the efficiency of trapping the neutron kinetic energy. Faster neutrons will enter the scintillation cocktail and undergo scattering events with hydrogen primarily, and to a lesser extent, carbon and oxygen nuclei. The maximum amount of energy lost by the neutron with one of these nuclei is given by

$$\Delta Q_{Max} = \frac{4mME_n}{(M+m)^2} \tag{24}$$

where   m = mass of the nucleus to which the neutron imparts its energy [MeV/c^2],

E_0 = rest mass of neutron [939.57 MeV/c^2], and

E_n = Kinetic energy of neutron [MeV] [22:213].

From this equation, one finds that a neutron can lose up to all of its energy in one interaction with the hydrogen nucleus, up to 28% of its energy with the carbon nucleus, and up to 22% with the oxygen

nucleus. It is clear from Equation 24, that as the mass of a nucleus increases, the maximum possible energy lost in a given collision decreases, thus organic scintillators, with their low Z material are ideal for slowing down neutrons in the fewest interactions and thus the shortest distance.

For fast neutrons, statistically, the ionized recoil hydrogen nuclei, or proton (H^+), are the first means of producing light output from the detector. As the neutron energy decreases, the probability of multiple H^+ events within the detector increases; however, after falling below approximately 100 keV, the neutron no longer produces H^+ events. Depending on the previously discussed mean free path, the faster neutrons may or may not be completely stopped in the active detector volume.

As the neutrons slow further, or *thermalize*, the high concentration of boron-10 (See Figure 3) allows for neutron capture and the second mechanism for light output occurs. For neutron energies below 200 keV, the capture time constant is determined solely by the ^{10}B concentration [23]. From Equation 1 we see that the interaction of a neutron with boron-10 produces an ionized lithium nucleus (Li^+) and an alpha particle (α). All three particles, H^+, α, and Li^+, can be categorized as heavy charged particles and will therefore create delayed fluorescence and phosphorescence in the scintillator.

An added feature of the organic scintillator arises from the low Z-value of its constituents, hydrogen, carbon, and oxygen. Because the scintillator is comprised totally of these type nuclei, the photoelectric cross-section for gamma rays of typical energies is extremely low and thus the detector will only give rise to a Compton continuum, rather than the usual Compton continuum and full absorption peak [9:224]. Thus, the third means of producing light in the detector is from Compton scattered electrons produced from gamma rays$^\oplus$. This type of light output, as discussed earlier, is fluorescence.

Because the different processes for fluorescence, delayed fluorescence, and phosphorescence depend on the nature of the incident particle, the detector output due to gammas, or neutrons, can be easily identified through a technique called *pulse shape analysis*, which will be discussed in more detail in chapter III [9:230]. Furthermore, it is not only possible to differentiate heavy charged particles from light, but to differentiate between various types of heavy charged particles.

The aforementioned linear response of electrons versus the non-linear response of heavy charged particles, such as H+, α, and Li^+, does not emphasize the drastic difference of the two responses. For a neutron entering the active detector volume, the ability to become thermally captured increases with lower energy as shown in Figure 3. If thermalized, the neutrons undergo the reaction $^{10}B(n,\alpha)^7Li$, which yields either 2.792 MeV (6%) or 2.310 MeV (94%), depending on whether the ^7Li (Li^+) is left in an excited state.

For a detector with even a moderately degraded response, one would still expect a thermal neutron capture peak to appear at the higher end of the energy spectrum; however, the extent of the non-linearity of the heavy charged particles becomes crystal clear when looking at Figure 14 below. The non-linearity of the organic scintillator produces a 60 keVee peak, rather than an approximately 2 MeVee peak as would be expected. The response of the detector to α and Li^+ is non-linear by a factor of 38.5.
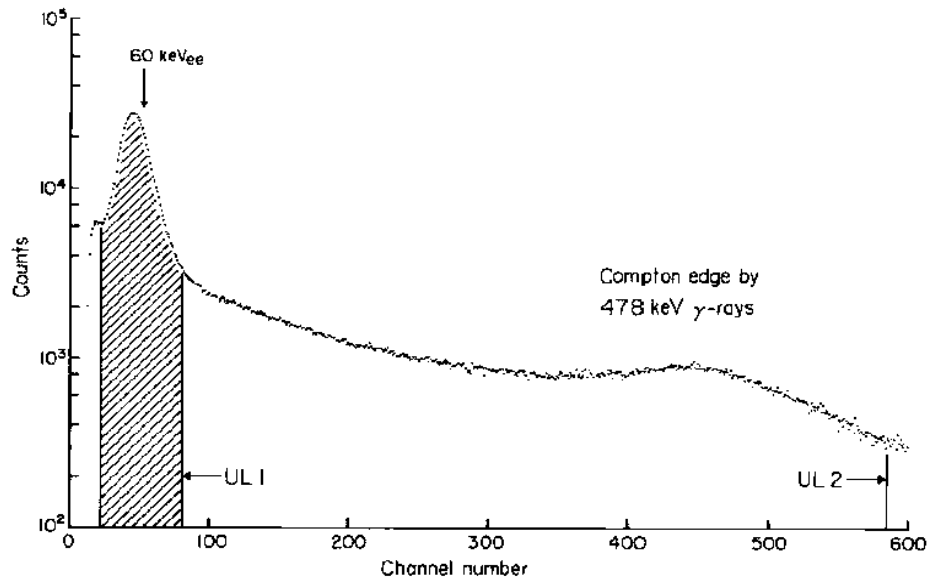
Figure 14: Pulse height spectrum (hatched area) for neutron energies derived from α-particles and ^7Li recoils produced in the thermal capture reaction $^{10}B(n,\alpha)^7Li$ [24:492]

In addition to the non-linear response of α and Li^+ particles, an expected non-linear response to the H^+ generated in the elastic collisions of neutrons with the hydrogen is expected. Because of their lower mass, charge, and energy, the extent of the non-linear response of H^+ is somewhat less than that of the α

$^\oplus$ Coincidentally, the Compton edge was used in calibrating the detector's energy response as outlined in

26

and Li$^+$. Also, because of the neutron's ability to impart any amount of energy, from all to none, on the hydrogen, a continuum of energies is expected. Figure 15 below provides an idea of what the spectrum might look like. The continuum shown is less convoluted than the H$^+$ recoil spectrum of a PuBe source due to its creation from monoenergetic neutrons.
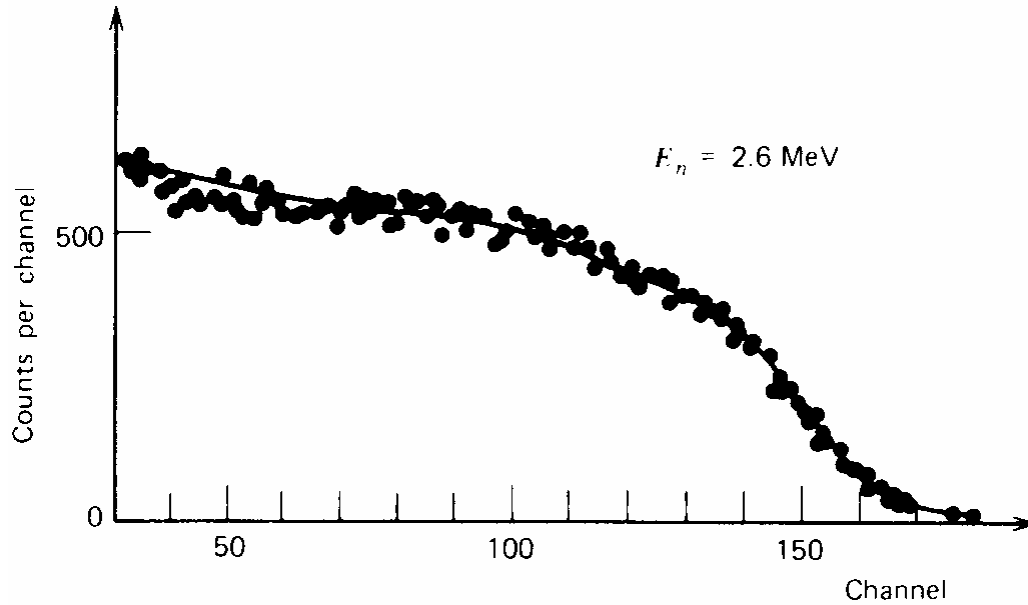
Figure 15: Proton recoil energy spectrum of monoenergetic neutron source [9:562]

Background

Up until this point, only neutron interactions with the moderation and detector have been considered; however, due to the large mean free path of neutrons in most materials, neutron interactions occur in all surrounding materials. Neutrons of sufficient energy will penetrate the disc, the disc housing, and other surrounding materials and scatter, both elastically and inelastically. Some neutrons will scatter away from the detector, but others will scatter into the detector. These scattering mechanisms result in a nearly unstoppable continuum of neutrons that are part of the background counts. The physical limitations (i.e. mechanical properties) of the aluminum disc prevent the fabrication of a disc large enough to attenuate nearly all of the higher energy scattered neutrons. The presence of this background continuum produces

Appendix F.

error, as the change in the thermal flux produced with presence of moderation *rides* on top of this background continuum. Although cumbersome, the presence of this continuum does not prevent the production of the forward edge spectrum.

Summary

Armed with the theory outlined thus far, a means of identifying a source type based on inferred characteristics of its energy spectrum gathered through the application of all the aforementioned processes is possible. The presence of moderation shifts the *true* spectrum and thus the flux of thermal neutrons. The pulsing disc mechanism provides a start time for the neutrons to traverse a fixed distance. The organic scintillator provides a means to identify the thermal capture of a neutron. The counts gathered during one opening and closing of the shutter represents one complete neutron data set. Although any particular data set will not be representative of the source type, a large number of data sets will provide the means to generate an arrival of counts at the detector over some time (i.e. the forward edge spectrum), which is a statistical representation of that particular neutron source's spectrum. By comparing several moderated forward edge spectrums to an unmoderated forward edge spectrum, inferences about the neutron's energy spectrum can be deduced.

An example of a *forward edge* spectrum is given in Figure 16. Statistically, the neutrons will arrive according to the detector area exposed and at the time it takes a particular energy neutron to traverse the flight path from disc chopper to detector. Through the *binning* of neutrons by arrival time, the change in slope from *time bin* to *time bin* can provide a telltale signature of the characteristics of the neutron spectrum as it arrives at the detector. In Figure 16, the number of counts arriving during the complete exposure of the detector to the source is at its maximum for that particular time bin. The earlier time bins have fewer counts arriving because the exposure area is less and the near thermal peak neutron energy (i.e. 3.1 MeV in Figure 6) has not traversed the required distance. The later time bins have a smaller slope because the flux of thermal neutrons is diminishing with decreased exposure area. The actual data set information and analysis will be presented in chapter IV.
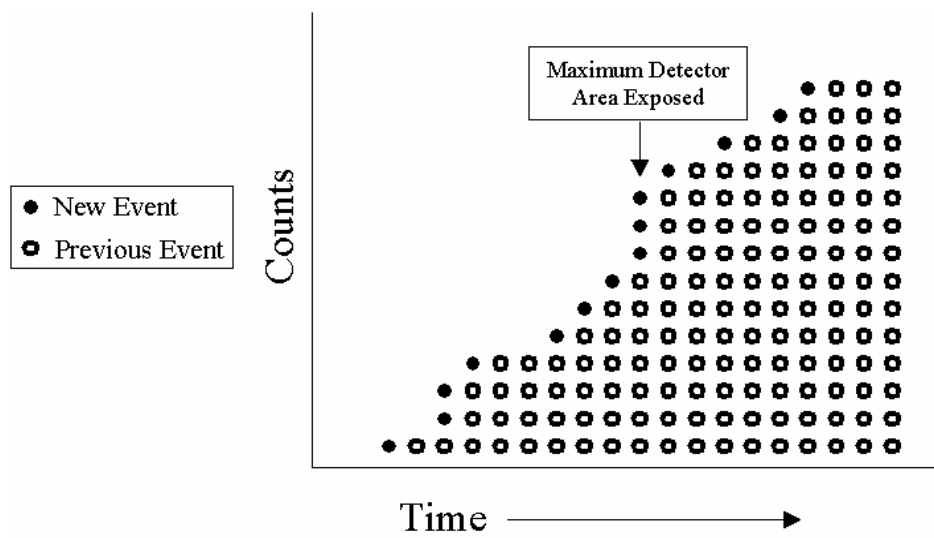
Figure 16: Example of "forward edge" spectrum

III. Methodology

Chapter Overview

Where chapter II, Theory, started with various theories of neutron spectroscopy, then moved toward the general concepts of this particular theory, chapter III, Methodology, will present the specifics of this process. The different groups of components, each group's system of nuclear instrumentation modules (NIMs) utilized, each modules specific function, and their combined function will be explained in detail. Additionally, the code used in data analysis will be examined.

Common Electronic Components

The signal detected by the organic scintillator is processed for both pulse shape analysis (PSA) and energy spectroscopy. Prior to reaching either of these two branches, the signal is modified by a group of common components depicted in Figure 17.
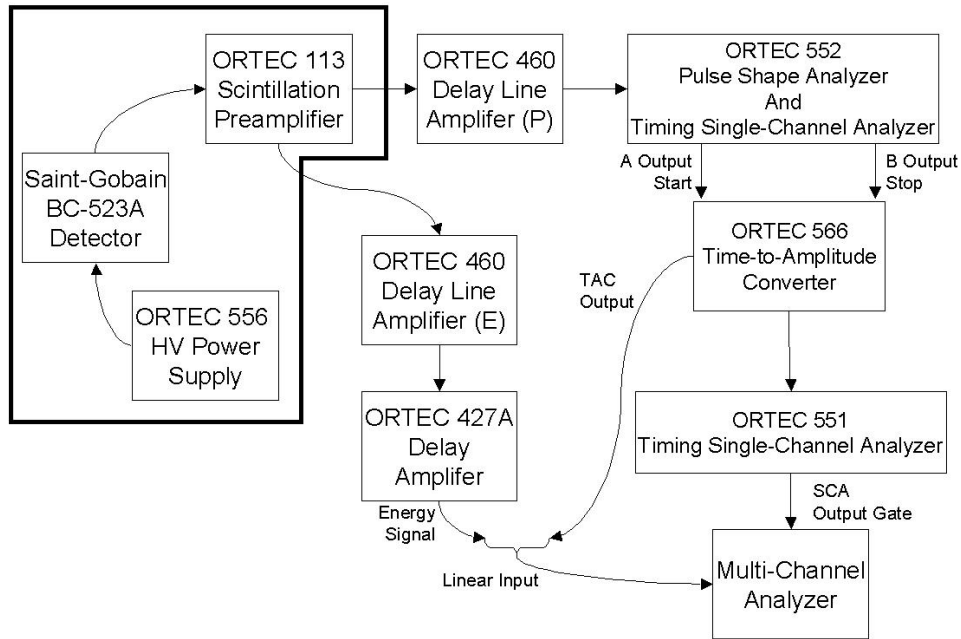
Figure 17: Common Nuclear Instrumentation Modules (NIMs) utilized in pulse processing

The ORTEC Model 556 High-Voltage (HV) Power Supply provides well-regulated and very stable high voltage required for proper functioning of the photomultiplier. It is attached to the HV connector port of the Saint-Gobain BC 523A Boron-Loaded Organic Scintillator via RG-59A/U 75Ω cable.

The output voltage of the ORTEC 556 HV Supply ranges from ±10 to ±3000 V [25:13.6]. The recommended operational voltage of the BC 523A is +750 V.
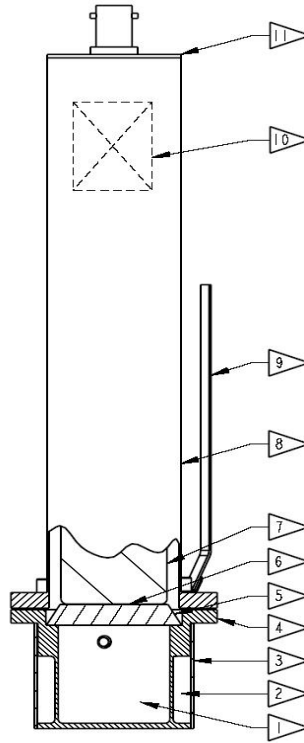
Figure 18: Engineering schematic of the BC 523A detector

The organic scintillator, housed in a protective aluminum casing (position 4, Figure 18), produces a *flash* of light upon an interaction with radiation. Since the scintillation material is transparent to the wavelength of its own emission, 425 nm, the light travels uniformly unattenuated in all directions inside the bicro-cell (position 1, Figure 18). On all sides of the bicro-cell, save one, resides a reflective paint, which increases the light output through the optical window (position 5, Figure 18). The similar index of refraction between the optical window and the scintillation cocktail ensures maximum transmission of light. A cylinder 3 cm in diameter and 3 cm in depth defines the active volume of the detector. The design measurements of the detector, as laid out in Appendix D, make it very well suited for optimizing the thermal capture of the 3.1 MeV neutron peak found in Figure 6. The optical window is coupled via transparent optical silicone grease to a Hamamatsu R6095 phototube or photomultiplier tube (PMT) similar to the one pictured in Figure 19.

The PMT is constructed of an outer glass surface with an inner photocathode. The photocathode consists of a photosensitive substance that produces photoelectrons under interaction with photons of visible light. The ORTEC 556 HV Supply creates a positive charge on the dynodes in the PMT. The photoelectrons produced at the photocathode accelerate toward the positively charged dynode. The dynode is made of a metal plate containing a substance on the surface such as a bi-alkali compound, which emits secondary electrons upon an impact from an accelerated electron [21:864]. A series of several additional dynodes, each with a higher potential than the previous one, further accelerates and multiplies the secondary electrons. The culmination of this PMT process is an avalanche of electrons at the last dynode, also called the anode. This final avalanche of secondary electrons is collected as a current pulse. Most important in this process is the understanding that the number of photoelectrons produced at the PMT photocathode and the magnitude of the final current pulse collected after the series of dynode amplifications are proportional to the light intensity, which is in turn a function, linear or non-linear, of the type of radiation energy absorbed by the scintillation detector [21:864]. Additionally, the time at which the electrical pulse is generated can be used to infer the arrival time of the light pulse and consequently, the arrival of the radiation.
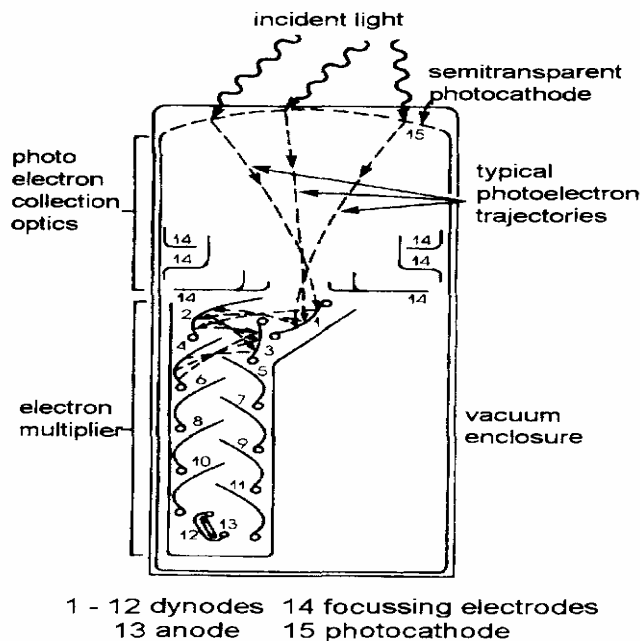
Figure 19: Schematic of a photomultiplier tube [18:357]

The current pulse generated by the PMT travels out the signal output port of the detector through a short distance of RG-62 A/U 93Ω cable to the ORTEC Model 113 Scintillation Preamplifier as shown in Figure 17[⊕]. The primary function of the preamplifier is to extract the signal from the detector without significantly degrading the intrinsic signal-to-noise ratio [25:2.1]. The ORTEC 113 is a non-inverting, parasitic-capacitance preamplifier. The current pulse generated by the detector is integrated on the combined parasitic capacitance present at the detector output and the preamplifier input and produces a voltage pulse as shown in Figure 20 [25:2.3]. The natural internal capacitance of the preamp is ~45 pF. The ORTEC 113 is an adjustable capacitance preamp. Adjusting the capacitance selector switch on the preamp adjusts its sensitivity and adjusts the height of the voltage pulse output from the preamp accordingly. The adjustable capacitance can be set at 0, 100, 200, 500, and 1000 pF. The setting utilized for this experiment was 0 pF, thus only the natural capacitance was used. The range of pulse output of the ORTEC 113 is ±3.5 V into a 100Ω load. As shown in Figure 17, the preamp voltage pulse travels toward two separate ORTEC 460 Delay Line Amplifiers (DLA). Pulse Shape Analysis requires the first DLA, while the energy spectroscopy requires the second DLA[⊕].
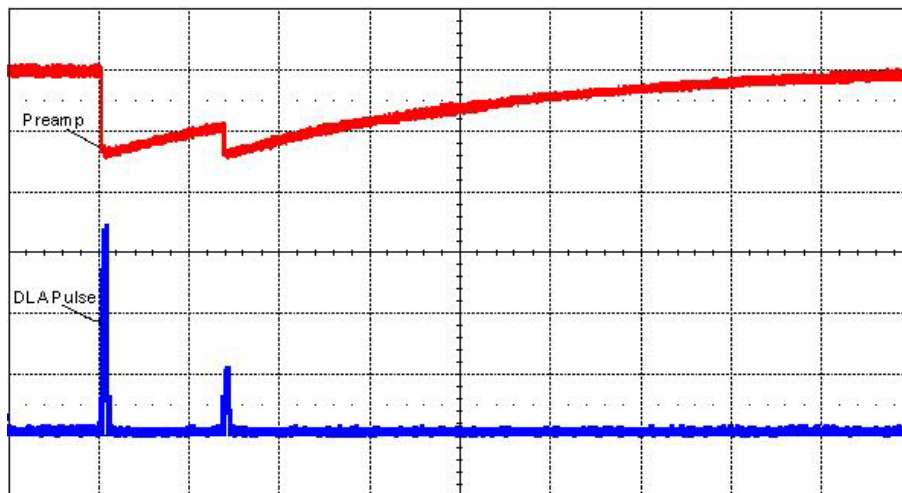
Figure 20: Preamplifier and Delay Line Amplifier oscilloscope outputs

[⊕] All cables used to connect the devices from hereon can be assumed as RG-62 A/U 93Ω cable unless otherwise stated.
[⊕] In order to avoid confusion, the Pulse Shape Analysis Delay Line Amplifier will be referred to as DLA (P) and the Energy Spectroscopy Delay Line Amplifier will be referred to as DLA (E).

Pulse Shape Analysis

In chapter II it was shown that the different decay processes associated with light and heavy charged particles is a useful process and can be taken advantage of to identify a gamma event from a neutron event. Again, in order to describe the process of pulse shape analysis, it is best to look at it through a chronological method detailing each NIM in Figure 21.
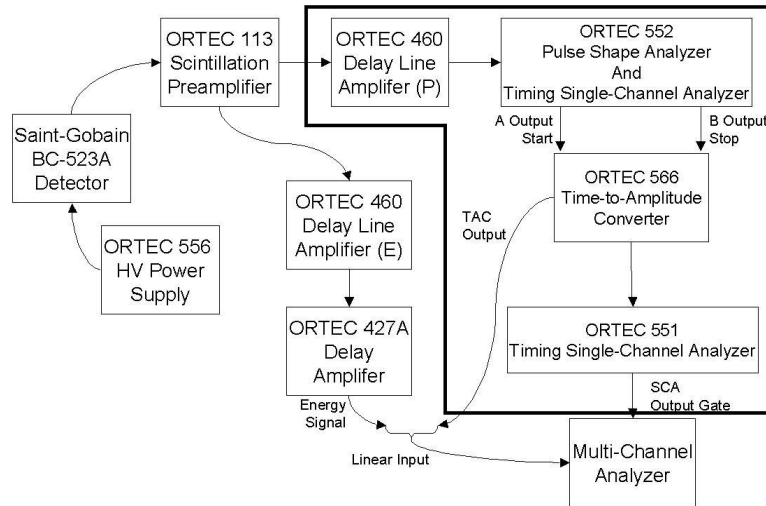
Figure 21: PSA branch NIM configuration

As indicated by its name, the ORTEC 460 Delay Line Amplifier DLA employs the technique of delay-line pulse shaping, which is well suited for scinitillation detectors [25:3.5]. Delay-line pulse shaping produces an essentially rectangular output pulse from each step-function input pulse provided by the preamp as in Figure 20 above. This particular feature makes the ORTEC 460 the amplifier of choice for leading-edge timing techniques, especially when coupled with the ORTEC 552 Pulse Shape Analyzer/Timing Single-Channel Analyzer (TSCA). For pulse pile-up prevention, this shaping method is close to ideal because an immediate return to baseline is obtained as shown in Figure 20.

Like all linear amplifiers, the ORTEC 460 linearly magnifies the amplitude of the preamp output from its low voltage range into the 0.1 to 10 V range; however, issues arose, which prohibited high amplification by the DLA (P) and eventually caused the removal of PSA all together. This problem, as outlined in Appendix E, introduced the use of the second DLA (E). The ORTEC 460 can provide both a unipolar and bipolar positive or negative output, although for this application the positive unipolar output

was chosen due in part to a need for the best signal-to-noise ratio. The ability to choose the integration time, via a toggle switch on the front panel, permits a better match to the rise time of the pulse furnished by the preamp. This particular feature was instrumental in separating the gamma events from the neutron events. The integration setting of 0.1 µs was ideal in resolving the gamma peak from the neutron peak, as illustrated a portion of the rise of the voltage pulse from the in Appendix E. Table 1 provides a list of the settings used throughout this experiment.

Table 1: DLA (P) SETTINGS

Fine Gain (Front)	x 0.5
Course Gain (Front)	x 10
Integration Setting (Front)	0.1 µs
Input Polarity (Front)	Negative
Delay (Rear)	Out (Prompt)

The ORTEC 460 accepts preamp (i.e. dependent on integration time setting), delays it by the factory preset of 1 µs and inverts it, then adds it back to the initial rise of the voltage pulse (Figure 22). Notice that the time information is inverted in the process of producing the trailing edge of the pulse. The 10% decay of the light pulse corresponds to the 10% rise of the preamp pulse. With the delay an inversion time of the DLA, this 10% rise in the preamp corresponds to a 10% decay in the trailing edge of the DLA pulse as shown in Figure 22. Once the light pulse has decayed to 90% of its original amplitude, the preamp has built up to 90% of its final amplitude, which corresponds to the 90% decay point of the trailing edge of the DLA output pulse [26:11]. Since the decay in the trailing edge of the DLA pulse corresponds to the decay time of the scintillator, the property of the original radiation causing the light output in the scintillator is retained [25:A.18].
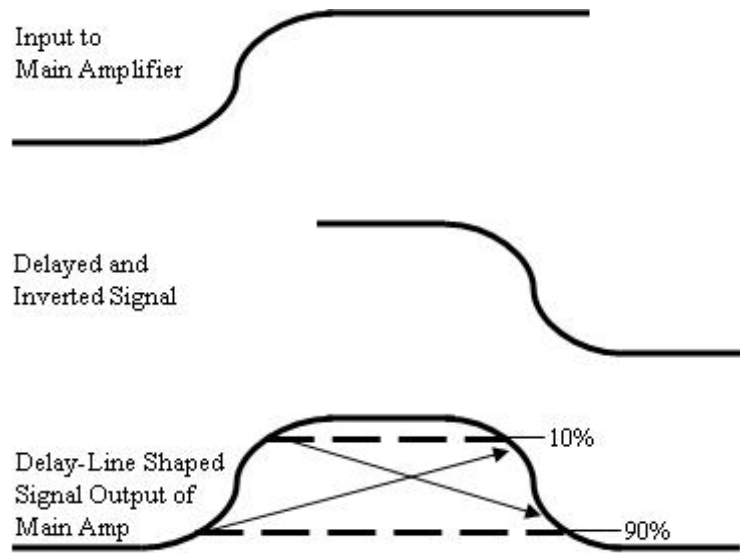
Figure 22: Single-Delay-Line shaped signal [26:11]

As shown in Figure 21, the output from the DLA (P) goes to the ORTEC 552 PSA/ TSCA. The TSCA portion of the ORTEC 552 can be used as either a single-channel analyzer or as an integral discriminator. The PSA part of the ORTEC 552 can interpret information using pulse shape analysis by comparing the time relationships between its two sets of outputs. The PSA output criteria come in the form of percentage decay of the incoming pulse. The *start* pulse is generated when the incoming pulse from the DLA (P) achieves a set percent decay from its maximum. This decay percentage can be set to one of three settings, 10%, 20%, and 50%, which is controlled by the internal A-fraction jumper. As shown in Appendix E the 50% decayed trigger point was used for the A-fraction setting in this experiment. As the pulse decays, a second pulse, or *stop* pulse, is generated once the decay percent criteria of the B-fraction is met. The terms *start* and *stop* are used because these pulses are used as start and stop triggers in the ORTEC 566 Time-to-Amplitude Converter, which will be discussed next.

A selector switch on the front panel of the PSA, which ranges from 10% to 90%, adjusts the B-fraction decay setting. A factory set delay of 0.1 μs between the two trigger points can be adjusted up 1.1 μs using the delay potentiometer on the front panel. Two potentiometers also on the front panel allow for adjustment of walk compensation for the A-fraction and B-fraction outputs. An attenuator toggle switch allows for attenuation of the input signal of x1, x10, or x100.

The TSCA provides the ability to set an upper and lower threshold on the input pulse. It can be operated in one of three modes: integral, normal, or window. The normal mode was used for this experiment and essentially allows the upper level discriminator (ULD) setting and lower level discriminator (LLD) setting to act independently in providing an upper and lower voltage threshold [27:3]. The LLD was kept at 0.0 V and the ULD was set to 9.0 V because the characteristic feature of the neutron capture pulse occurs very low on the energy spectrum. The settings of the ORTEC 552 Pulse Shape Analyzer and Timing Single-Channel Analyzer can be found below in Table 2. The data collected from the PSA can be seen in both Appendix E and chapter IV. Again, recall that the pulses generated by the PSA/TSCA are in fact determined by the rate of decay of the light in the scintillation material and are thus still directly associated with the type of radiation incident on the detector.

Table 2: PSA/TSCA SETTINGS

Pulse Shape Analyzer	
A-Fraction (Internal Jumper)	50%
B-Fraction (Front)	90%
Attenuation (Front)	x 1
Delay (Front)	0.1 μs
Timing Single-Channel Analyzer	
Upper Level (Front)	9.0 V
Lower Level (Front)	0.0 V
Mode (Front)	Normal

From Figure 21 the start and stop pulse travel to the ORTEC 566 Time-to-Amplitude Converter (TAC). The TAC generates an analog output pulse that has an amplitude from 0 and +10 V, which is proportional to the time difference between the start and stop inputs. The 50% decay point pulse (A-fraction), from the PSA provides the start pulse. The 90% decay point pulse (B-fraction) provides the stop

pulse. Using the range rotary switch in conjunction with the multiplier switch, both located on the front panel of the TAC, a time interval between 50 ns and 2,000,000 ns (2 ms) can be measured.

As an example, with the TAC range and multiplier switch set to 500ns, a TAC output created from a time interval of 250 ns would show up as a 5 V pulse. A 20-turn potentiometer can delay the TAC ouput from 0.5 μs to 10.5 μs based on the stop input. The TAC operated under the settings listed in Table 3. Time-to-Amplitude Converter output can be seen in Appendix E and chapter IV.

Table 3: TAC SETTINGS

Range (Front)	50 ns
Multiplier (Front)	x 10
Delay (Front)	0.5 μs
Strobe Mode (Front)	Internal

According to Figure 21, the TAC output now goes to both the Multi-Channel Analyzer (MCA) and the ORTEC 551 TSCA where a gate is created. The TSCA of the ORTEC 551 works in the exact same fashion as the TSCA portion of the ORTEC 552 except that it is creating a voltage threshold for the TAC output, rather than the DLA (P). Operated in the normal mode via a toggle switch on the front, the 551 generates a nominal output voltage pulse of +5 V and 500 ns wide if the input pulse amplitude exceeds the LLD setting, but does not exceed the ULD setting. Again, in the normal mode, each threshold is adjusted independently in the range of 40 mV - 10 V, and the ULD must be set higher than the LLD to permit SCA outputs [28:1]. A delay selector, in conjunction with a delay toggle switch, can delay the TSCA output from 0.1 to 11 μs.

Recalling chapter II, the different radiation interactions, gamma or neutron, have different decay times. These scintillation decays are processed through the NIMs. The TAC output represents two different amplitude events based on the type of radiation causing the event, either neutron or gamma. The TSCA sets a LLD threshold above the amplitude of the gamma events, creating a gate for the MCA. The TAC output

that flowed directly to the MCA is counted only if the TSCA gate is open. The data for gated TAC events can be seen in chapter IV. The TSCA operated with the settings listed in Table 4.

Table 4: TSCA SETTINGS

Lower Level (Front)	4.9 V (γ + n) or 5.6 V (n only)
Upper Level (Front)	10
Mode (Front)	Normal
Delay Switch (Front)	1.0
Delay Toggle (Front)	0.1 – 1.1 μs

Although shown as moving directly from the TAC to the MCA in Figure 21, in actuality, the signal was sent to a Canberra Model 9633 Analog-to Digital Converter (ADC). The ADC simply allows for processing of the signal prior to readout by the MCA. The ADC has a number of features. The Busy indicator is a 20-segment LED display, which shows the average dead time in increments of 5%. Dead time is the time that the ADC is busy converting an input and increases proportionately with increases in gain and conversion. Gain controls the ADC's resolution; that is, the number of parts into which the full-scale (10 V) inputs can be divided. The larger the selected gain, the finer the divisions and the greater the resolution. The range allocates the number of channels to be used by the ADC.

As an example, if the range is set to 4096 and the gain is set to 8192, then the MCA output represents voltage inputs of 0-5 V; however, if the gain is set to 4096, then the MCA output represents voltage inputs of 0-10 V. The offset is used to shift the memory assignment of the ADC's conversions. As an example, if the gain is set to 8192 and the range is only 4096, an offset of 4096 would permit observation of voltage inputs from 5-10 V. The LLD and ULD act in the same fashion as the LLD and ULD of the TSCA. The mode can be set to coincidence or anticoincidence for use with a gate, such as that provided by the TSCA. The settings of the ADC are listed in Table 5. The ADC settings are controlled by way of the MCA software. The ADC communicates with the MCA software in the computer via a Canberra Model 556A Acquisition Interface Module (AIM) [29:5].

39

Table 5: ADC SETTINGS

Gain	Adjusted throughout
Range	4096
Offset	Adjusted throughout
LLD	1.51%
ULD	110%
Zero	0.0001%
Coincidence Mode	Anticoincidence

Energy Spectrum Analysis

With a firm understanding of the PSA branch of the electronics in Figure 21, it is now time to consider the analysis of the energy spectrum. Recalling the non-linear response of the organic scintillator to heavy charged particles, the need for amplification of the 60 keVee thermal capture peak is required; however, the DLA (P) amplification of x5 produced the problems outlined in Appendix E. The need exists to amplify the energy signal as much as possible in order to better observe the low energy thermal neutron capture peak, but in doing so, the DLA (P) would lose all ability to create a pulse capable of later pulse shape analysis. The need for a second amplifier is quite obvious and based on the ORTEC application guide, the DLA is the premier choice for energy spectroscopy with scintillation detectors [25:3.17].

From the ORTEC 113 Preamp in Figure 17, the signal splits in two directions. The PSA branch was just reviewed; now the energy branch depicted in Figure 23 will be explained in detail.
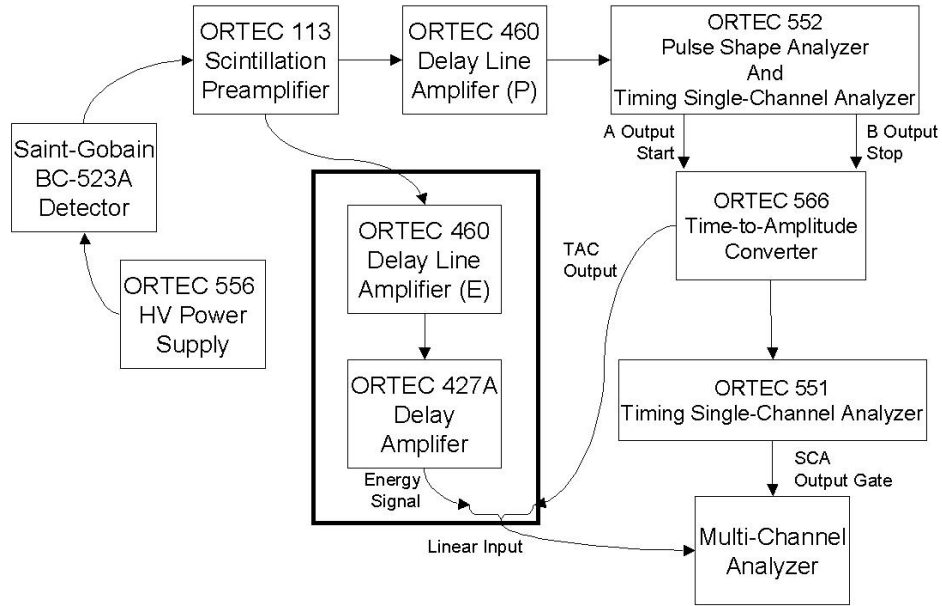
Figure 23: Energy spectrum branch NIM configuration

With the knowledge that the same DLA cannot conduct both PSA and energy spectroscopy, a second DLA, the DLA (E), was added with a much higher amplification. The DLA (E) can be operated in any of the three integration settings since the overall pulse height generated is independent of the rise time of the pulse. The amplification of x30 was chosen based on the analysis outlined in Appendix F. The settings for the DLA (E) are outlined in Table 6.

Table 6: DLA(E) SETTINGS

Fine Gain (Front)	x 0.6
Course Gain (Front)	x 50
Integration Setting (Front)	0.1 μs
Input Polarity (Front)	Negative
Delay (Rear)	Out (Prompt)

The energy signal from the DLA (E) runs through an ORTEC 427A Delay Amplifier, which serves to delay the signal in order to coincide with the TSCA gate created from the PSA branch. The 427A

41

allows for incremental linear delays ranging from 0.25μs to 4.75 μs. It has a natural delay of 60 ns. The delay is adjusted with a series of switch-selectable steps on the front panel [25:3.21]. This experiment utilized a delay of 1 μs.

The energy signal for the DLA (E) was gated using the TAC output generated from the PSA branch of NIMs. The outputs, which can be seen in Appendix F and chapter IV, represents the energy spectrum of gamma events, neutron events, or both, depending on what portion of the TAC output from Figure 36 is being observed through the LL/UL discriminator of the TSCA.

Thus far the electronics for both PSA and energy spectroscopy have relied on the ability to gate TAC and energy outputs through the coincidence/anticoincidence mode of the ADC/MCA. The ADC/MCA, while useful for analyzing the *raw* energy spectrum of the PuBe source over several seconds or minutes, is not fast enough, nor resolute enough for analysis of the disc chopper data. The ADC/MCA requires counting times several order of magnitude above the resolving time needed for analysis of the disc chopper, which will operate in the micro-second range. A new set of electronics must be devised in which the energy output signal is captured via the LeCroy WavePro 7100. This entails the development of both an energy gate that isolates the thermal neutron capture peak and a coincidence unit that provides coincidence between the thermal neutron capture peak event (energy branch) and the neutron peak from the PSA output[⊕].

Replacement of ADC/MCA

As shown in Figure 24 below, the output of the DLA (E) is sent to a delay amplifier and a TSCA. The delay amplifier delays the energy signal to coincide with the arrival of the gate produced by the TSCA at the ORTEC 542 Linear Gate and Stretcher (LG&S).

[⊕] At this point in the research, all efforts to use PSA in discriminating against gamma events were being made; however, in the end as shown in Figure 25, the PSA branch was not used.
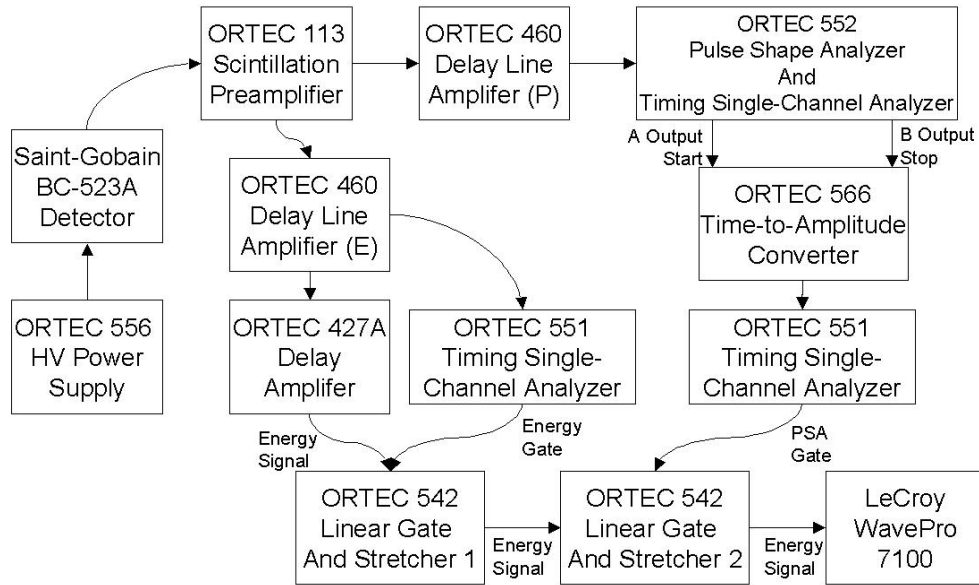
Figure 24: ADC/MCA electronics replacements

The LG&S accepts short duration linear input pulses and provides linear output pulses of the same amplitude when the input gate requirements are satisfied. The input gate may be operated in either a coincidence or an anticoincidence mode. The gate period generator is triggered on the leading edge of a gate input pulse and continues for an effective period set by a front panel adjustment. The gate period must overlap the linear input pulse peak for coincidence mode operation or must overlap the discriminator response for anticoincidence mode. The front panel allows for several adjustments. A screwdriver potentiometer adjusts the sensitivity level for input discrimination between +0.1 to +1V. The output delay screwdriver potentiometer adjust the delay period from peak detect to start of output pulse from 0.5 to 5 μs. The output width screwdriver potentiometer adjusts the width of the output pulse from 0.5 to 5 μs. A locking-toggle switch controls the gating function and can be left in normal (ungated) or gated. The gate period is a screwdriver potentiometer that adjusts the duration of gating control from leading edge of the gate input pulse. The range is adjustable from 0.5 to 5 μs. Another locking-toggle switch selects either coincidence or anticoincidence mode for gate input function. Because two separate LG&S modules were initially used, the LG&S following the DLA (E) will be referred to as LG&S 1, while the second LG&S will be referred to as LG&S 2. The settings for the LG&S 1 are listed in Table 7.

43

Table 7: LG&S 1 SETTINGS

Input (Front)	DC couple
Disc Level (Front)	+0.1 V
Output Delay (Front)	3 μs
Mode (Front)	Gated
Gate Mode (Front)	Coincidence
Output Width (Front)	0.5 μs
Gate Period (Front)	1 μs
Srobe Operation (Back)	Internal

The TSCA in the energy branch was set with a LL discriminator setting of 0.50 and an UL discriminator setting of 1.28, which provided a gate in the LG&S 1 for the thermal neutron capture peak. The output of the LG&S 1 went to the linear input of the LG&S 2. Its settings are listed in Table 8.

Table 8: LG&S 2 SETTINGS

Input (Front)	CD couple
Disc Level (Front)	+0.1 V
Output Delay (Front)	1 μs
Mode (Front)	Gated
Gate Mode (Front)	Coincidence
Output Width (Front)	0.5 μs
Gate Period (Front)	1 μs
Srobe Operation (Back)	Internal

The LG&S 2 was designed to employ the TSCA output from the PSA branch as a gate for all neutron events; however, as shown in Appendix E, the PSA branch was incapable of producing a TAC output for the low energy thermal capture event. In the end, the PSA branch was dropped from the equipment setup as shown in Figure 25.

With the absence of the PSA branch, the LG&S 1 output represents not only the thermal neutron capture event, but also Compton scattered electron events and H^+ events with energies corresponding to the TSCA's LLD and ULD. The MCA was used one last time to produce an output of the thermal neutron capture peak as shown in chapter IV. Afterward, the LG&S 1 output was sent to the LeCroy WavePro 7100.
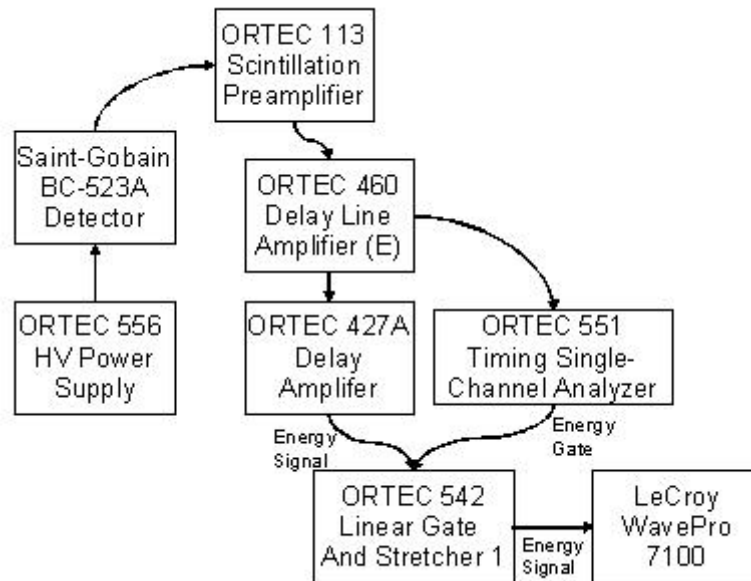
Figure 25: Final electronics setup

Disc Chopper Spin Up

The spin up of the approximately 3.5 kg aluminum disc presented special considerations. The motor required to spin at ~10,000 RPM had to be both fast and high powered. The DeWalt DW625 120 V Electronic Plunge Cut Router is a variable speed router with ranges of 8,000-20,000 RPM. The router is capable of producing 3/4 horsepower. The router used two spring loaded twin columns for depth

adjustments between 0-70 mm. The 0.5" collet coupled the router to the disc chopper via the lower shaft depicted in Figure 62, Appendix C. The router provided variable speeds as shown in Table 9. The router also came equipped with a slow start option permitting the router to spin up over the period of a few seconds, as opposed to an immediate start. This option, however, was not slow enough to counter the extreme torque produced by spinning such a large mass.

A Statco 3PN1010 Variable Autotransformer (VaryAC) provided the solution to the fast spin up. The DeWalt DW625 was connected to the VaryAC. The VaryAC provided a continuous increase in the AC power supply. With the router set at the 2nd stage, the VaryAC was slowly increased from 0% to 75% power, which provided the angular velocity of 10,000 RPM.

Table 9: VARIABLE ROUTER SPEEDS [30:3]

Stage	RPM
1	8,000
2	12,000
3	16,000
4	18,000
5	20,000

The Required Moderation

The PuBe spectrum of Figure 6 is a varied spectrum with several peaks; however, the main flux of neutrons occurs at the energy of 3.1 MeV. Moderating the PuBe source such that the 3.1 MeV neutrons are near thermal energies requires a specific thickness of paraffin. As shown in the MCNP output of Figure 26 the thickness of paraffin needed to maximize the number of thermal neutrons in the spectrum is roughly 1.8 cm; however, in order to prevent complete absorption of the 3.1 MeV energy peak, a less thick 1.5 cm thickness was used. This decreased thickness takes into account the marginal attenuation by the air in route to the detector and the attenuation by the face of the detector. With the paraffin in place, the PuBe spectrum is effectively shifted, in whole, toward lower energies, thus the initial low energy neutrons will not only be

moderated by the paraffin, but will also be mostly attenuated. Those neutrons with energies above the initial 3.1 MeV peak will now shift to lower energies ranging from near thermal up to the low MeV range.

Detector Flux vs Paraffin Thickness
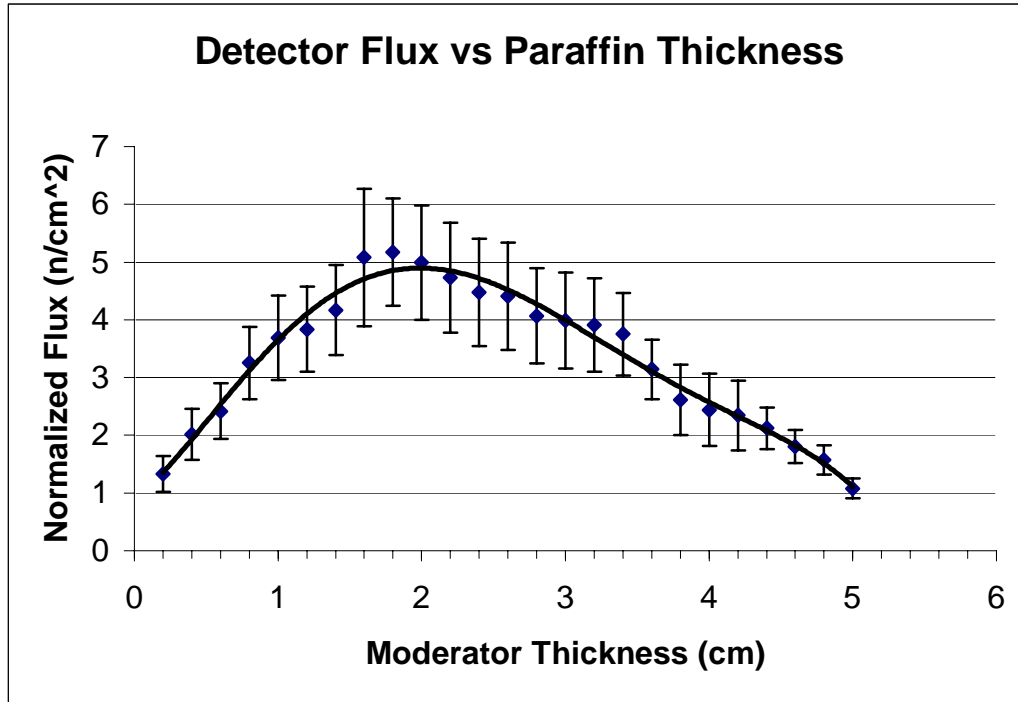
Figure 26: Flux of neutrons at detector face vs paraffin thickness from MCNP modeling

These higher energy neutrons still pose a problem with *background* counts during the operation of the neutron disc. Neutrons with enough energy (~1.6 MeV) will not be completely attenuated by the aluminum disc when it is in the closed configuration, but rather will be attenuated by some unknown amount. Higher energy neutrons will undergo scattering with some scattering into low enough energies to be captured in the detector. This capture will be delayed 10-20 μs after the last scatter/H$^+$ event and may therefore show up in the neutron events of interest (i.e. from neutron gate opening to last neutron arrival). Those neutrons that are attenuated to near thermal energies will be captured in the detector, thereby causing a continuous count throughout the entire rotation of the disc chopper. Some neutrons that are attenuated to near thermal energies as they leave the disc in the nearly open configuration will arrive at the detector at the same time as those fast neutrons that traveled through the very initial opening of the disc, thus a degree of error will be introduced.
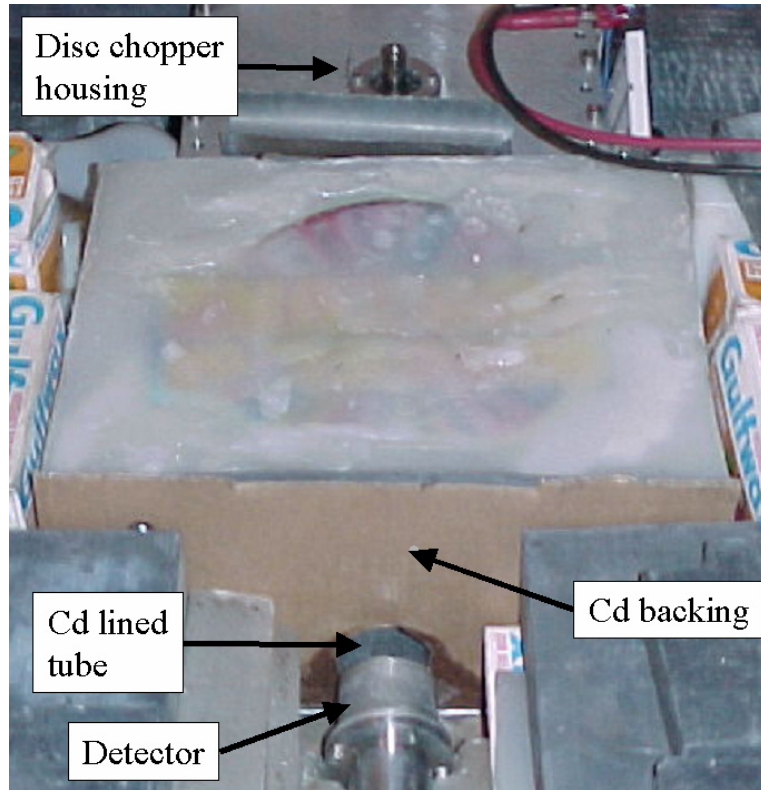
Figure 27: Paraffin block with cadmium shielding for "skyshine" reduction

The epithermal and thermal energy neutrons present another and unexpected phenomena known as *skyshine* [31]. Skyshine occurs when lower energy neutrons are scattered off surrounding materials, such as air, concrete, and other structures, and are redirected. These redirected neutrons sometimes scatter several times with their torturous path leading them back into the detector, as though they had traveled the same straight path the high energy neutrons traversed to the detector. The higher energy neutrons with their larger mean free path observe fewer interactions in flight and therefore will in general travel a straighter path than lower energy neutrons.

Within this experiment, it was possible for neutrons to travel completely around the disc chopper and get counted in the detector. In fact, without any moderation around the detector and source, the same number of counts was received whether the wheel was in the open or closed configuration. As shown in Figure 27 above, a special paraffin block was designed with cadmium lining both the flight tube and the entire face of the paraffin block next to the detector. Cadmium was also placed around the entire detector

48

with the exception of the face of the detector. Four counts were conducted in both the open and closed

configuration, respectively, with varying thicknesses of moderation placed in front of the PuBe source.

Table 10: REDUCTION IN THERMAL COUNTS BETWEEN OPEN AND CLOSED DISC
CONFIGURATION WITH VARYING MODERATION THICKNESSES

Moderation (cm)	Counts (open)	Counts (Closed)	Reduction (%)
7.5	13590	9619	29.2
6.0	14977	9595	35.9
4.5	16084	10728	33.3
3.0	17516	11503	34.3
1.5	21881	12546	42.7
0	23112	12453	46.1

As shown in Table 10, the reduction in thermal counts between open and closed increases with

decreasing moderation. This can be partially explained in terms of the increased flux of total neutrons as

moderation decreases (i.e. more of the spectrum is present); however, the dynamic interactions of the

neutrons within the disc, the disc housing, and the surrounding paraffin result in the largest reduction in

thermal counts from open to closed configuration with no moderation.

The modeling with MCNP predicted a maximum thermalization of the PuBe spectrum at 1.8 cm,

thus the 1.5 cm moderation was used throughout this experiment. With 1.5 cm of moderation present, the

thermal counts from the open configuration to the closed configuration of the disc chopper was reduced by

42.7% as shown in Table 10 above and depicted in Figure 28 below. Blocks of paraffin were also placed

around the source, the support pedestal and the detector as shown in Figure 29[⊕].

$\oplus$ Blocks of paraffin, which normally cover the disc housing and detector, are not pictured for ease in
identifying features.
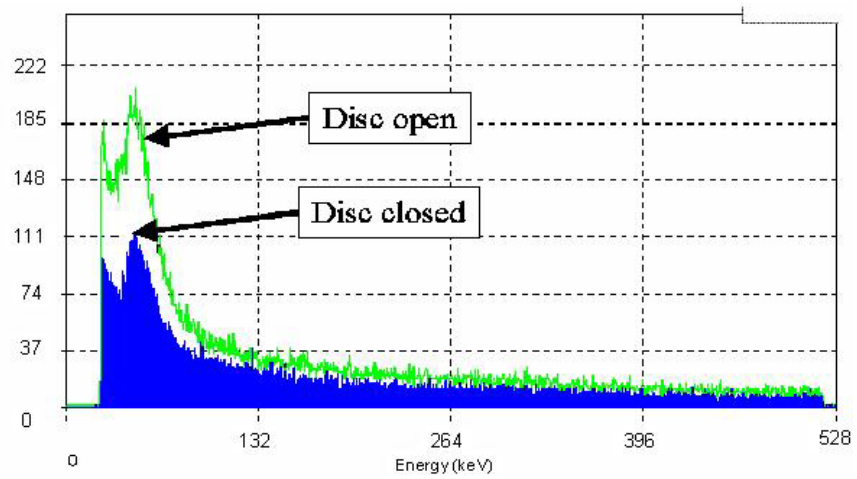
Figure 28: Comparison of thermal neutron capture counts for open and closed configuration of disc chopper
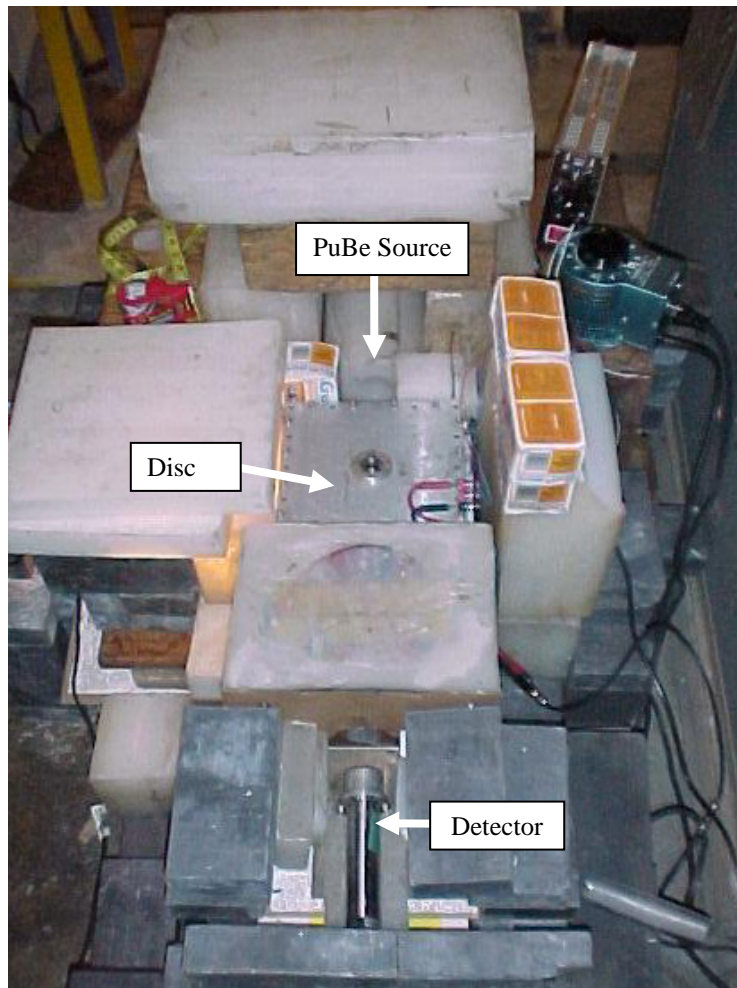
Figure 29: Placement of moderation

50

The Photodiode Trigger

An ability to correlate when the disc is in the open configuration and its corresponding neutron pulse arrival at the detector requires calibration in terms of timing. Without a known start and stop time, the pulses recorded by the LeCroy contain no information about neutron energy. The arrival time of the neutrons at the detector can only be determined with knowledge of when the neutron gate is open and closed. The timing information was gathered with the use of the setup depicted in Figure 30 below. A regular 70-watt incandescent light bulb provided the light source, which triggered the photodiode when the neutron gate was 90° off axis from the source-detector line of sight.
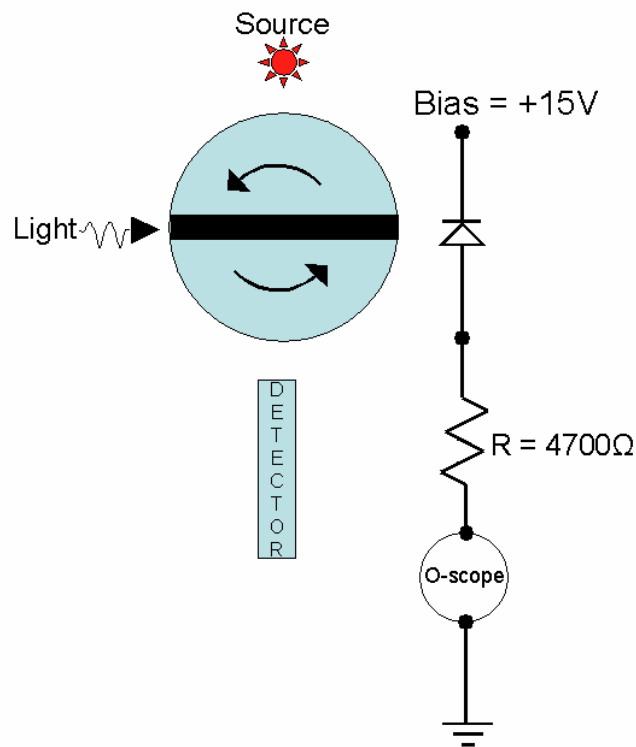
Figure 30: Photodiode layout and circuitry

An example of the oscilloscope output provided by the electronics found in Figure 25 and Figure 30 can be seen in Figure 31 below. The two peaks in the top display of Figure 31 are the triggering of the photodiode. The time between the photodiode peaks represents the time it took the disc to rotate 180°. Since the angular velocity is nearly constant once the router motor has spun the disc up to speed, the same trigger time can be used for all thermal neutron capture pulse data sets. A representative data set is seen in

the lower display of Figure 31. The three voltage pulses represent three separate neutron events. The digital oscilloscope greatly facilitated the ability to capture the timing and neutron event information.
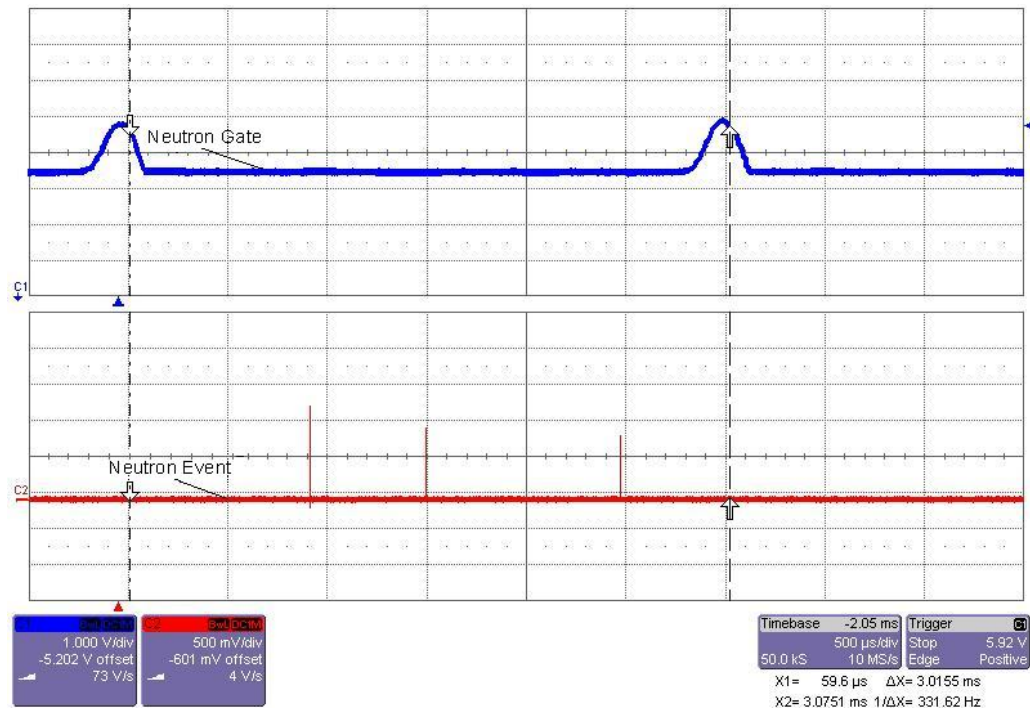
Figure 31: Photodiode output and thermal neutron capture output from Linear Gate & Stretcher 2

Data Collection

The LeCroy 7100 WavePro has a single-shot acquisition mode, which provides a series of digitized voltage values sampled on the input signal at a uniform rate [32:7-1]. Under the Save/Recall function several options exist. The input channel can be designated, the file type specified, and the save option of single, fill, or continuous can be set. A MATLAB file specification provided the most ease in later analysis. The single save option was used to capture the photodiode trigger input. The fill option was then used to capture all neutron events registering over the trigger of 200 mV. The fill option continued to save data until the 500 MB pin drive was full.

The Timebase/SMART Memory function allowed for the adjustment of the number of sample data points taken. With the oscilloscope display set at 500 μs/div, the option of 50,000 sample points was

52

selected for the first set of data collected. This option provided 100 ns/point for the full 5 ms displayed on the oscilloscope display. This option was selected because the 500 ns width of the neutron energy pulses generated by the LG&S 1 yielded approximately five data points to define each neutron pulse. Additionally, the option of 100 ns/point provided data sets that were approximately 1 MB in size, thus 438 data samples could be obtained at a time given the capacity of the 500 MB pin drive.

After analysis of the first set of data, it was clear that only one or two data points were needed to identify a thermal neutron event, so the number of sample points was reduced to 25,000, which resulted in 200 ns/point and approximately 2-3 data points identifying a neutron event. The file size was also cut in half, so that nearly 900 neutron data samples could be stored on the 500 MB pin drive.

The integration of the timing information from the photodiode and the neutron events from the electronics was handled with a couple of simple codes as shown in Appendix G, which were devised in Matrix Laboratory Software [33]. The oscilloscope saved the data in a MATLAB .DAT file form, so the MATLAB software was able to readily read the data sets.

The critical file was the photodiode-produced-timing file generated from the data as shown in the top display of Figure 31. The photodiode provided the start time on which to evaluate the timing information for all neutron data sets in that particular run. Photodiode timing files were taken for each run since the router speed varied from start up to start up. The timing information from the photodiode allowed the pinpointing of the neutron gate opening and closing, as well as the arrival of the last neutron at the detector, all of which are henceforth referred to as neutron events of *interest.*

Based on the overall setup of the PuBe source, the disc chopper, and the detector, as shown in Figure 64, Appendix C, the angle of rotation required to calculate the opening and closing of the neutron gate (absence of cadmium foil) can be calculated. In addition to the opening and closing of the gate, the disc chopper, through its natural counter-clockwise rotation, passes through other key angles of note[⊕].

Figure 32, Table 11 shows the position of the disc chopper when the slowest neutron begins its flight toward the detector. This neutron, in order to avoid attenuation by the cadmium on the opposite side

---

[⊕] The angles depicted in the figures are referenced from the full photodiode-light source line of sight.

of the tunnel, must be a low energy thermal neutron. Figure 33$^{\oplus\oplus}$, Table 11 depicts the position of the disc chopper when the fastest neutron begins its flight to the detector. The fastest neutrons will arrive at the detector on the order of a few picoseconds; moreover, relative to thermal neutrons this event will occur at the instant the source has line of sight to the detector. Figure 34,Table 11 shows the angular position of the disc chopper when the last slowest neutron must leave in order to escape the disc prior to the neutron gate closing. Figure 35, Table 11 demonstrates the angular position of the disc chopper at the last possible moment the neutrons can escape$^{\oplus\oplus}$ prior to the gate closing. This slowest neutron must now travel the distance between the disc and the detector prior to being counted. The time of flight of this neutron from the last angular position (Figure 35) added to the time of arrival of the very first neutron yields the time window for neutron events of interest.

$^{\oplus\oplus}$ Figure 33 and Figure 35 of Table 11 assume that the fast neutrons are completely attenuated by the aluminum disc and cadmium, although in reality faster neutrons are either unaffected by the disc or moderated to some degree.

Table 11: KEY ANGULAR POSITIONS OF NEUTRON DISC CHOPPER
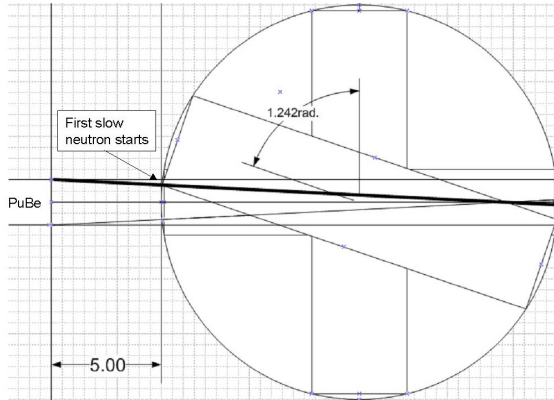
Figure 32: Start of first slow neutron
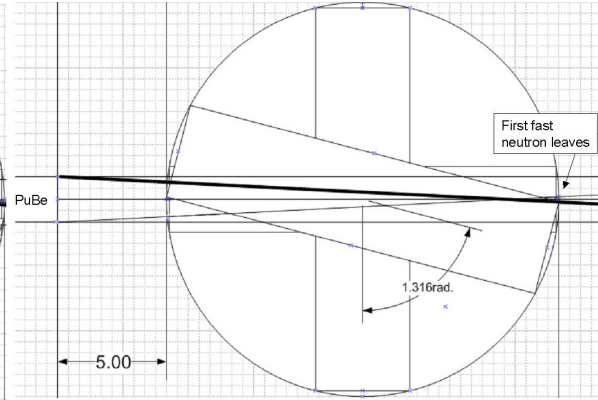
Figure 33: Start of first fast neutron
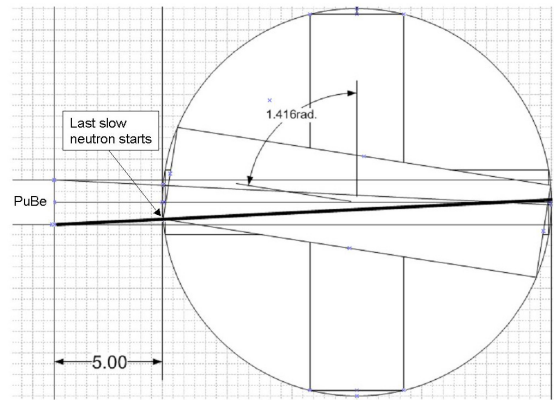
Figure 34: Start of last slow neutron
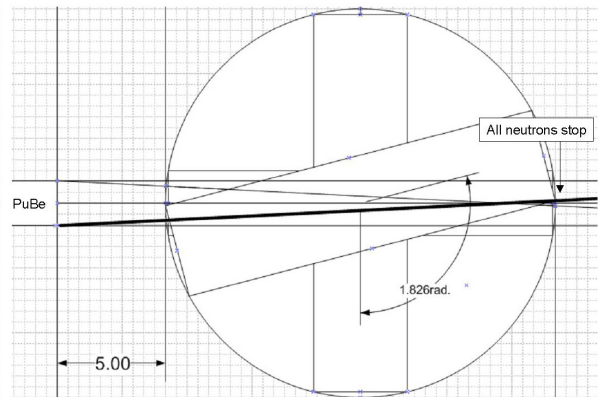
Figure 35: All neutrons stop

Summary

The methodology outlined in this section provides the specific approach towards the theory described in chapter II. A number of steps in the approach, such as the various MCNP models, the energy calibration from three separate gamma sources, the replacement of the MCA/ADC with a Linear Gate and Stretcher, and the final decision to forego PSA were secondary issues that all required a high degree of attention in order to achieve the final output files. The electronics approach used in the forward edge neutron spectroscopy was designed to take advantage of the exceptionally fast timing and operation of the 7100 WavePro Oscilloscope, without which this project would have been nearly impossible. The various data gathered from this methodology will now be discussed in chapter IV.

IV. Analysis and Results

Chapter Overview

This chapter provides an initial presentation of the results of the data collected early on in the experiment, which includes both a PuBe PSA and PuBe energy spectrum, followed by the data collected via the LeCroy oscilloscope from use of the disc chopper and later analyzed by the MATLAB code. Analysis for the PSA and energy spectrum of the PuBe source was more subjective in nature and will be discussed in conjunction with the presentation of the data. The analysis for the data collected via the LeCroy oscilloscope will follow the collected data in a separate section, as it was more objective in nature. Although detailed, this chapter is not all-inclusive, but relies on the various appendices for presentation of more intricate points in the data collection process.

Results of Pulse Shape Analysis

Figure 36 depicts a full PuBe TAC spectrum. With the use of an ORTEC 419 Precision Pulse Generator, the variation in decay times (TAC output) between the gamma$^{\oplus}$ and neutron-induced events is apparent. A clear baseline resolution between the two events was not attained in the efforts of this experiment; therefore, a degree of overlap of gamma events and neutron events occurs. This overlap is better illustrated in Figure 37 where the gamma induced ^{22}Na events clearly encroach under the neutron peak of the outlined PuBe TAC spectrum. The ^{22}Na source was the better choice among the ^{137}Cs, ^{54}Mg, and ^{22}Na sources for emphasizing/ensuring the validity of the PuBe gamma peak, as it decays with a 1.274 MeV gamma, which is most similar in energy to the 4.43 MeV and 7.66 MeV gammas emitted by the PuBe source [14:175]. The gamma energy has a direct correlation to the location of the gamma peak in the TAC output. Lower energy gammas create lower energy Compton scattered electrons, which in turn will have a higher LET, thereby creating a longer decaying pulse and consequently producing a gamma peak of longer delay. For example, the ^{137}Cs source with its 662 keV gamma will produce a gamma peak in the range of 300 ns versus the ^{22}Na peak at approximately 280 ns.

$^{\oplus}$ The term gamma event refers to the Compton scattered electrons caused by the incident gammas.
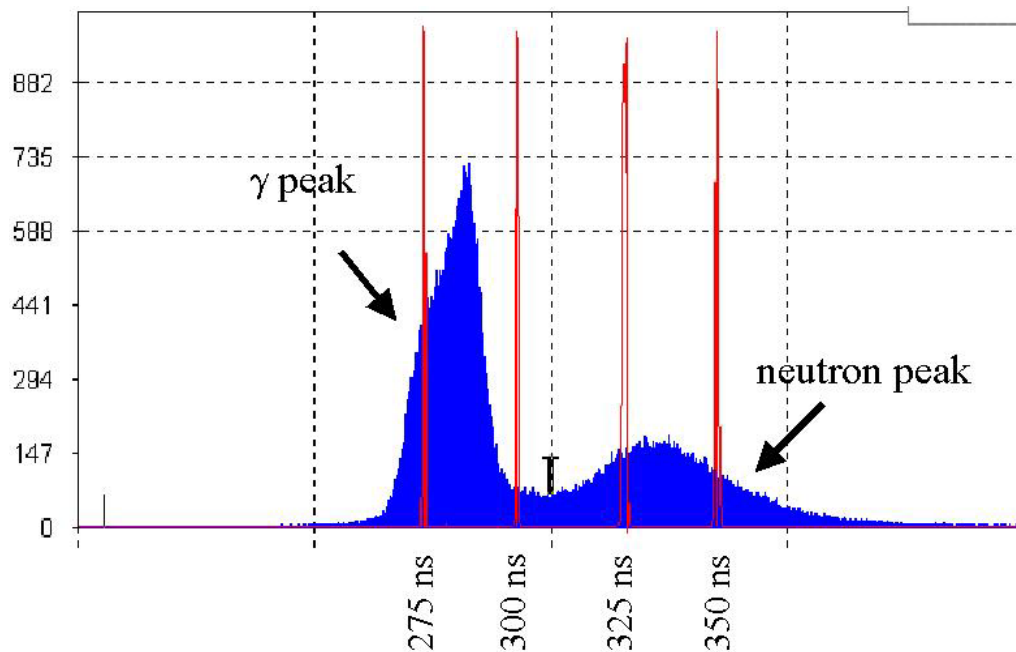
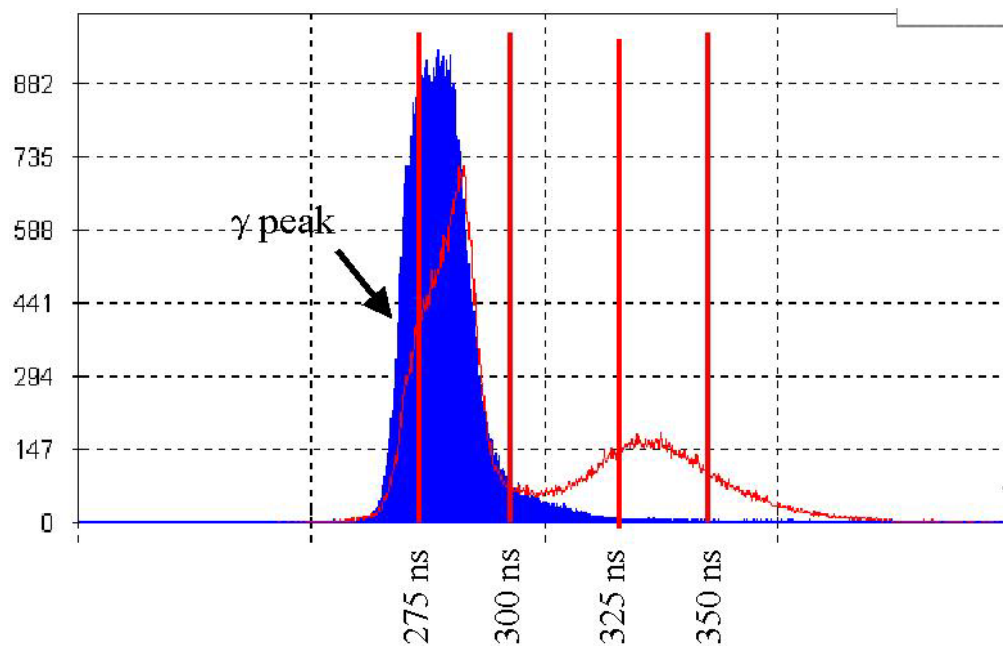Figure 36: Full PuBe TAC spectrum

Figure 37: Na-22 TAC spectrum with full PuBe reference

The application of a TSCA with a LLD=5.6 and ULD=10 (neutron events) was run in coincidence mode with the TAC output to produce Figure 38. The neutron events defined in Figure 38 contain only

some higher energy H^+ and some of the encroaching Compton scattered electrons from the gamma events. As mentioned in Appendix E, the amplification of the DLA (P) was insufficient to generate a TAC output for the low energy neutron events. I believe that had the DLA (P) been able to both amplify the preamp signal and conduct PSA on the signal, a much longer tail would have appeared on the neutron peak representing the most lengthy decay times of the thermal neutron capture event (α and Li^+).

A means exists to distinguish between heavy charged particles. As with varying gamma energies, different LETs associated with H^+, α, and Li^+ will produce different decaying pulses. The pulse produced by a H^+ with its lower mass and energy will decay more quickly than the pulse produced by the heaviest of the heavy charged particles. The Li^+ with its higher LET and production of Triplet states in the scintillation cocktail will decay over a much longer period. This experiment did not focus on the different pulse decay times associate with the three heavy charged particles; however, the LLD of 5.6 V, while cutting off part of the neutron peak in Figure 38, would only affect the more quickly decaying H^+ events and longer decaying gamma events, which are of no interest in a thermal neutron capture event.
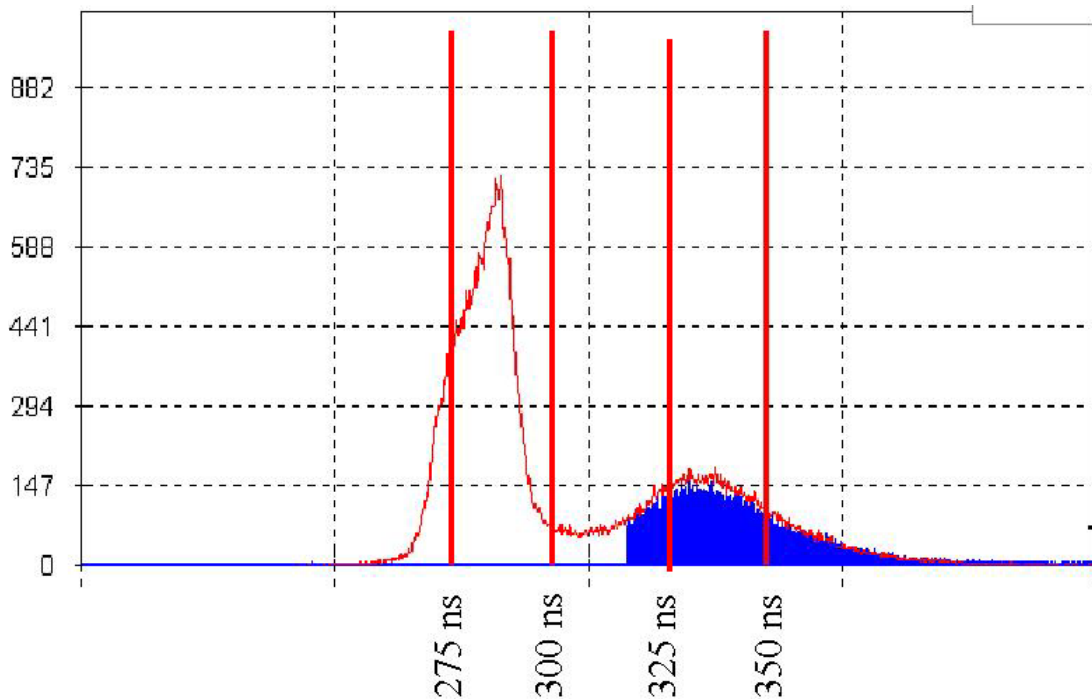
Figure 38: Gated PuBe TAC spectrum (neutrons only) compared with full PuBe TAC spectrum reference

58

The Results of Energy Spectroscopy

The PSA analysis branch was unable to establish a means of discriminating neutron and gamma events. The energy spectroscopy branch in conjunction with the LG&S 1 was the only means to focus on the energy of the thermal neutron capture peak. The energy output in Figure 39, calibrated according to Appendix F, depicts the thermal neutron capture peak, which had a centroid of 57.2 keV +/- 2.1 keV at FWHM, the H^+ continuum mentioned in Figure 15, and the continuum of gamma (Compton) events. The location of the thermal capture peak centroid was very close to the 60 keV reported by Aoyama, *et. al*. The difference can be attributed to the error associated with calibration.
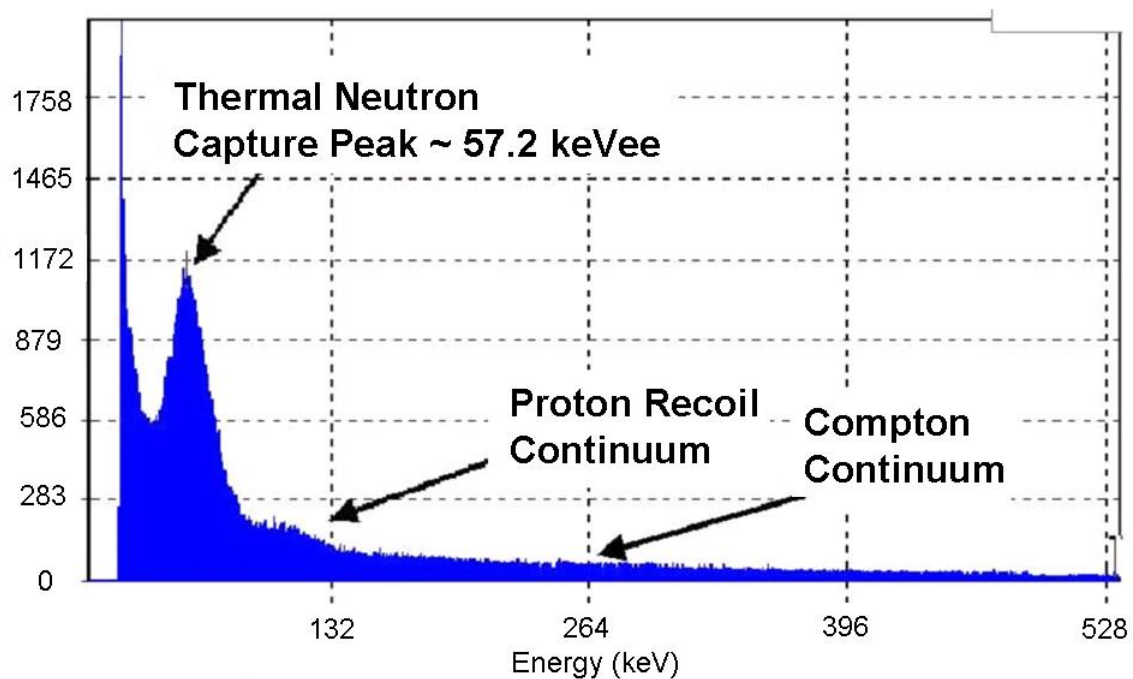
Figure 39: Full PuBe neutron energy spectrum

As shown in Figure 40, the aid of the TSCA in the energy branch permitted the isolation of the thermal neutron capture events, as well as those H^+ and Compton electron events, which had energies corresponding to a thermal neutron capture event (i.e. between 0.5 and 1.28 V). The selection of this LLD and ULD setting of the TSCA was chosen merely by means of the MCA energy spectrum, attempting to account for as much of the thermal peak as possible. After selecting the LLD and ULD range with the

MCA, the output was diverted to the 7100 WavePro Oscilloscope for use in data set collection. More information regarding the energy calibration of the detector can be found in Appendix F.
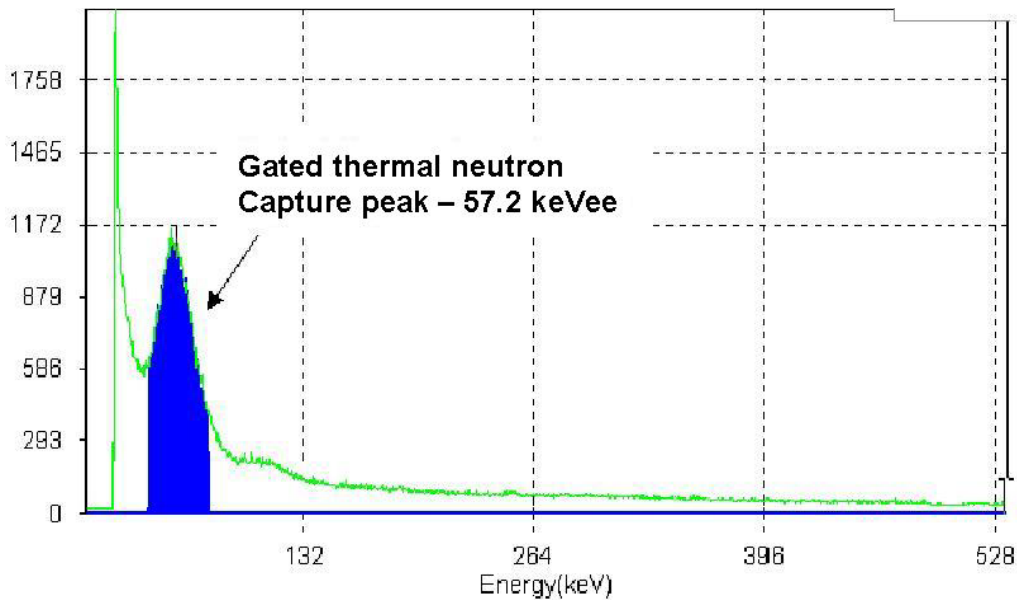
Figure 40: Gated PuBe thermal neutron capture peak

The Results of the WavePro/MATLAB Data

Five different runs were conducted in the data collection stage. The first three runs conducted turned out to contain too little data of statistical significance, thus two additional runs were performed containing much more data. Of the first three runs conducted, the data run #1 used no moderation and no cadmium cover in order to see the *true* PuBe spectrum. The data run #2 used no moderation and a cadmium cover over the face of the detector in order to see the true PuBe spectrum in the absence of thermal neutrons. Data run #3 used the 1.5 cm of moderation (paraffin) and no cadmium in order to conduct forward edge spectroscopy on the highest flux (3.1 MeV peak from Figure 6) of thermal neutrons.

The following is a discussion of the first three data runs, which although statistically insignificant, contained information worth discussing. The photodiode (.DAT) files for each of the three respective runs are depicted in the upper plot of Figure 41-Figure 43 below. The neutron event .DAT files are too numerous to list; however, representative neutron event .DAT files are seen in the lower plots of Figure 41-Figure 43.

60
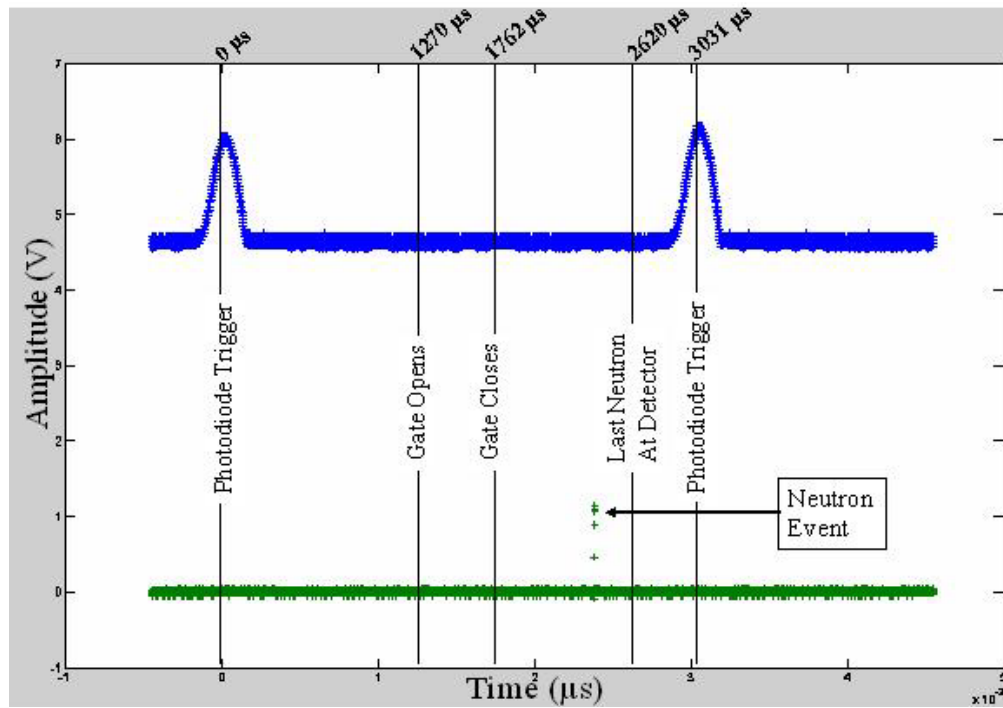
Figure 41: Combined photodiode and neutron events for data run #1 (no moderation and no cadmium cover)
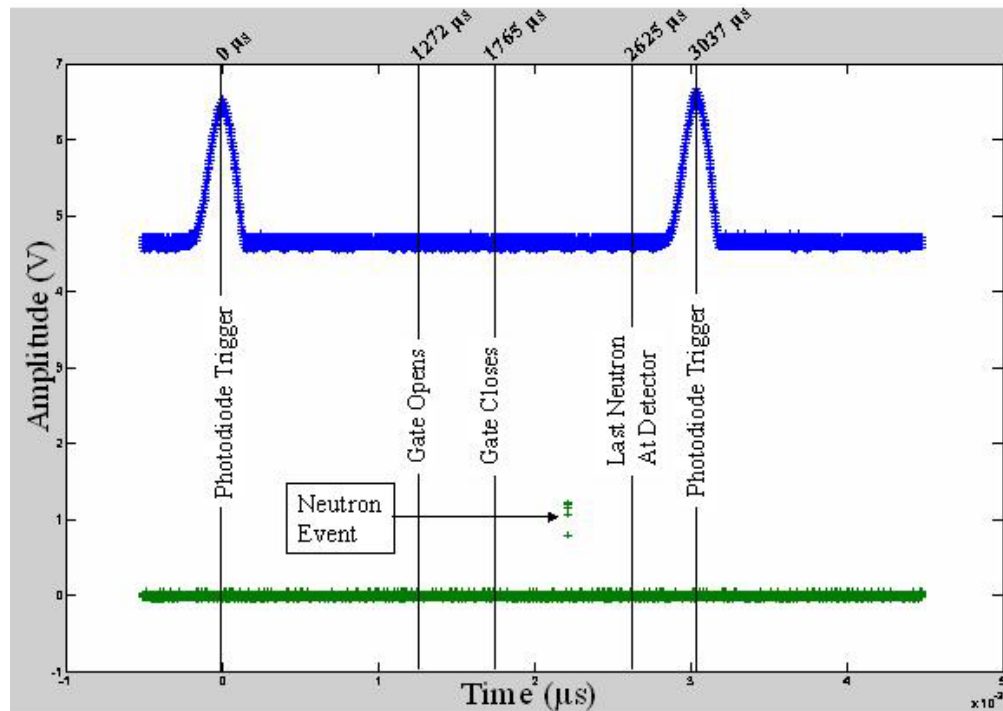
Figure 42: Combined photodiode and neutron events for data run #2 (no moderation and a cadmium cover)

61
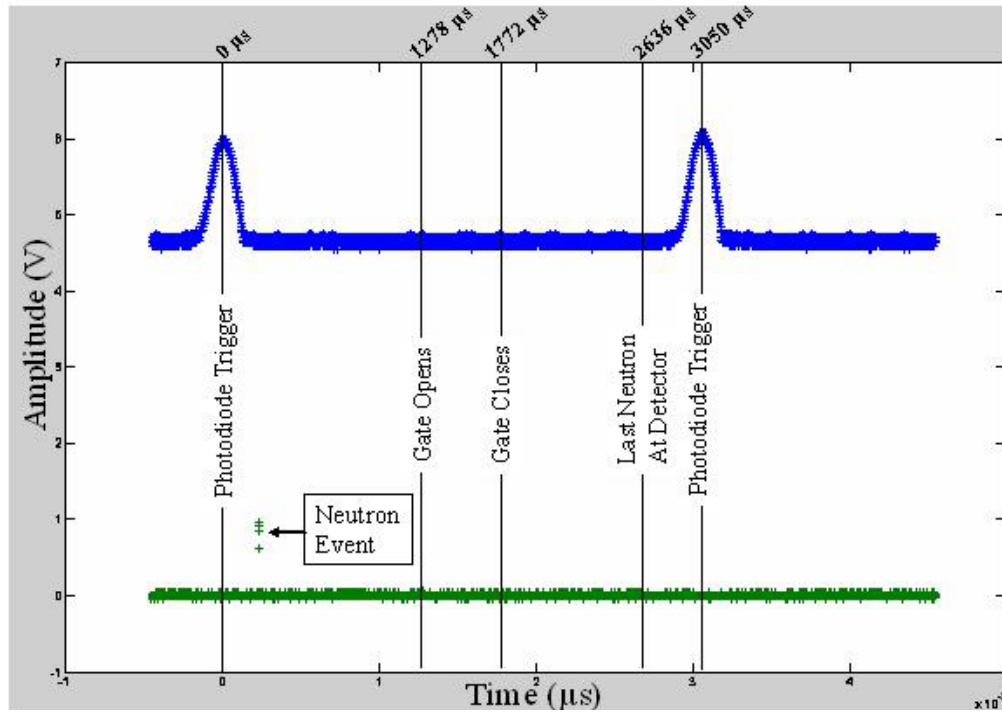
Figure 43: Combined photodiode and neutron events for data run #3 (moderation and no cadmium cover)

Figure 41-Figure 43 are temporal representations of some of the angular positions listed in Table 11. The first photodiode peak marks the reference start time (0 μs). The first three data runs, *No moderation & no cadmium* (data run #1)*, No moderation & cadmium* (data run #2)*,* and *Moderation & no cadmium* (data run #3), had varying angular velocities of 9897.10, 9878.03, and 9836.31 RPM, respectively. Due to their varied angular velocities, key events, such as the opening and closing of the neutron gate and arrival of the last neutron at the detector occurred at different times for each of the runs as shown in Figure 41-Figure 43.

The slowest neutron of interest was the one that began in Figure 32 and exited the disc just prior to closing in Figure 35 and given the angular velocities of the three runs had a kinetic energy of approximately 0.00053 eV, or roughly three orders of magnitude below the mean value of thermal neutron

energy$^\oplus$. The timing knowledge of the gate opening, gate closing and arrival of the last neutron at the detector were applied to the 1,300 neutron .DAT files compiled during the first three data runs. A MATLAB code similar to the one found in Appendix G identified neutron events in each data set and summed all neutron events into 10 µs bins ranging from 10 to 3040 µs. The data runs #1, #2, and #3 required manual input of all 1500 data sets due to the lack of a robust MATLAB code at the time of analysis.

The neutron data sets are representative of all neutron events occurring over a 180° rotation of the disc chopper. A histogram of all neutron counts arriving for data run #1 are visible in Figure 44 below. The solid bars represent the neutron events of interest (i.e. from opening of the window until arrival of last slow neutron at detector). In order to better understand the *forward edge* neutron spectrum predicted in Figure 16, a summation histogram of counts from opening until last arrival is presented in Figure 57.
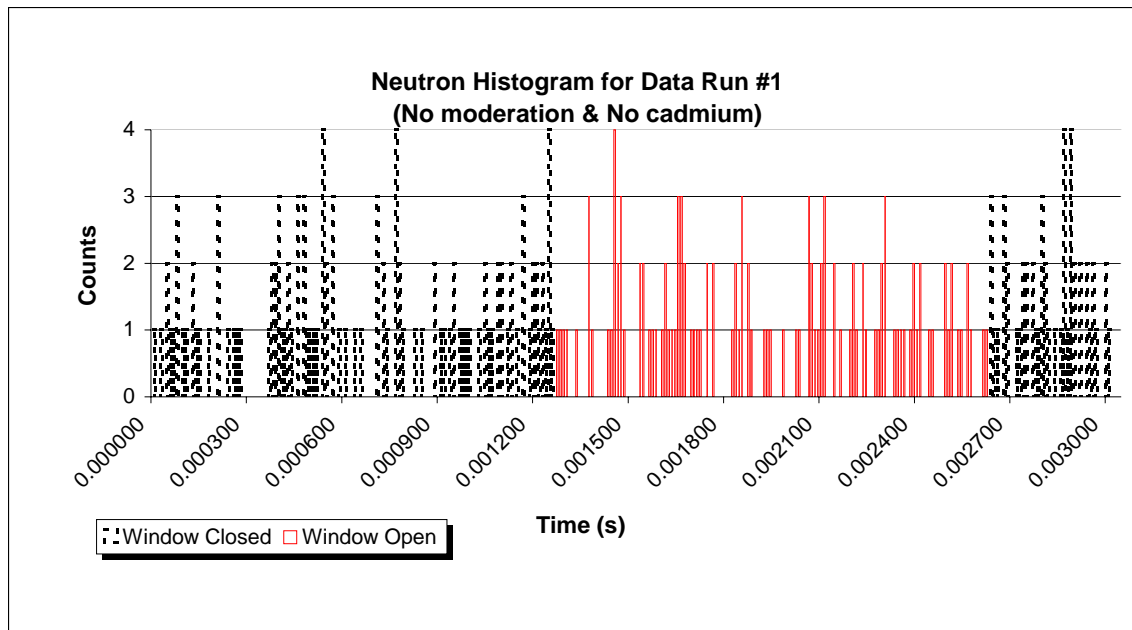
Figure 44: All neutron events for data run #1 (Note: The solid bars denote the neutron events of interest)

$^\oplus$ Appendix I shows this low energy neutron has little chance of attenuation by air prior to entering the detector and will thus be included in the flux of neutrons which determine the slope of the *forward edge*.
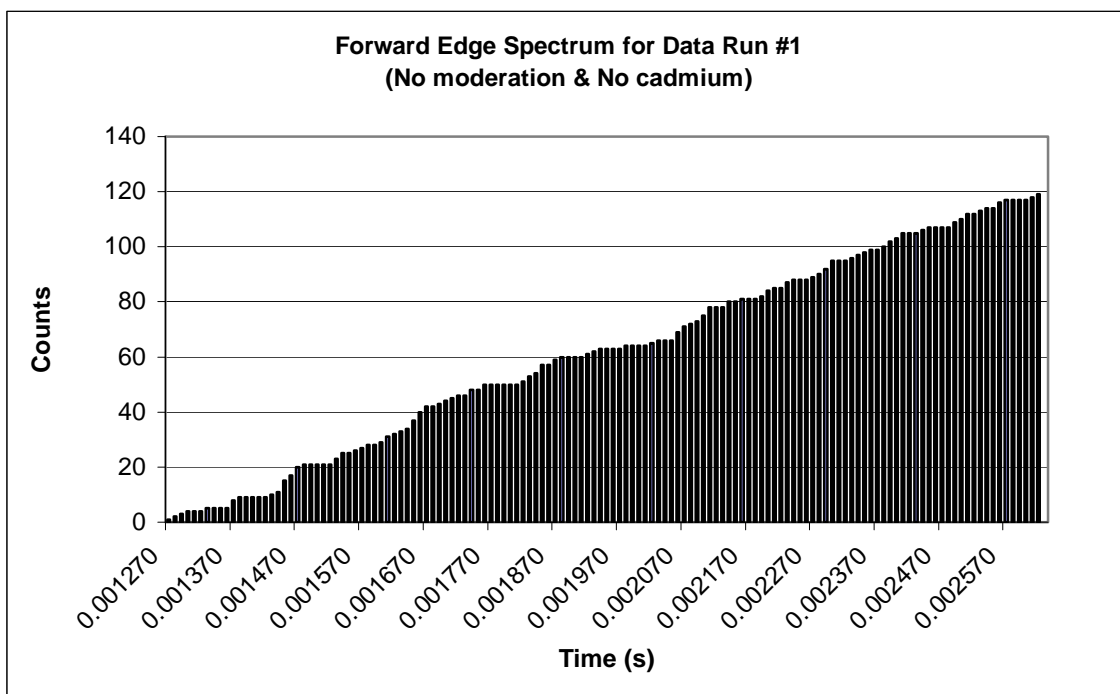
Figure 45: "Forward edge spectrum" of neutron events for data run #1
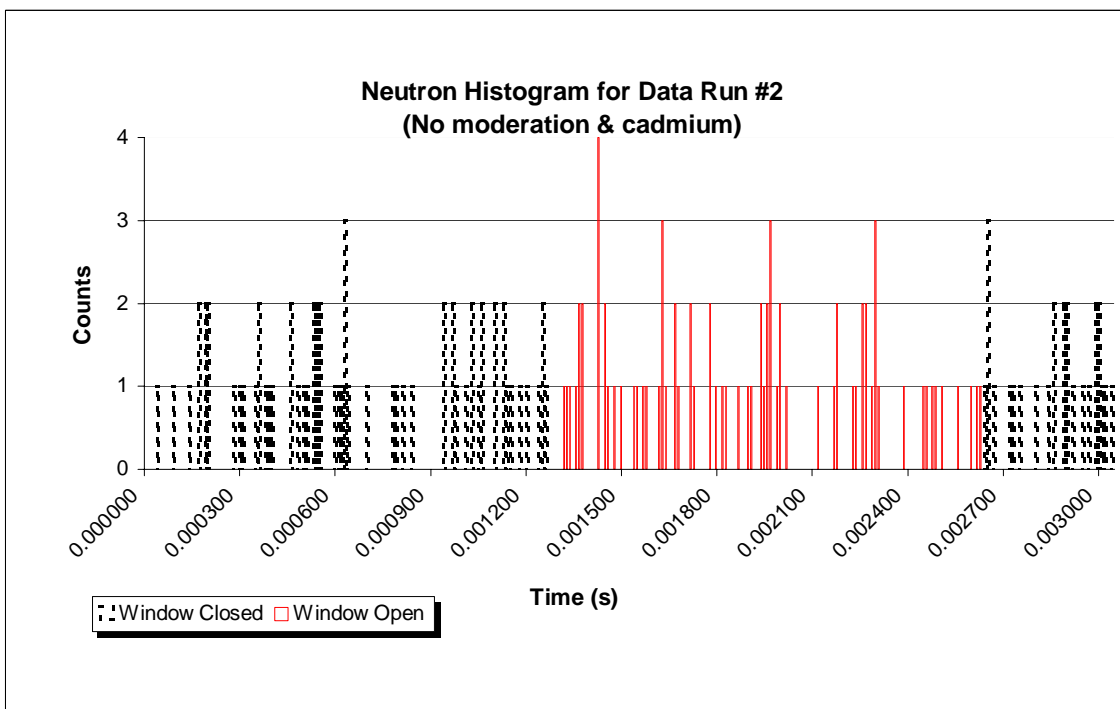
Figure 46: All neutron events for data run #2 (Note: The solid bars denote the neutron events of interest)

Forward Edge Spectrum for Data Run #2
(No moderation and cadmium)
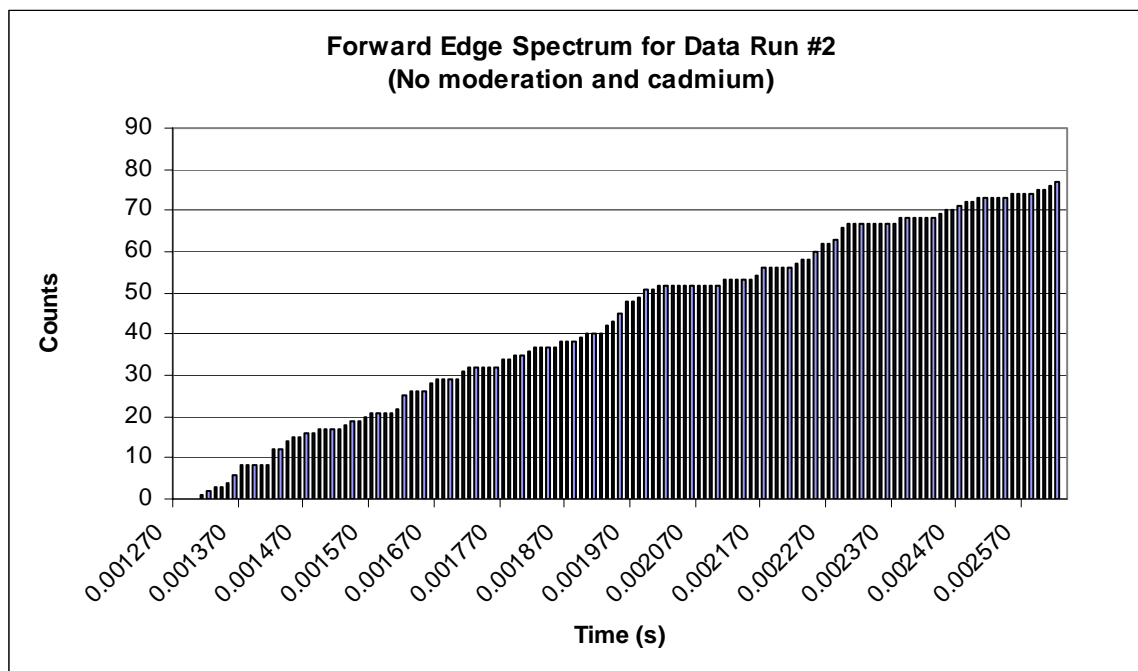
Figure 47: "Forward edge spectrum" of neutron events for data run #2

Neutron Histogram for Data Run #3
(Moderation & no cadmium)

Window Closed   Window Open

Figure 48: All neutron events for data run #3 (Note: The solid bars denote the neutron events of interest)
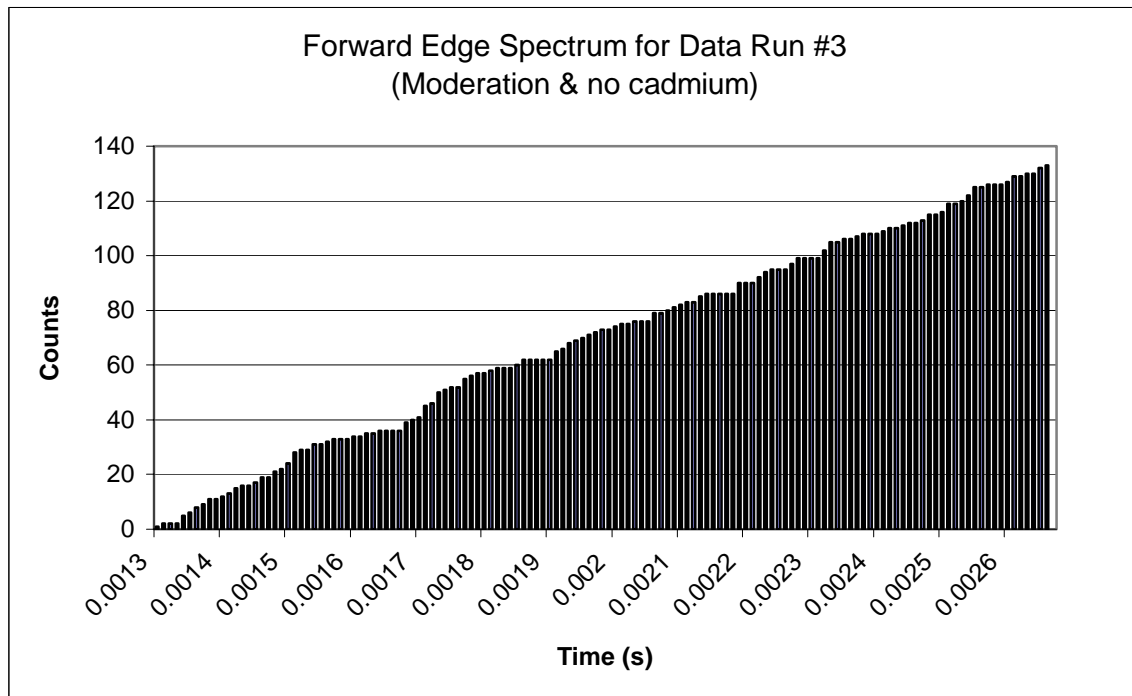
Figure 49: "Forward Edge Spectrum" of neutron events for data run #3

The histograms for the data runs #2 and #3 are visible in Figure 46 and Figure 48 above. Once again, the solid bars represent the data points of interest. The forward edge spectrum*s* for data runs #2 and #3 are displayed in Figure 47 and Figure 49.

After the realization that not enough data existed in the first three data runs, the MATLAB code was adjusted so as to automatically load each of the several thousand data sets, analyze each one, and redistribute the neutron data into the 10 µs bins from $10 - 3000 \, \mu s^{\oplus}$. The actual MATLAB code used in this data analysis and redistribution is found in Appendix G. The second two runs used no cadmium and only varied by the addition of 1.5 cm of a paraffin moderator in one of the runs. Each data run was comprised of 3,550 data sets each, for a total of 7,100 sets of datum. The second two runs, data run #4 (*Unmoderated)* and data run #5 (*Moderated*), had increased angular velocities of 9999.87 and 9999.38 RPM, respectively.

This angular velocity permitted the slowest neutron of 0.00054 eV to pass through the disc. The photodiode .DAT files for data runs #4 and #5 are depicted in the upper plot of Figure 50-Figure 51 below. Again, a neutron event .DAT file is embodied in the lower plots of Figure 50-Figure 51.

Similar style histograms and forward edge spectrums for the last two data runs are seen in Figure 52-Figure 55 following the .DAT figures below. Figure 56 provides an additional plot of both forward edge spectra from data runs #4 and #5, which brings out the distinct differences in the flux of thermal neutrons.
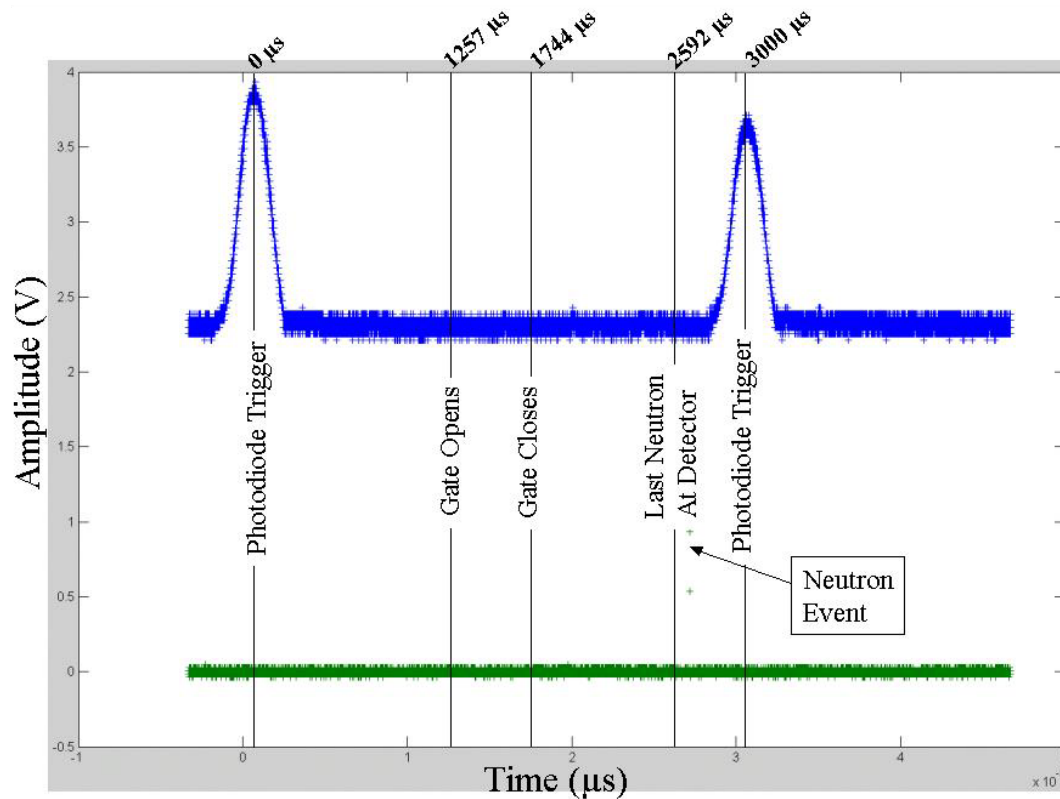
Figure 50: Combined photodiode and neutron .DAT file for data run #4 (no moderation)

⊕ The last time bin ended at 3000 μs for runs #4 & #5 because the angular velocity for these runs was approximately 100 RPMs faster than the first three data runs.
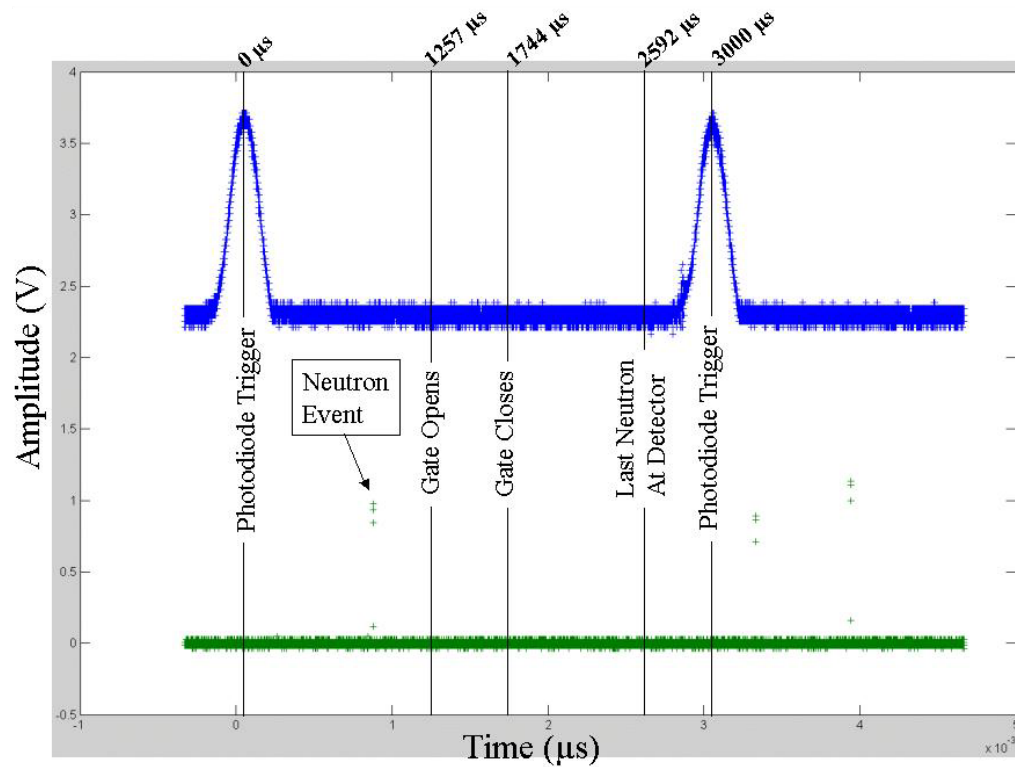
Figure 51: Combined photodiode and neutron .DAT file for data run #5 (moderation)
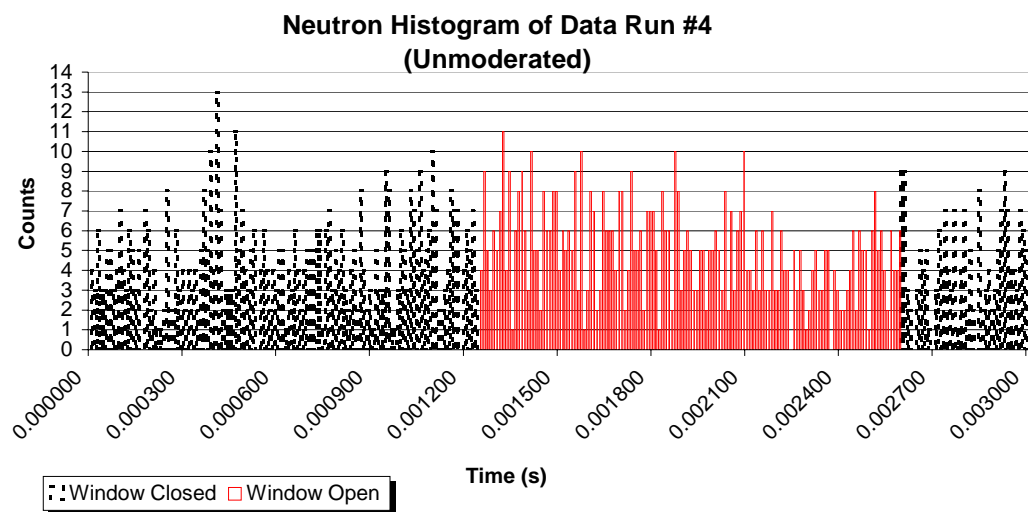
Figure 52: All neutron events for data run #4 (Note: The solid bars denote the neutron events of interest)

68

Forward Edge Spectrum for Data Run #4
(Unmoderated)
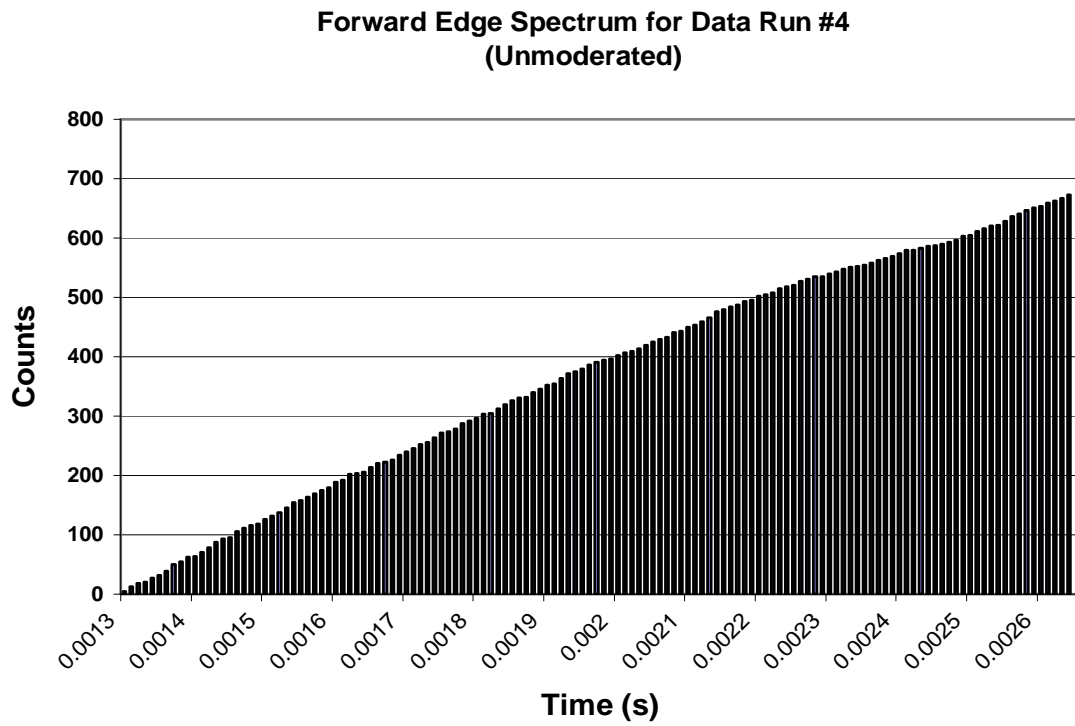
Figure 53: "Forward Edge Spectrum" of neutron events for data run #4

Neutron Histogram of Data Run #5
(Moderation)

Window Closed Window Open

Time (s)
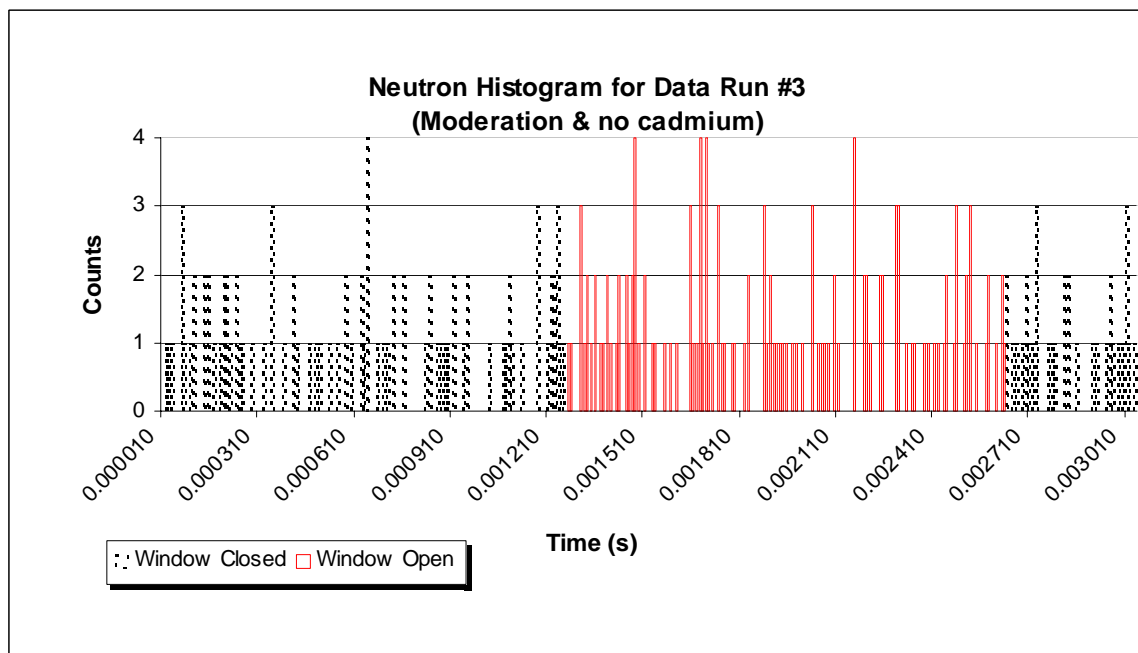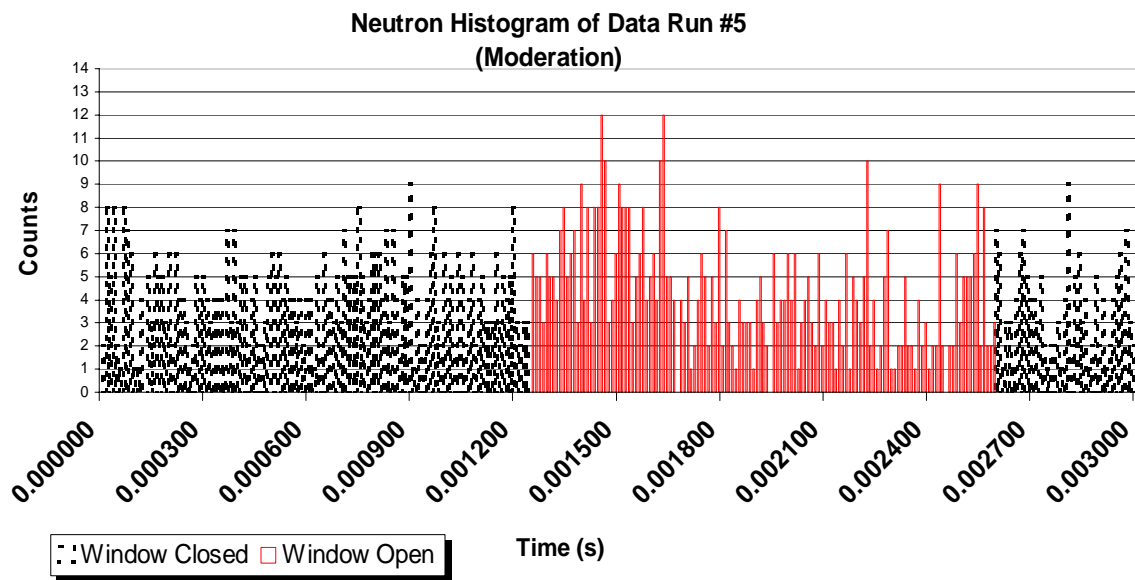
Figure 54: All neutron events for data run #5 (Note: The solid bars denote the neutron events of interest)

69

Forward Edge Spectrum for Data Run #5
(Moderated)
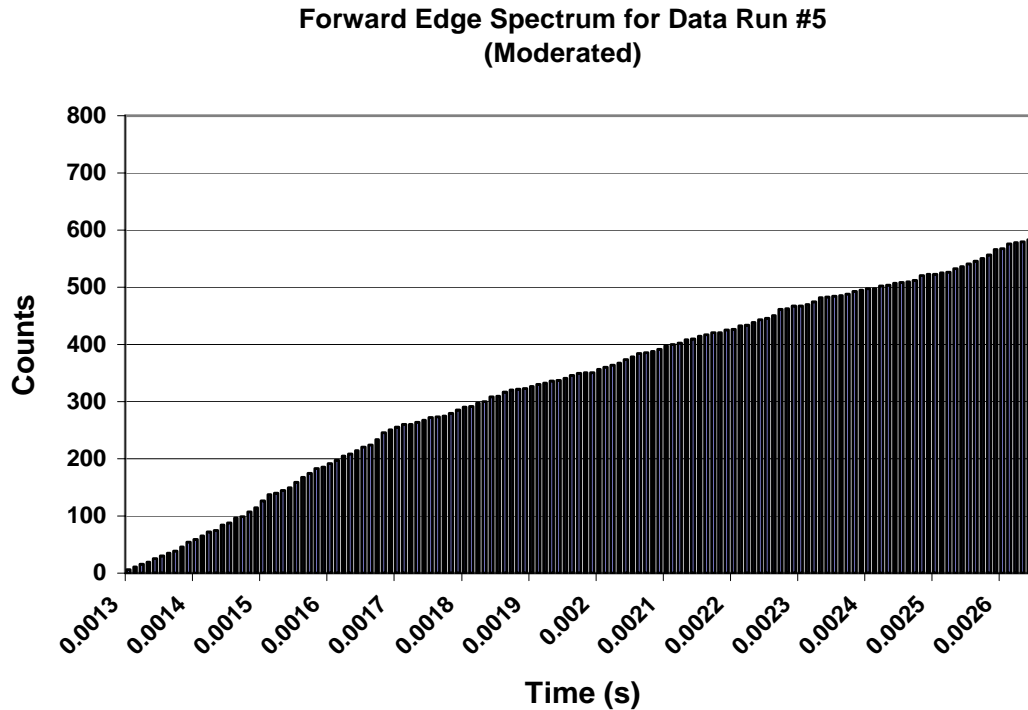
Figure 55: "Forward Edge Spectrum" of neutron events for data run #5

Analysis of WavePro/MATLAB Data

The first three data sets, namely *No moderation & no cadmium, No moderation & cadmium,* and *Moderation & no cadmium,* represent only a small portion of detector to source exposure. Each data set provided approximately 3 ms worth of data; however, of those 3 ms only ~1350 μs were detector to source exposure. For the 1,300 data sets collected, only ~2.03 seconds of actual detector to source exposure time occurred; therefore, very few supportable conclusions can be drawn from these data runs due to poor statistics. In the 2.03 seconds the neutron gate was open 275 counts were recorded. The anticipated thermal neutron count rate of all neutrons for an unmoderated source in the same amount of time is 658 (See Appendix H). The lower count rate can easily, but not quantifiably, be attributed to the presence of moderation.

Although statistically irrelevant, some anticipated responses from the first three data runs are worth mentioning. For data run #1 that had no moderation and no cadmium, an absence of an increased flux in the forward edge spectrum (Figure 45) is not surprising. This absence can be explained in terms of

70

the number of thermal neutrons present in an unmoderated PuBe spectrum. As shown in Figure 6, the thermal neutrons account for a very small fraction of the total flux. Their point of arrival in the spectrum would be imperceptible. The characteristic features of Figure 6, namely the 1.9, 3.1, 4.5, 6.5, 7.7, and 9.7 MeV peaks, would all arrive within the first picoseconds of the first time bin given their unmoderated energy.

The forward edge spectrum of data run #2 (Figure 47) yields results exactly opposite of what would be expected. With the presence of cadmium, no thermal neutron should be expected and therefore a more featureless slope would be expected than in Figure 45, which was acquired without cadmium.

The apparent increase in neutron counts with the opening of the neutron gate observed for data run #3 (Figure 49) would be expected with the presence of the moderation and absence of cadmium. Two significant changes in slope occur at 1480 µs and 1700 µs. If the data collected in data run #3 had been statistically supportable, these two slope increases would have indicated an increased flux of 0.026 eV and 0.006 eV neutrons in the moderated PuBe spectrum.

The results of data runs #4 and #5 were much more promising because of the five fold increase in number of data sets collected. The total source to detector exposure time was roughly 9.47 seconds and allowed for 1256 counts. The expected thermal neutron count from an unmoderated PuBe is 3069 counts, again higher for the same reasons mentioned earlier.

The forward edge spectrum of data run #4 (Figure 53) shows an initial increase in slope beginning at around 1350 µs. Although this in theory would indicate a slight increase in the flux of roughly 0.1 eV neutrons, I believe it is more likely a product of an increase in flux due to the increasing area of detector exposed to source. The unmoderated source experiences down scatter in energy as the high energy neutrons interact with the aluminum disc and moderation in route to the detector. This assertion is merely speculative; however a more interesting feature resides in the latter half of the forward edge spectrum at approximately 2250 µs. The slope begins to decrease. This same feature also presents itself in the forward edge spectrum of the moderated source (Figure 55). This decrease in slope may be attributed to a series of events that occur from the geometry of the disc and the diminishing presence of low energy neutrons that does not occur at any other time during the rotation of the disc chopper. As the neutron gate begins to close,

the depth of aluminum as seen by neutron in flight from the source to the detector begins to increase, but it is not thick enough yet to present much attenuation, thus the only neutrons present are the low energy neutrons that are still in route from the disc to the detector. This number is diminishing, as the area of the detector exposed to the source is diminishing. This feature is depicted as point F in Figure 56.

With the addition of the moderation required to thermalize the 3.1 MeV peak the forward edge spectrum of data run #5 (Figure 55) is produced. Immediately, a distinct difference between the slopes Figure 53 and Figure 55 becomes apparent. A rapid increase in slope occurs around 1460 µs, which equates to an increased flux of 0.026 eV neutrons. The slope continues to increase until approximately 1700 µs, which corresponds to the arrival of the highest flux of thermal neutrons that would occur approximately 200 µs after full opening of the neutron gate. The decrease in slope continues nearly linearly until 2350 µs which was the same trend described for the forward edge spectrum of data run #4.

A comparison of data runs #4 and #5, as depicted in Figure 56, highlights the distinct affect on the presence and absence of moderation on the flux of thermal neutrons. Point A refers to the point at which the first *true* thermal neutrons can possibly arrive at the detector[⊕]. Region B indicates the time in which the amount of detector exposed to the source increases, thus permitting a larger number of thermal neutrons to reach the detector. During this period, the unmoderated slope clearly increases more quickly than the moderated slope. Point C illustrates the point of maximum exposed source-to-detector area, thus the number of thermal neutrons arriving at the detector *spikes*. Point D indicates the point at which the amount of source-to-detector area begins to decrease and correspondingly, the number of thermal neutrons also decreases. Point E represents the time at which the last *true* thermal neutron can arrive at the detector. From this point forward, the number of thermal neutrons arriving at the detector belongs to those high energy neutrons down-scattered in energy by the disc and other surroundings. Point F was described earlier.

[⊕] The timing of the points of interest (A-F) in Figure 56 consider the time-of-flight of the neutrons across the set distance from source to detector.

Forward Edge Spectrums (Moderated vs Unmoderated)
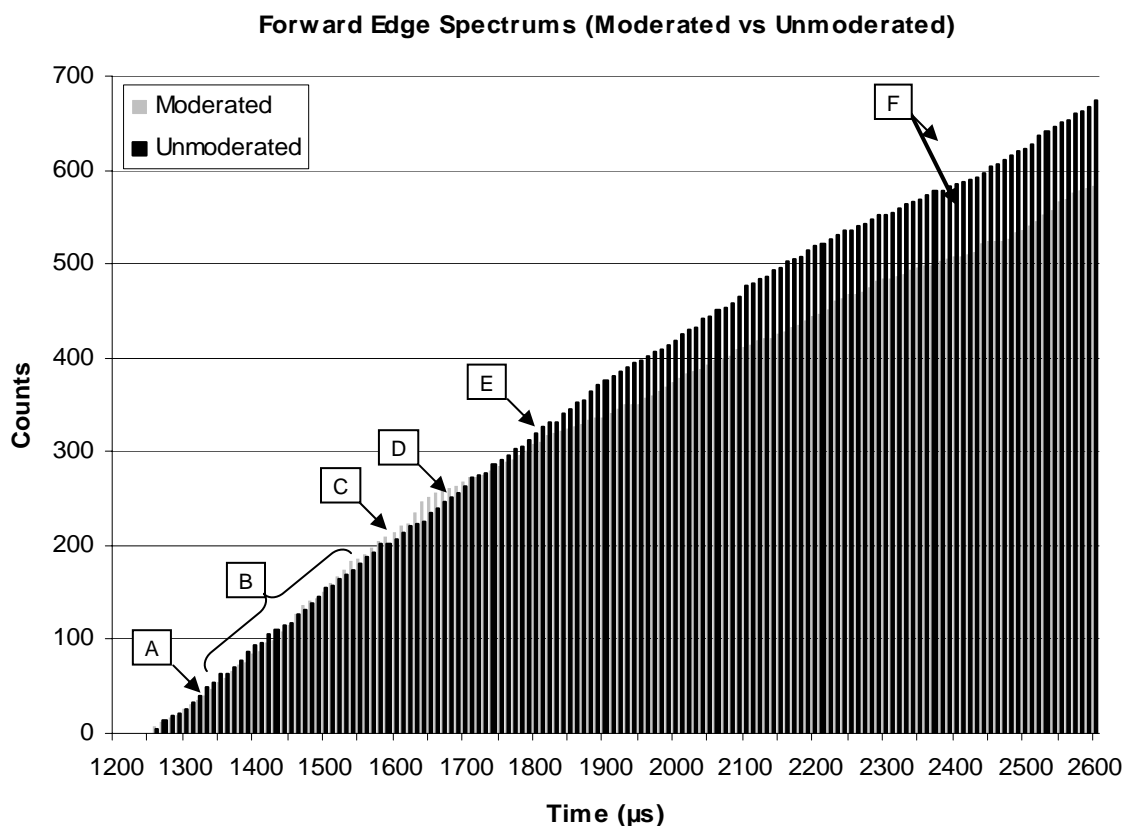
Figure 56: Comparison of forward edge spectra from data run #4 and #5

Error Analysis

The introduction of error in the process of gathering and analyzing the neutron data files are varied and many. Some sources of error, while easily recognizable, are unquantifiable within the scope of this project, while other sources of error are readily quantifiable. The following is an analysis of the WavePro/MATLAB data and its associated error.

As mentioned at the end of chapter III, the photodiode .DAT file was the key to ascribing appropriate time bins for each neutron event. As shown in Figure 57, the photodiode output was a series of 50,000 points in the case of the first three data runs and 25,000 for the last two, each with an associated amplitude value. The peak amplitude value was not a specific point, but rather several points, thus a degree of error is introduced when attempting to pinpoint the exact start time (0 µs).

73
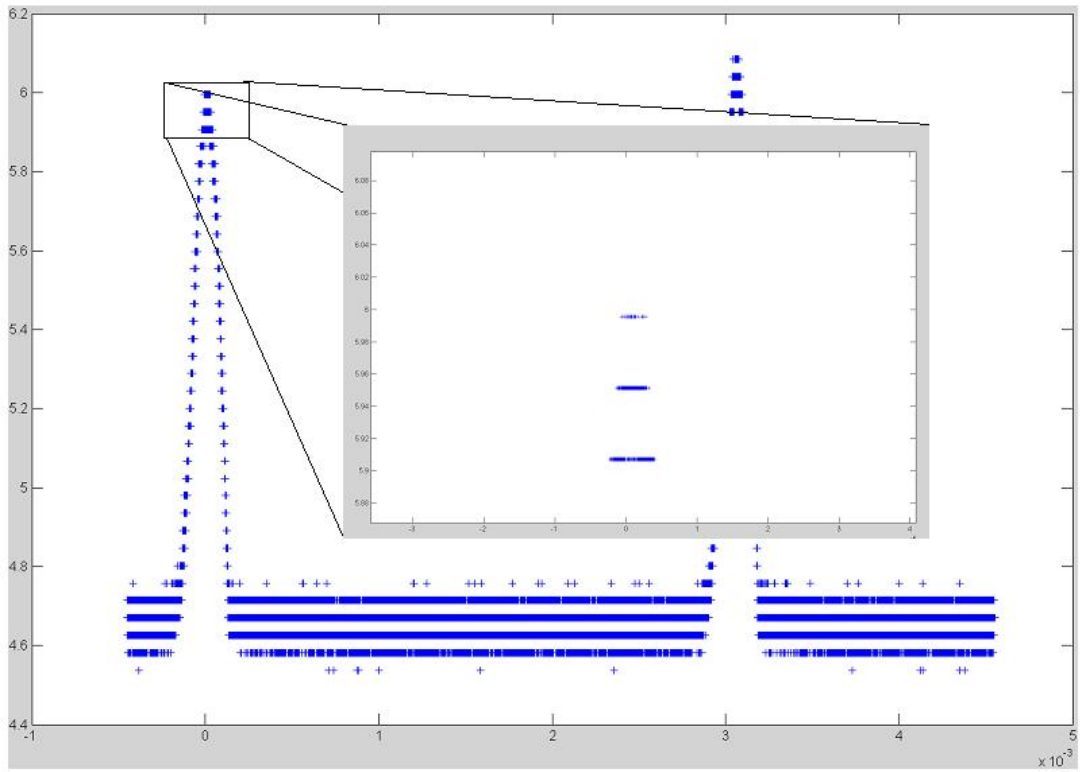
Figure 57: Photodiode .DAT file generated by the 7100 WavePro Oscilloscope (Insert denotes finite points)

Data runs #1 and #3 had an error of +/- 14 μs and +/- 17 μs, respectively, in pinpointing the exact

photodiode peak. Data run #2 had an error of +/- 2 μs. This equates to a range in angular velocity of

1025.96 to 1046.88, 1018.59 to 1041.52, and 1033.76 to 1035.09 rad/sec, respectively. Data runs #4 and #5

had errors of +/- 14 μs and +/- 20 μs. The range of angular velocities for data run #4 and #5 are 1039.53 to

1056.87 and 1034.95 to 1059.67 rad/sec. This source of error could shift the forward energy spectrum bins

by 10 μs either way.

Another source of unquantifiable error lies in the events under the thermal neutron capture peak.

The output produced by the electronics of Figure 25 on the LeCroy Oscilloscope is the voltage pulses

produced by a thermal neutron capture event. Although the majority of the events are thermal neutron

capture, some pulses are created by one of three other mechanisms.

As shown in Figure 39 the thermal capture peak rides on top of both the H^+ recoil continuum and

the Compton scattered electron continuum. With the advent of the TSCA as in Figure 40, most of the

74

Compton electron continuum is discarded, as well as part of the H^+ recoil continuum; however, some counts that show up on the oscilloscope belong to gamma and H^+ events.

One further point of error, although small in comparison to those previously discussed, was the oversight of the delay in electronics. As it turns out, the energy branch incurs a 5.39 µs delay with respect to the photodiode peaks as shown in Figure 58 below. This error can be corrected through a simple delay in the photodiode peak or an extra line of code adjusting the delayed neutron signal in the MATLAB program.
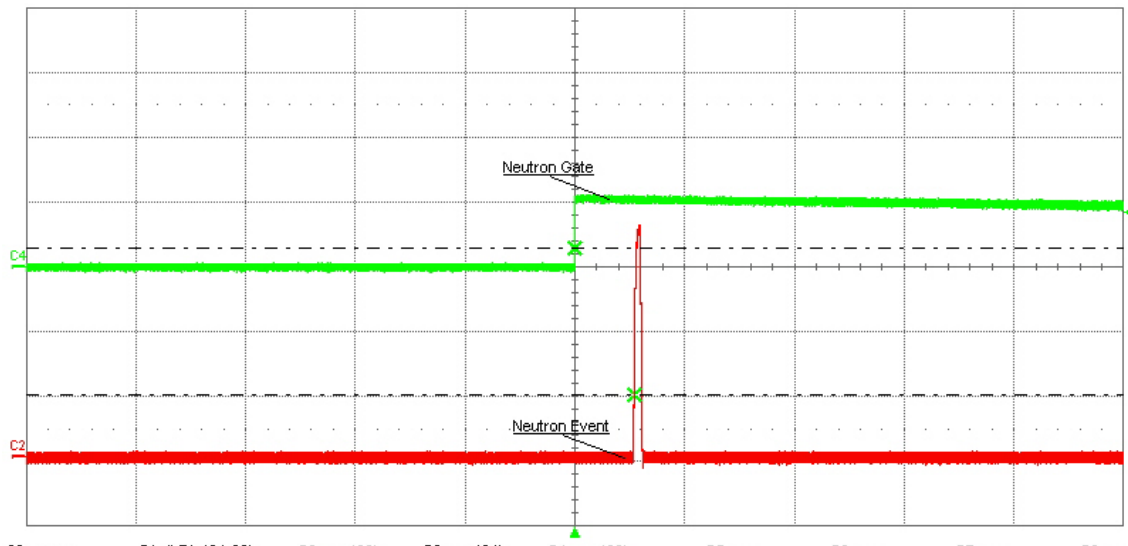
Figure 58: Delay between photodiode trigger and neutron event

Summary

The first three data runs, although statistically insignificant, supported the anticipated finds. The last two data sets showed the most promise in proving the theory of forward edge spectroscopy true. The results of runs #4 and #5 support the expected finds in altering the thermal flux with the presence of moderation.

Various mistakes and oversight introduced error that in retrospect could have been better compensated for or completely overcome. In particular, mistakes made early on during the purchasing and production phase created a great deal of error that could have been overcome with a better understanding of the fundamental behavior of neutron interaction in the various materials at hand. With a more thorough understanding, I am confident that better informed decisions would have led to different dimensions,

materials, and designs; however, hindsight is always 20/20. Some of the error introduced was unavoidable given the constraints of the working environment and materials available. The very nature of the neutron itself leads to error that must be accepted in order to continue forward with the research. The neutrons dynamic interaction with matter is a continuous probabilistic and ultimately statistical process. Efforts in the form of moderation and positioning are the only weapons in combating this problem.

V. Conclusions and Recommendations

Chapter Overview

This chapter summarizes the overall conclusions drawn from the data and experience in the search for a *forward edge* neutron spectroscopy technique. Recommendations for future research based on the hard fought victories and defeats of this project are outlined. Although interesting in terms of laboratory research, the final conclusion of this research indicates that no further funding or effort should be put forward by DTRA or any other interested party in the development of this concept for identification of SNM.

Review of Objectives

1. Select an appropriate detector, to include dimensions, based on neutron modeling

2. Design and produce a neutron disc chopper system

3. Calibrate the system

4. Analyze the data in order to produce a *forward edge* neutron time-of-flight spectrum

Conclusions of Research

In terms of the initially stated objectives, this research effort was a large success. This venture began nearly eight months ago with modeling the response of the detector. With initially little understanding of the concepts, much less the magnitude of this project, the procurement and production of the design came together over the course of several months. The production of the neutron disc chopper was a great milestone in the process and would not have been possible without the expert knowledge and abilities of the AFIT fabrication shop.

Calibrating the system was an exercise in literature review. The ability to calibrate the system based on the use of the Compton edge of three separate isotopes was a critical step in the ability to collect any type of meaningful data. A crucial break through in yet further literature review, coupled with the calibration step, provided the ability to uncover the elusive thermal neutron capture peak, which created the momentum necessary to achieving the collection of data which culminated in the *forward edge spectrums* of the three data runs.

The initial MATLAB codes employed in the analysis of the first three data runs was extremely time consuming; furthermore, the analysis of the collected data provided little in the way of conclusive evidence that the disc was functioning as expected. The advent of the more robust MATLAB code outlined in Appendix G gave rise to the expedited analysis of the neutron data sets. The product of this analysis, the second two data runs, provided indications that the system was in fact able to infer characteristics of a neutron energy spectrum using the forward edge neutron TOF spectroscopy technique. Although the theory and methodology presented in this experiment merits further investigation, a definitive conclusion about the success of this technique remains elusive.

Significance of Research

The design, production, and validation of such a technique as *forward edge* neutron time-of-flight spectroscopy would satisfy a number of DoD requisites in the area of proliferation and counter-proliferation. Its ramifications would be as far reaching as improving the preparedness of the military, revamping nuclear treaty monitoring, and expediting cargo shipments to improve commerce.

Although the ability to conduct neutron energy spectroscopy in the energy range of interest did not present itself in this research effort, a great step was taken in easing the preparation for follow-on research. The learning curve for construction of a disc chopper, implementation of electronics, and analysis of data is well presented in this thesis effort and will provide a solid stepping-stone for follow-on research.

Recommendations for Future Research

1. Although successful in its ability to attenuate some higher energy neutrons, the overall design of the disc chopper needs enhancement. Better incorporation of the cadmium foils is required as well as an increase in the disc diameter. Potential doping of the aluminum with boron may be explored.

2. The physical geometry of the system requires better positioning of moderation in order to reduce the number of counts from the open to closed configuration

3. A higher flux of neutrons would permit fewer data sets to be collected. The OSU reactor may be able to facilitate this project better than the PuBe source on hand.

4. Incorporating or altogether replacing the current organic scintillator with a BF_3 proportional counter in order to observe only thermal neutrons, rather than both all thermal and some fast.

5. Integrate the capture-gated neutron spectrometer method with the current method [9:570] to identify and cut out H^+ events and thermal neutron capture events stemming from a fast neutron.

Appendix A: PuBe Source Specifications

Developer: Monsanto Research Corporation
                   Mound Laboratory
                   Miamisburg, Ohio

Recipient: MCLI-SE-Physics Department
                   C/O Dr. George John
                   Wright-Patterson Air Force Base, Ohio

Date Produced: 25 April 1961[⊕]

Date Acquired: 09 March 1962

Source #:   00303 (WPAFB)
                   M-1170 (Monsanto Research Corp.)

Source Type: ^{239}Pu-Be

Mass Be: 39.28 grams

Mass Pu: 76.36 grams

Container: Tantalum/Stainless Steel

Dimensions: PuBe capsule (Diameter: 0.82 inches)
                              (Height: 3.72 inches)

                   Ta/S.S. Container (Diameter: 1.02 inches)
                                  (Height: 5.52 inches)

Neutron Flux: 9.04×10^6 neutrons/sec (initial flux)

Activity: 5 Ci (initial activity)

[⊕] Based on data from similar shipment. See Reference 16.

Appendix B: PuBe Source Calculations

The subscripts, 1,2,3, and 4, refer to Pu^{239}, Pu^{240}, Pu^{241}, and Am^{241}, respectively. The values for $a_{1,2,4}$ were taken from Fig.1 of the article "Increase in Neutron Yields of Plutonium-Beryllium (α,n) sources", <u>Nuclear Applications</u>, Vol 4, March 1968 by M. Edward Anderson.

In[1]:= $N_a := 6.022 * 10^{23}$ $(*\frac{atoms}{mol}*)$

In[2]:= $T_1 := 24110$ (*half life in years*)
$T_2 := 6564$ (*half life in years*)
$T_3 := 14.35$(*half life in years*)
$T_4 := 432.2$(*half life in years*)

In[6]:= $Mass_{Tot} := 76.36$(*grams*)
$W_1 := .934$ (*% composition of Pu^{239}*)
$W_2 := .061$ (*% composition of Pu^{240}*)
$W_3 := .0055$(*% composition of Pu^{241}*)

NOTE: The above % composition of the Plutonium was taken from Table III of the aforementioned article, "Increase in Neutron Yields of Plutonium-Beryllium (α,n) sources". I assumed the % composition of this source, M-1170, was similar to that of M-1127. No Am^{241} is present at "birth".

In[10]:= $Mass_1 = Mass_{Tot} * W_1$(*g*);
$Mass_2 = Mass_{Tot} * W_2$(*g*);
$Mass_3 = Mass_{Tot} * W_3$(*g*);

In[13]:= $AM_1 := 239.052156$(*$\frac{g}{mol}$*)
$AM_2 := 240.053808$(*$\frac{g}{mol}$*)
$AM_3 := 241.0568453$(*$\frac{g}{mol}$*)

In[16]:= $N_1 = \frac{Mass_1}{AM_1} * N_a$; (*number of Pu^{239} atoms present initially*)
$N_2 = \frac{Mass_2}{AM_2} * N_a$; (*number of Pu^{240} atoms present initially*)
$N_3 = \frac{Mass_3}{AM_3} * N_a$; (*number of Pu^{241} atoms present initially*)

In[17]:= $\lambda_1 = \frac{Log[2]}{T_1}$; (*decay constant*)
$\lambda_2 = \frac{Log[2]}{T_2}$;
$\lambda_3 = \frac{Log[2]}{T_3}$;
$\lambda_4 = \frac{Log[2]}{T_4}$;

The "birth date" of the source is approximately 4/25/61 based on Table III source number M-1127, which is the source closest in fabrication date to this source M-1170. The following equation solves for the initial neutron yield at the "birth date". Note: The time elapsed from "birth date" to the date of measurement (3/9/1962) is $t \approx 318/365$

In[20]:= $Q_1 := 9.04 * 10^6$ (*3/9/1962*)

In[21]:= $Q_0 = Q_1 \Big/ \Big(1 + 1.23 * \Big(\frac{\lambda_4 \lambda_3 N_3}{(\lambda_1 N_1 + \lambda_2 N_2)(\lambda_3 - \lambda_4)} \big(Exp[-\lambda_4 \frac{318}{365}] - Exp[-\lambda_3 \frac{318}{365}]\big)\Big)\Big)$;

In[22]:= $Q[t\_] = Q_0 \Big(1 + 1.23 * \Big(\frac{\lambda_4 \lambda_3 N_3}{(\lambda_1 N_1 + \lambda_2 N_2)(\lambda_3 - \lambda_4)} (Exp[-\lambda_4 t] - Exp[-\lambda_3 t])\Big)\Big)$;

The above equation yields the activity of the source since its "birth" in 1962.
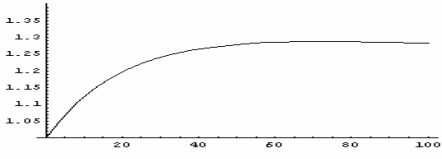
In[23]:= $Date[] - \{1961, 6, 0, 0, 0, 0\}$
Out[23]= $\{44, -4, 17, 11, 47, 40.6406250\}$
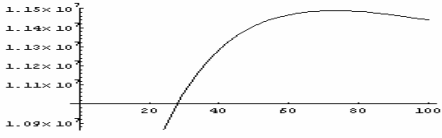
In[24]:= $Q[0]$ (*Neutron flux at birth*)
Out[24]= 8.92117915×10^6

In[25]:= $Q[43.4]$
Out[25]= 1.133814431×10^7

This is the present flux [n/s] of neutrons emitted by the PuBe source

In[26]:= $<<$ Graphics`Graphics`

In[27]:= $Plot\Big[\frac{Q[t]}{Q_0}, \{t, 0, 100\}, PlotRange \rightarrow \{1.0, 1.4\}\Big]$

Out[27]= - Graphics -

In[28]:= $Plot[Q[t], \{t, 0, 100\}]$

Out[28]= - Graphics -

In[29]:= $Solve[\partial_t (Q[t]) == 0, t]$
Out[29]= $\{\{t \rightarrow 72.91646021\}\}$

In[30]:= $Q[72.9164602138331`]$
Out[30]= 1.148808392×10^7

Note of Interest: The source will reach its maximum flux sometime in the year 2033 and it will be approximately 1.15×10^7 n/s

Appendix C: Disc Chopper Schematics
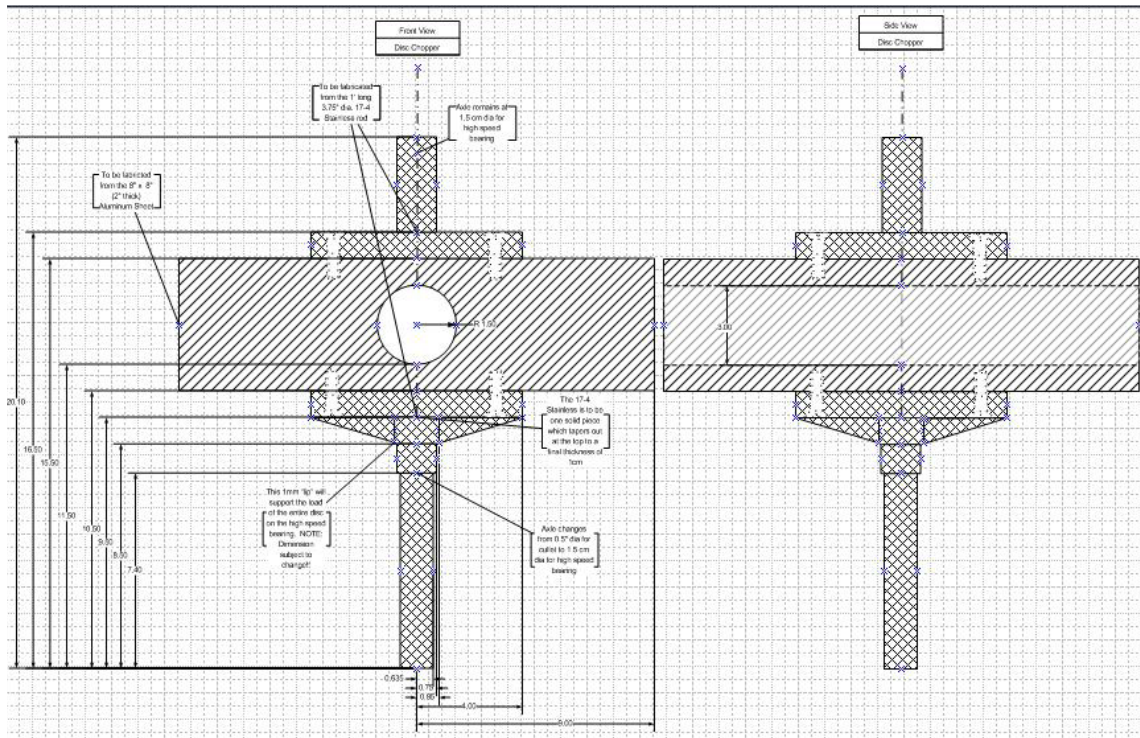
Figure 59: Disc chopper schematic - (Disc Side View)
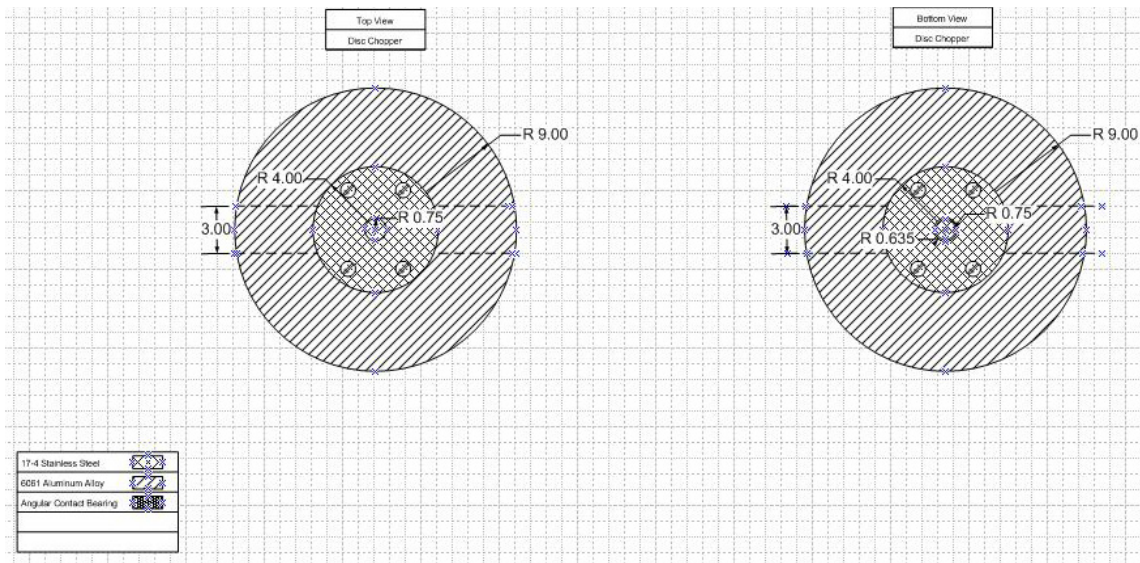
Figure 60: Disc chopper schematic - (Disc Top View)
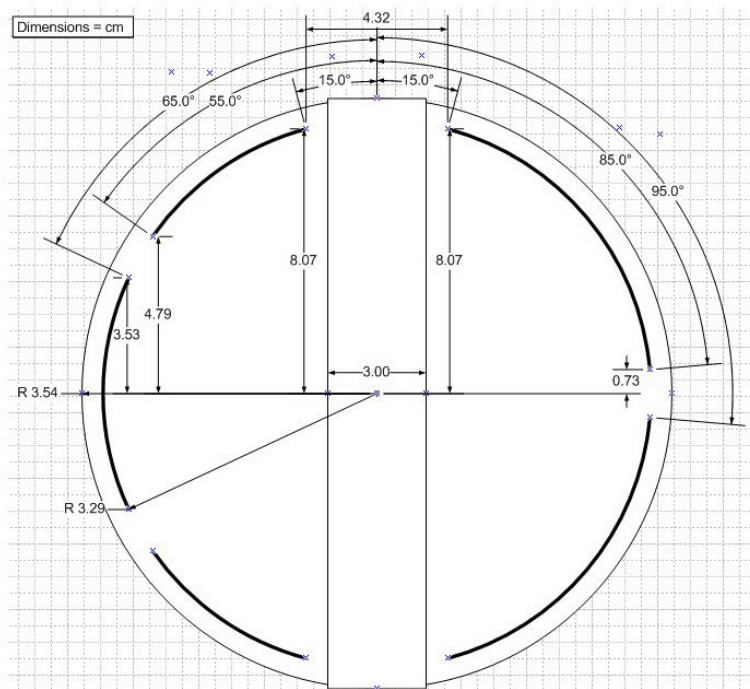
Figure 61: Disc chopper schematic - (Cadmium Placement)
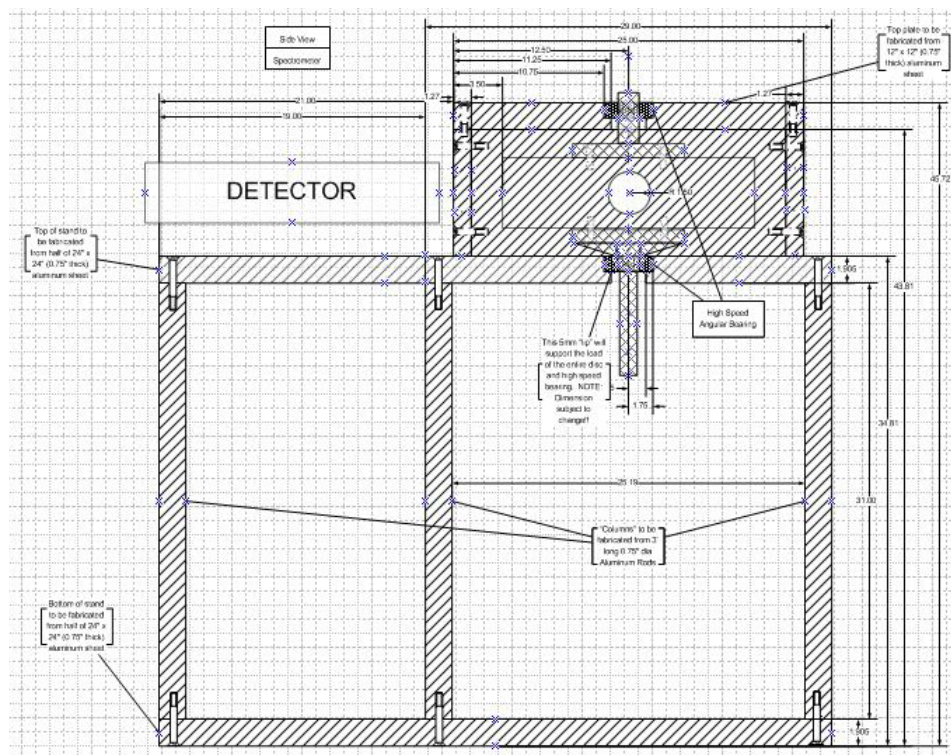
Figure 62: Disc chopper schematic - (Disc Housing Side View)
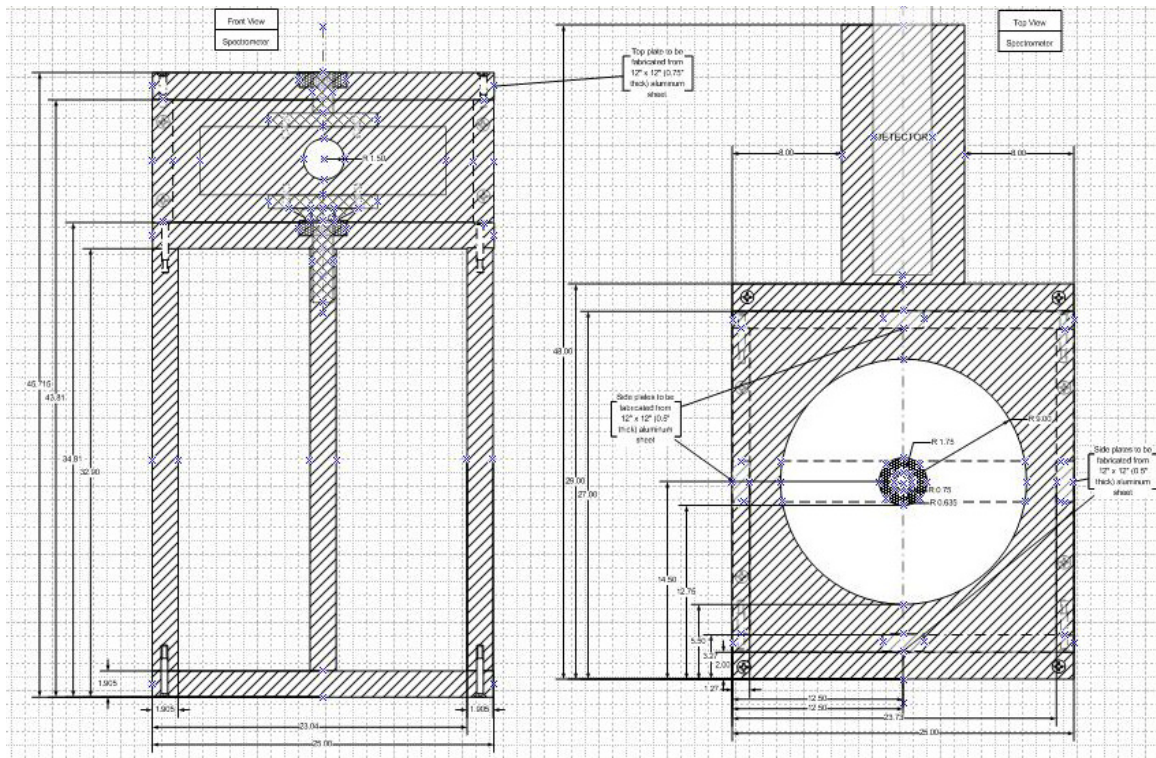
Figure 63: Disc chopper schematic - (Disc Housing Side and Top View)
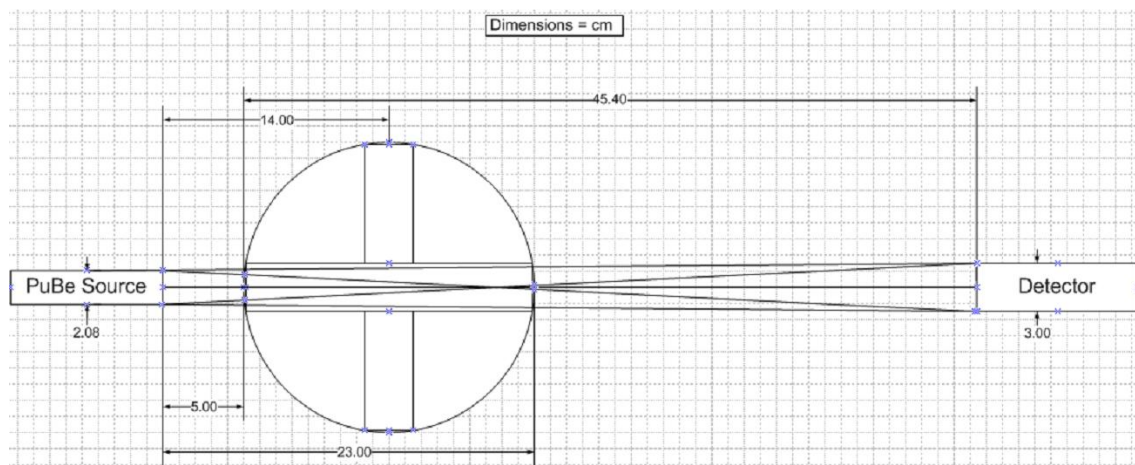
Figure 64: Solid angle relationship configuration of PuBe source, disc chopper and detector

The Monte Carlo N-Particle (MCNP) Transport Code System is a "general-purpose, continuous-energy, generalized geometry, time-dependent, coupled neutron-photon-electron Monte Carlo code system" [34:iii]. MCNP utilizes an input code that incorporates the subject's geometry (i.e. detector geometry) and orientation, source strength and direction, and material composition. It calculates a variety of outputs some of which include current across a surface, energy absorbed in a volume, and surface flux.

An example copy of the detector input file, along with narrative comments in bold print, follows:

NOTE: The cell cards define each cell of the detector, as well as the volume outside the detector. Line 1 states that the cell is free space (0) and encompasses everything outside of surface 1 (cylinder of radius 1.5 cm), everything left of surface 2 (a plane located at 0 cm on the y axis), and everything right of surface 27 (a plane located at 10 cm on the y axis). The surface locations are defined later. The neutrons in this region are of zero importance (imp:n=0).
Line 2 states that the cell is comprised of material 1 (defined later), has a density of 0.916 g/cm^3 and encompasses everything inside of surface 1, right of surface 2, and left of surface 3. The neutrons in this region are of total importance (imp:n=1).

```
c cell cards for detector
1   0                1:-2:  27        imp:n=0      $zero importance universe
2   1   -0.916   -1  2     -3         imp:n=1      $0.4 cm detector slice
3   1   -0.916   -1  3     -4         imp:n=1      $0.4 cm detector slice
4   1   -0.916   -1  4     -5         imp:n=1      $0.4 cm detector slice
5   1   -0.916   -1  5     -6         imp:n=1      $0.4 cm detector slice
6   1   -0.916   -1  6     -7         imp:n=1      $0.4 cm detector slice
7   1   -0.916   -1  7     -8         imp:n=1      $0.4 cm detector slice
8   1   -0.916   -1  8     -9         imp:n=1      $0.4 cm detector slice
9   1   -0.916   -1  9     -10        imp:n=1      $0.4 cm detector slice
10  1   -0.916   -1  10    -11        imp:n=1      $0.4 cm detector slice
11  1   -0.916   -1  11    -12        imp:n=1      $0.4 cm detector slice
12  1   -0.916   -1  12    -13        imp:n=1      $0.4 cm detector slice
13  1   -0.916   -1  13    -14        imp:n=1      $0.4 cm detector slice
14  1   -0.916   -1  14    -15        imp:n=1      $0.4 cm detector slice
15  1   -0.916   -1  15    -16        imp:n=1      $0.4 cm detector slice
16  1   -0.916   -1  16    -17        imp:n=1      $0.4 cm detector slice
17  1   -0.916   -1  17    -18        imp:n=1      $0.4 cm detector slice
18  1   -0.916   -1  18    -19        imp:n=1      $0.4 cm detector slice
19  1   -0.916   -1  19    -20        imp:n=1      $0.4 cm detector slice
20  1   -0.916   -1  20    -21        imp:n=1      $0.4 cm detector slice
21  1   -0.916   -1  21    -22        imp:n=1      $0.4 cm detector slice
22  1   -0.916   -1  22    -23        imp:n=1      $0.4 cm detector slice
23  1   -0.916   -1  23    -24        imp:n=1      $0.4 cm detector slice
24  1   -0.916   -1  24    -25        imp:n=1      $0.4 cm detector slice
25  1   -0.916   -1  25    -26        imp:n=1      $0.4 cm detector slice
26  1   -0.916   -1  26    -27        imp:n=1      $0.4 cm detector slice
c end of cell cards for detector
```

NOTE: The surfaces are defined on a Cartesian coordinate system. Line 1 defines a cylinder with radius 1.5 cm whose center lies on the y axis. Line 2 defines a plane perpendicular to the y axis located at the origin (0 cm).

```
c beginning of surfaces
1 CY 1.5
2 PY 0
3 PY 0.4
4 PY 0.8
5 PY 1.2
6 PY 1.6
7 PY 2.0
```

```
8 PY 2.4
9 PY 2.8
10 PY 3.2
11 PY 3.6
12 PY 4.0
13 PY 4.4
14 PY 4.8
15 PY 5.2
16 PY 5.6
17 PY 6.0
18 PY 6.4
19 PY 6.8
20 PY 7.2
21 PY 7.6
22 PY 8.0
23 PY 8.4
24 PY 8.8
25 PY 9.2
26 PY 9.6
27 PY 10.0
c end of surfaces
```

NOTE: The energy source is a neutron emitting source located on surface 2. It is uniformly distributed on surface 2. It is a monoenergetic source (erg=10 MeV) and is preferentially directed in the positive y direction (dir=1)

```
c energy source
sdef sur=2 Pos=0 0 0 dir=1 erg=10
```

NOTE: The composition of the detector references an Engineering Nuclear Data File (ENDF) using a ZAID format such as 6012.40c, which references the total neutron cross-section for Carbon-12. The numbers following the ZAID are the mole concentrations.

```
c material properties
m1 nlib=60c 1001 0.558 6012.40c 0.321 8016.00c 0.091 5010.03d .027 5011.40c .003
```

NOTE: The Tally cards list the desired output. The neutrons with energies ranging from 14 to 0 MeV (phys:n 14 0) are all considered in the Monte Carlo process. The desired output here is the flux of neutrons with energies equal to 0.000005 MeV (E2:n 0.000005) across the various surfaces (F2:n 3 4 5…). The number of particles starting at the surface is 1.1E7 (nps 11000000).

```
c Tally cards
phys:n 14 0
E2:n 0.000005
F2:n 3 4 5 6 7 8 9 10 11 12 13 14 15 16 17 18 19 20 21 22 23 24 25 26 27
c
nps 11000000
print
ctme
```

The MCNP output files are very large text files, so only the relevant data has been included below.

The example output was derived from the above input file.

NOTE: The weighted flux of neutrons with energy equal to 5.0000E-06 MeV across surface 3 (defined above) is 1.39254E-06 with an error of +/- 0.1610. In order to calculate the actual number crossing, multiply by the initial number of neutrons 1.1E07 for a total of 15.31795 +/- 2.46619 neutrons/cm^2.

```
surface   3
      energy
    5.0000E-06   1.39254E-06 0.1610
surface   4
      energy
    5.0000E-06   2.39594E-06 0.1621
surface   5
      energy
    5.0000E-06   2.58501E-06 0.1185
surface   6
      energy
    5.0000E-06   2.53529E-06 0.1149
surface   7
      energy
    5.0000E-06   2.62701E-06 0.1146
```

```
surface  8
     energy
  5.0000E-06   3.25466E-06 0.1205
surface  9
     energy
  5.0000E-06   2.85427E-06 0.1085
surface  10
     energy
  5.0000E-06   3.79300E-06 0.1114
surface  11
     energy
  5.0000E-06   3.54144E-06 0.1495
surface  12
     energy
  5.0000E-06   3.08410E-06 0.0993
surface  13
     energy
  5.0000E-06   4.03470E-06 0.1658
surface  14
     energy
  5.0000E-06   3.95547E-06 0.1295
surface  15
     energy
  5.0000E-06   3.28399E-06 0.1228
surface  16
     energy
  5.0000E-06   2.85660E-06 0.1360
surface  17
     energy
  5.0000E-06   2.81638E-06 0.0987
surface  18
     energy
  5.0000E-06   3.17060E-06 0.1259
surface  19
     energy
  5.0000E-06   3.34320E-06 0.1315
surface  20
     energy
  5.0000E-06   2.62908E-06 0.1428
surface  21
     energy
  5.0000E-06   2.70013E-06 0.1575
surface  22
     energy
  5.0000E-06   3.37462E-06 0.1693
surface  23
     energy
  5.0000E-06   1.85543E-06 0.1774
surface  24
     energy
  5.0000E-06   2.05288E-06 0.2036
surface  25
     energy
  5.0000E-06   1.66829E-06 0.1402
surface  26
     energy
  5.0000E-06   1.04979E-06 0.1503
surface  27
     energy
  5.0000E-06   6.66959E-07 0.1975
```
        Several MCNP runs were made with varied initial energies from 1 to 10 MeV. Figures 18-20 are

graphs of the MCNP output of the flux of 0.5 eV neutrons/cm^2 through the BC-523A Organic Scintillator

material for 1, 3.1, and 10 MeV neutrons using the aforementioned MCNP input card.

86
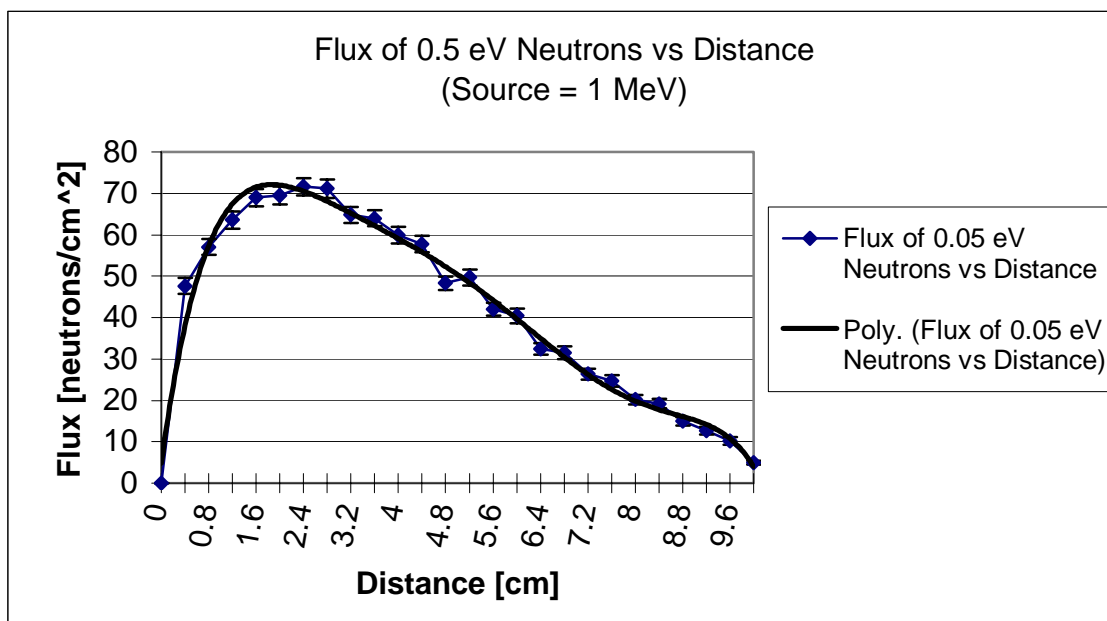
Figure 65: Flux of 0.5 eV neutrons through BC-523A Organic Scintillator (Source Strength = 1 MeV)

The value of 0.5 eV approximates the value of a thermalized neutron, which is actually 0.0253 eV at standard room temperature [35:73]. The MCNP program produced extremely large error in the flux value when flux energies of below 0.5 eV were attempted. As shown in Figure 65, the peak thermalization for a 1 MeV neutron occurs between 2.4 and 2.8 cm. As the energy of the neutron source is increased, the peak thermalization begins to move further back in the detector depth. Figure 66 has a peak thermalization at around 3.0 cm for 3.1 MeV incident neutrons, while the peak thermalization for the 10 MeV source in Figure 67 occurs between 4.4 and 4.8 cm. This movement in peak thermalization is a product of both the elastic and inelastic scattering
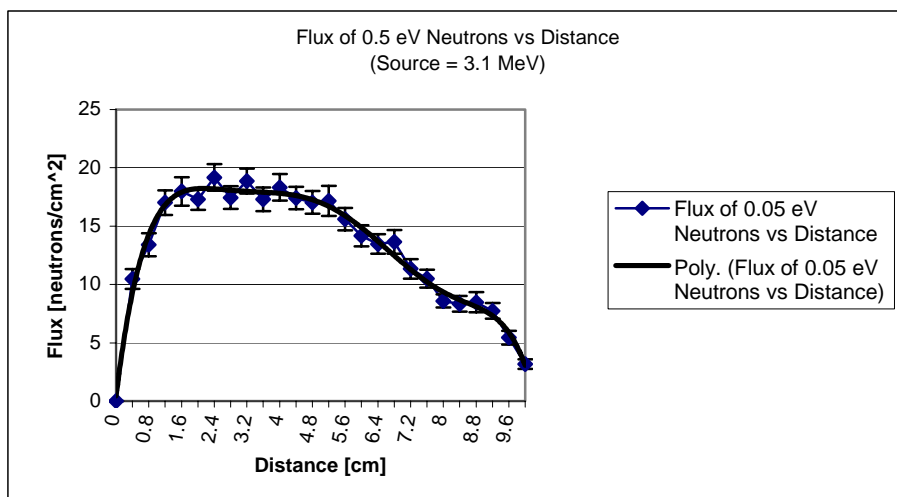
Figure 66: Flux of 0.5 eV neutrons through BC-523A Organic Scintillator (Source Strength = 3.1 MeV)
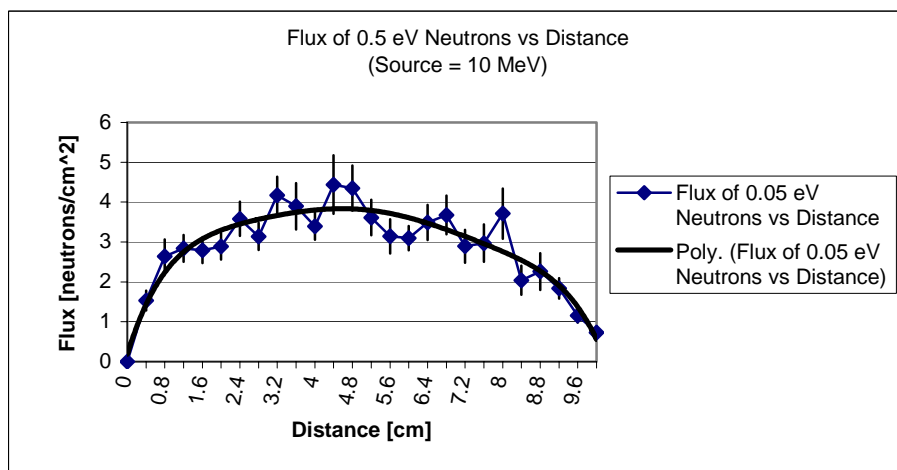
Figure 67: Flux of 0.5 eV neutrons through BC-523A Organic Scintillator (Source Strength = 10 MeV)

of the neutron, which serves to moderate the neutron, and the thermal capture of the neutron once energies drop down to the point where the Boron-10 thermal capture cross-section dominates. Thus through the output of the modeling, the expectation of this particular BC-523A organic scintillation detector is that it will produce a rather large thermal capture peak, while producing relatively few proton recoil events in the energy spectrum of an unmoderated PuBe source.

Appendix E: PSA & TAC Adjustments

Integration Settings

The DLA has three different integration settings. The rise time of the output pulses from the DLA are a function of the rise time furnished from the preamp and of the setting of the front panel integration switch (Integ). When the switch is set at 0.04 µs, the rise time for a step input from the preamp is less than 100 ns. The 0.1 µs and 0.25 µs switch settings will provide proportionately longer rise times [26:4]. The rise time of the pulse produced by the DLA establishes the trigger points for the start and stop pulse produced by the PSA and subsequently sent to the TAC. Figure 68 provides a typical DLA output pulse with Integ = 0.1 µs. The pulse is fairly symmetric. The integration setting of 0.04 µs provides better symmetry, while 0.25 µs is more asymmetric.
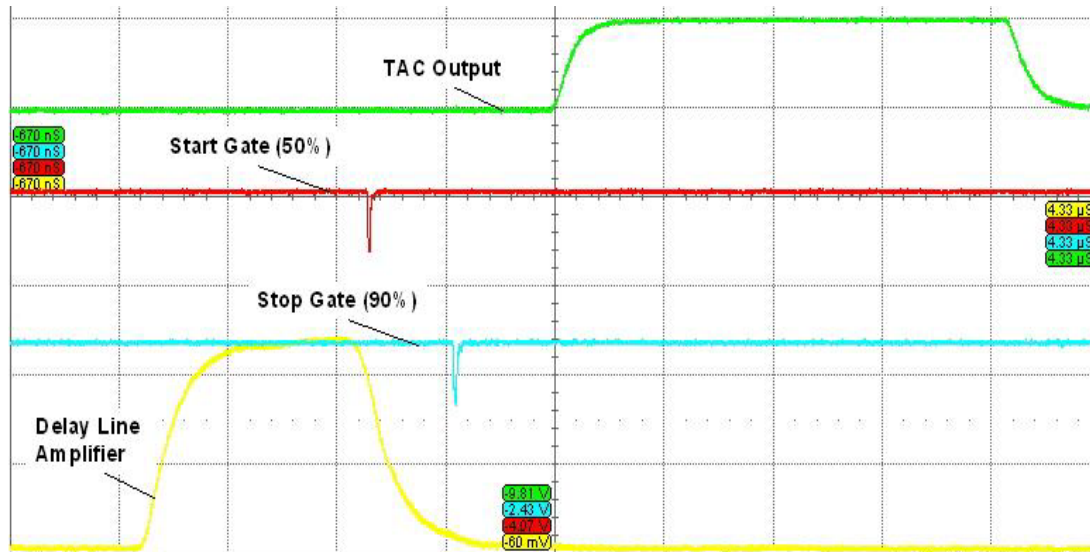
Figure 68: DLA, PSA (Start and Stop Signal), and TAC oscilloscope output

Although the symmetry is somewhat improved at the 0.04 µs setting, other problems, such as the creation of spurious start gates as shown in Figure 69, prohibit the use of this setting for data collection purposes.
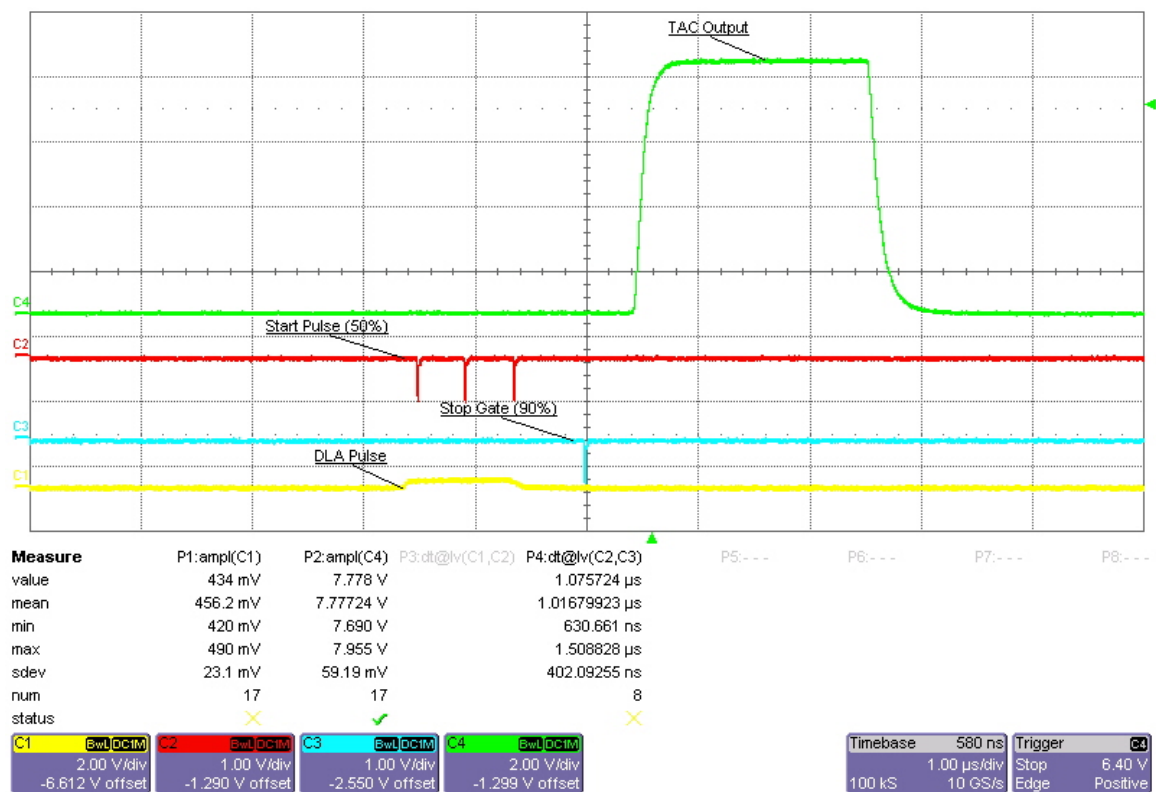
Figure 69: "Spurious" start gates created by the PSA (Integ = 0.04 μs)

The TAC output, as shown in Figure 68 and Figure 69, was sent through a TSCA to an Analog to Digital Converter (ADC), which then fed the signal to a Multi-Channel Analyzer (MCA) via an Acquisition Interface Module (AIM). The MCA output in Figure 70-Figure 72, which is a TAC voltage pulse representative of the time between the start and stop peak, was dramatically affected by the integration setting, as would be expected with the change in symmetry of the DLA output pulse. The *spurious* start gates created by the PSA for the integration setting of 0.04 μs created *ghost* peaks at both 650 μs and 1075 μs. As shown in the measurement readout in Figure 69, the TAC output generated by the time difference in the first *spurious* start gate and the stop gate was 1075.724 ns, exactly where the second ghost peak resided in Figure 70.
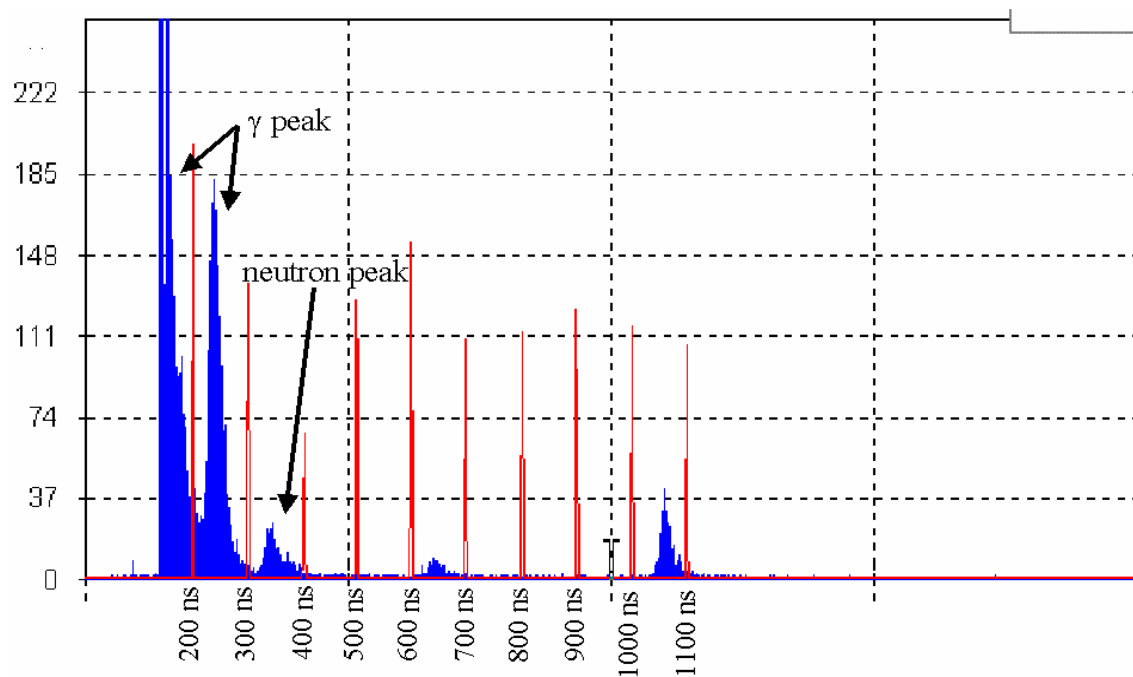
Figure 70: TAC output with DLA integration switch set to 0.04 μs
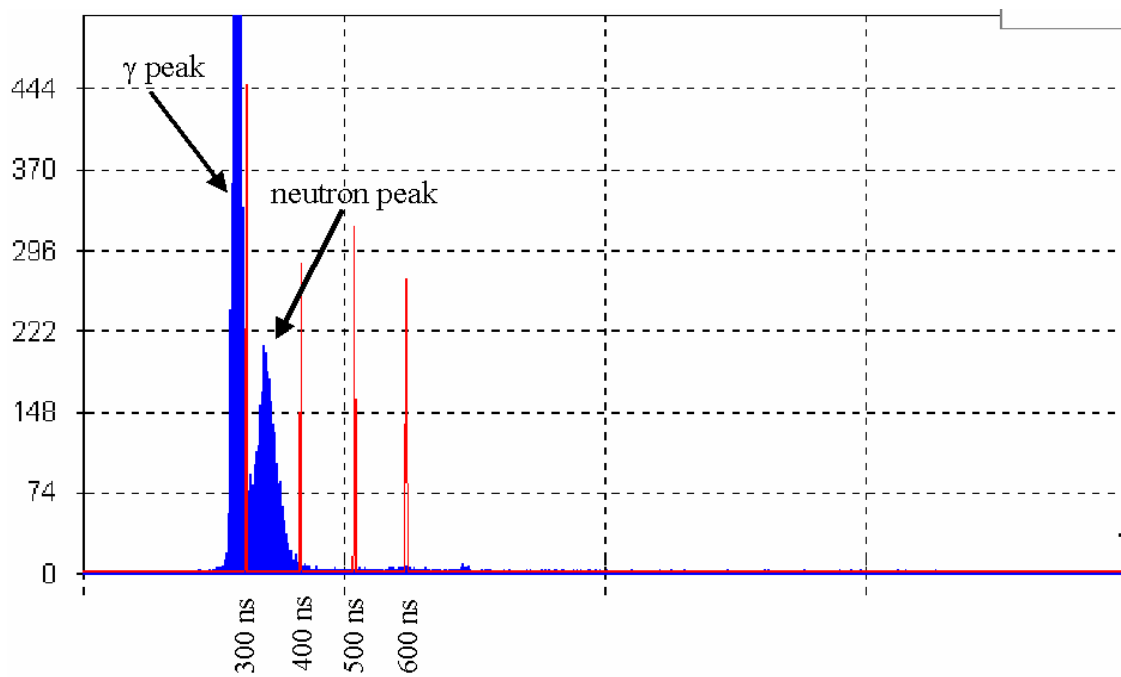
Figure 71: TAC output with DLA integration switch set to 0.1 μs
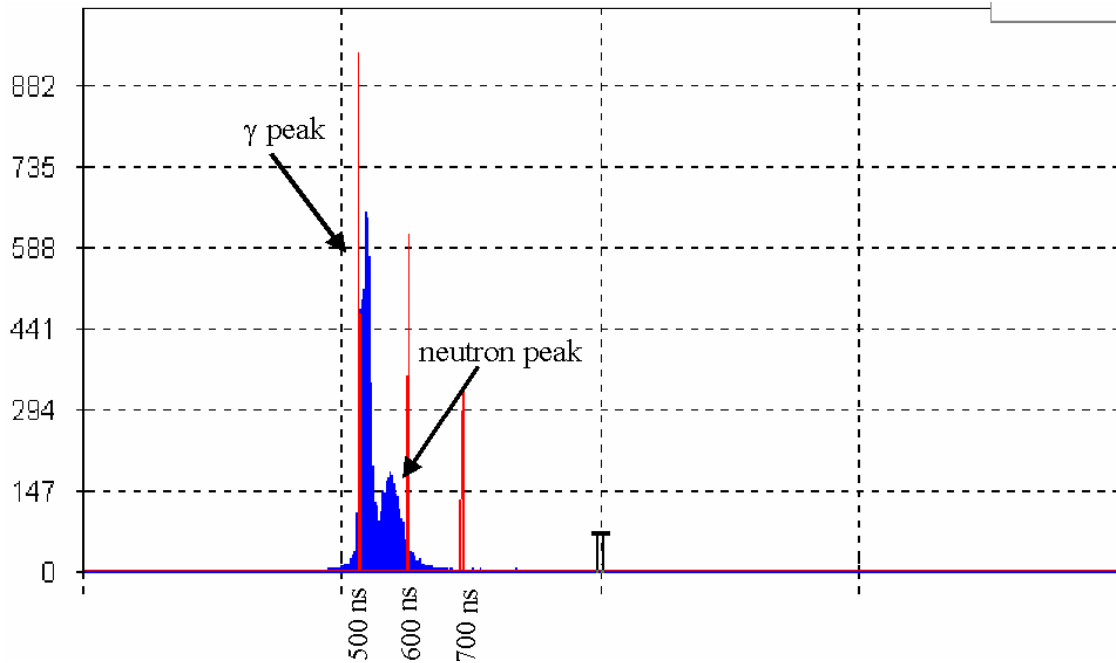
Figure 72: TAC output with DLA integration switch set to 0.25 μs

The second two figures above, Figure 71 and Figure 72 are MCA outputs of the TAC for an integration setting of 0.1 μs and 0.25 μs, respectively. Neither of these settings produced *spurious* start gates; however, the 0.1 μs setting provided more baseline resolution in separating the gamma events from the neutron events, thus 0.1 μs was used throughout this experiment.

Channel A Constant Fraction Setting

In addition to issues with the integration settings of the DLA, the trigger point for the start gate required a degree of refinement. An internal jumper selects the constant fraction that was used for the channel A response point; jumper positions were 10%, 20%, and 50%, referring to the decay from the peak of the input DLA waveform [27:4]. With the jumper positioned for 10% and 20% settings, the PSA was unable to accurately detect the true 10% and 20% decay point part of the time, thus *spurious* start gates as shown in Figure 73 were created independent of the integration setting on the DLA.

Figure 73: Spurious Start Gate created by PSA due to A-channel constant fraction setting of 10%

Figure 74: TAC output with PSA A-channel constant fraction setting of 10%
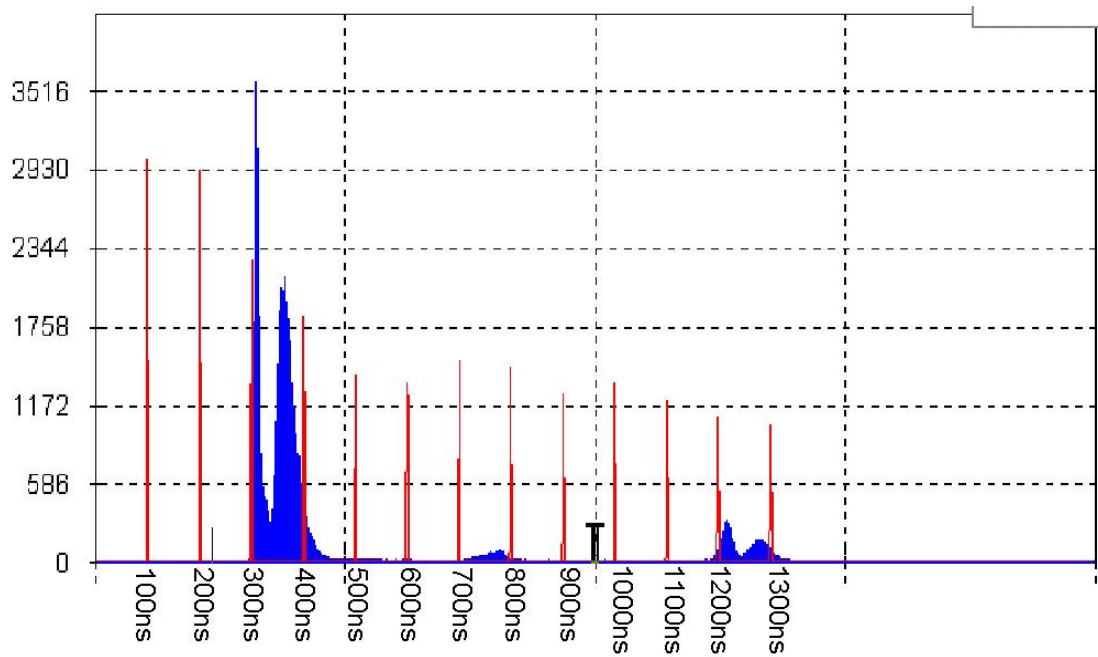
Figure 75: TAC output with PSA A-channel constant fraction setting of 20%
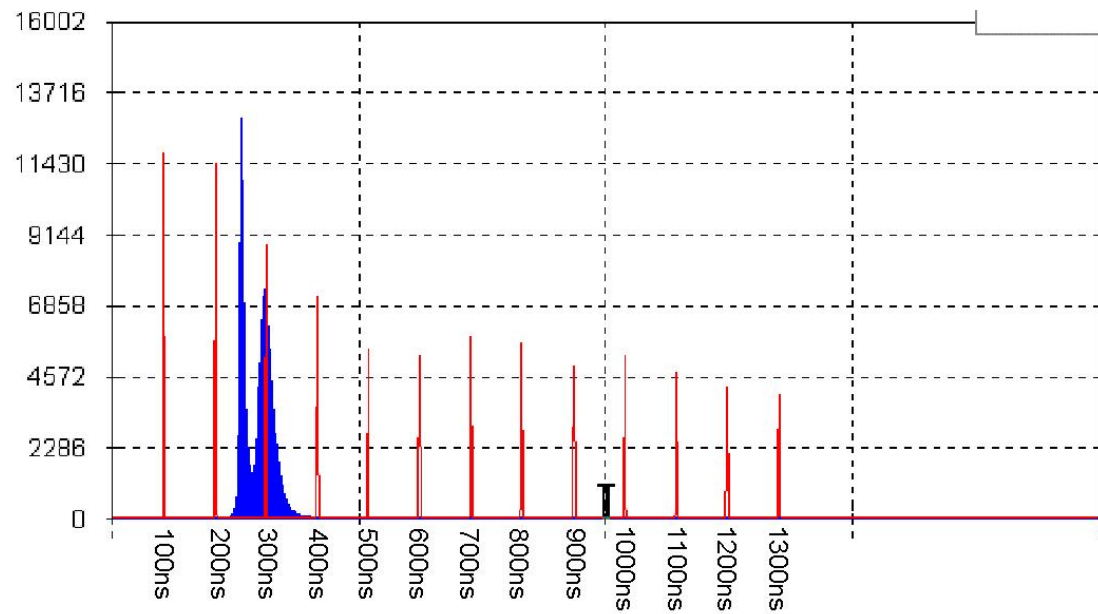
Figure 76: TAC output with PSA A-channel constant fraction setting of 50%

The MCA output for the three A-channel constant fraction settings are seen in Figure 74-Figure 76. The measurement readout from Figure 73 of the time difference between the start and stop pulse is

94

1303.881 ns, which corresponds to the last *ghost* peak in Figure 74. Armed with this knowledge an A-channel constant fraction setting of 50% was the clear choice for the PSA.

Signal Amplification

One final issue existed with the DLA. A high degree of signal distortion was witnessed even at the low amplification setting of x5. The severity of the distortion increased with amplification The signal distortion occurred at the return to baseline of the DLA output pulse as shown in Figure 77 below. Variations on the LLD and ULD of the ORTEC 552 were made in order to overcome this problem. Settings of the LLD and ULD to observe only the low amplitude energy outputs of the DLA (P), which would obviously be associated with the thermal capture peak, presented ghost peaks similar to those shown above. The same results were seen when the LLD and ULD were set to see all energy pulses (0-10V) produced by the DLA (P). LLD and ULD settings in between were also conducted in association with a variety of DLA (P) amplification settings. All settings presented ghost peak type output from the TAC. In the case of the ghost peaks, experimental results proved that the two peaks consisted of both gamma and neutron events, thus the ability to conduct pulse shape analysis for this over-amplified pulse was completely degraded. A separate branch line including another ORTEC 460 Delay Line Amplifier (DLA (E)), as shown in Figure 21, was created for the energy analysis part of this experiment.
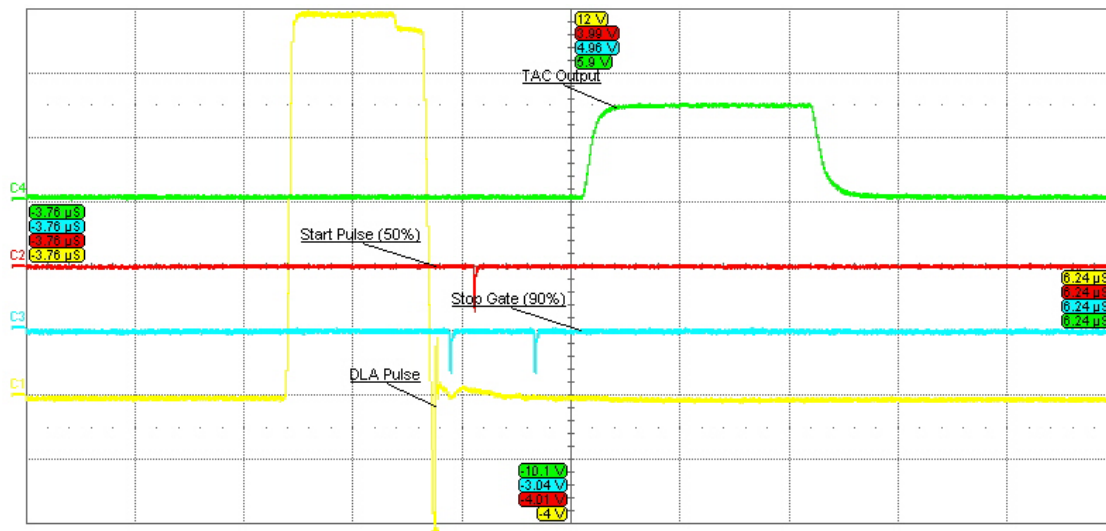
Figure 77: Distortion of DLA output pulse caused by over-amplification

95

As it turns out, the amplification required in the DLA (E) to conduct analysis of the thermal capture peak was so high that no corresponding TAC output was being produced in the PSA branch. The inability to amplify the DLA (P) above x5 prevented a TAC output identifying the phosphorescent decay following a Li^+ or α event (i.e. neutron capture). With the TSCA (ORTEC 551) of the PSA branch set with a LLD=0 and a ULD=10, thus identifying all gamma and neutron pulses from the DLA (P), a measurement of the TAC output in coincidence and anticoincidence with the energy spectrum provided by the energy branch via the LG&S 2 can be seen in Figure 78.
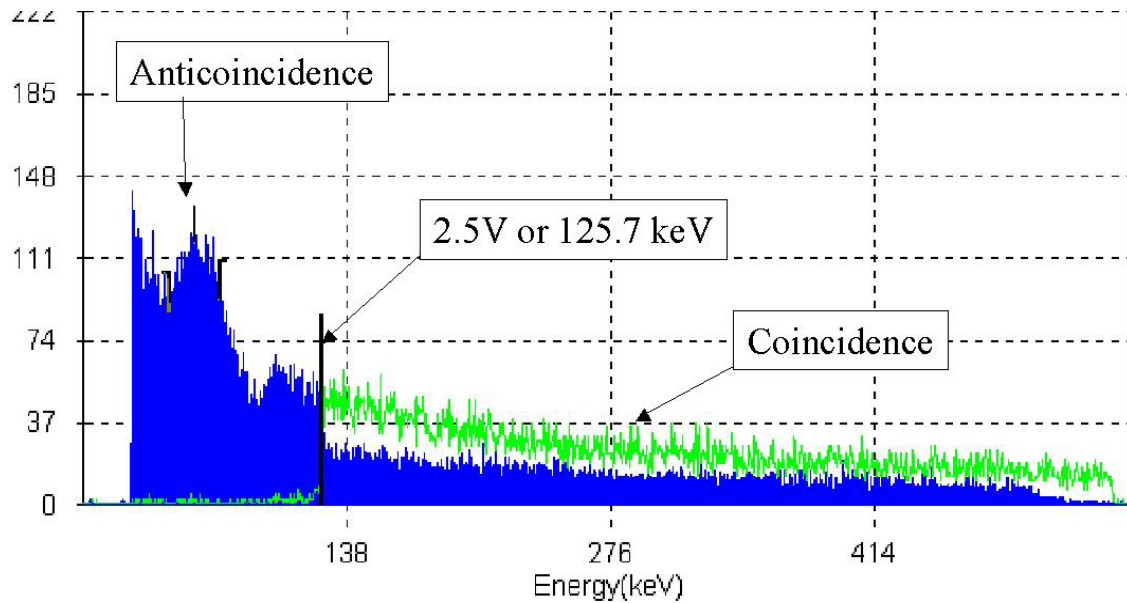
Figure 78: Coincidence/anticoincidence of PuBe energy spectrum and TAC output of all events (α and γ)

The thermal capture peak in the energy spectrum only shows up when run in anticoincidence with the TAC output from the PSA branch. Neutron and gamma events below 125.7 keV did not generate a TAC output in the PSA branch. The inability to amplify the DLA (P) overall prevented the use of PSA in discriminating against those Compton scattered electrons (i.e. gamma events) under the thermal capture peak.

Appendix F: Energy Spectrum Calibration and Output

The addition of the second DLA (E) allowed for better observation of the lower energy spectrum of the incident radiation. The x5 amplification utilized in the DLA (P) could not resolve the thermal neutron capture peak in the PuBe energy spectrum as shown in Figure 79 below.
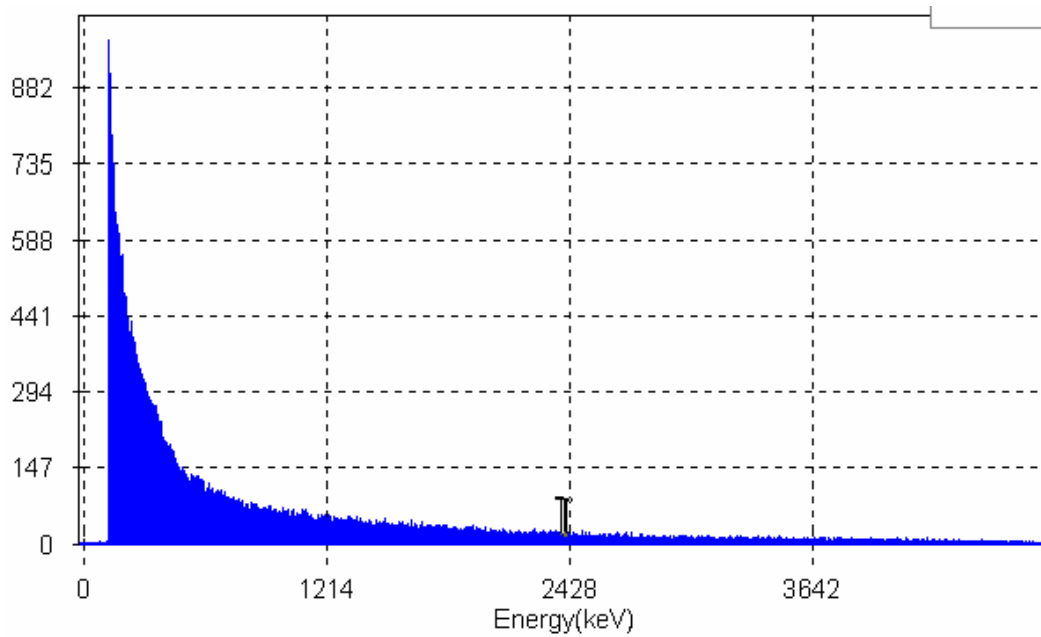
Figure 79: PuBe energy spectrum with minimal amplification (x5)

As the amplification of the DLA (E) increased, the ability to resolve the thermal neutron capture peak improved as shown in Figure 80. This final amplification of x30 was more than enough to clearly distinguish the thermal neutron capture peak from low-level noise.
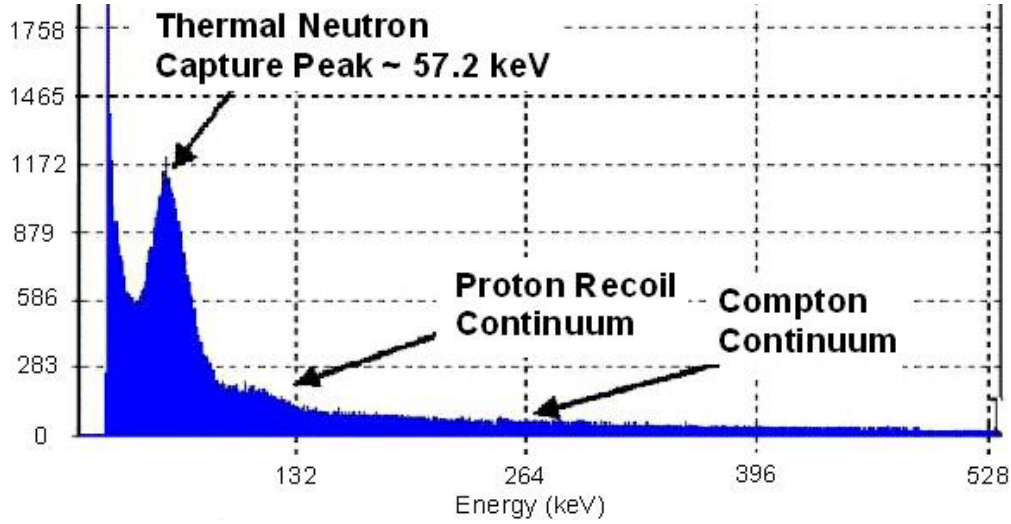
Figure 80: PuBe energy spectrum (x30 amp)

The final amplification of x30 was also chosen because of the ability to calibrate the PuBe source with other reference sources. Due to the linearity of β-particles, which are merely gamma induced Compton scattered electrons, a Cesium-137, Sodium-22, and Manganese-54 source produce a Compton edge(s) from which an energy calibration can be conducted[⊕]. The energy of the expected Compton edge is given as

$$E_{e^-}\Big|_{\theta=\pi} = h\nu\left(\frac{2h\nu/m_0c_2}{1+2h\nu/m_0c_2}\right) \qquad (25)$$

where $h\nu$ = energy of incident gamma (MeV) and m_0c^2 = rest mass energy of electron [9:310].

Cesium-137 produces a γ of 661.7 keV [15:34]. Manganese-54 produces a γ of 834.8 keV [15:25]. Sodium-22 produces both a β+ and a γ. The γ is 1274.5 keV [15:20]. The Na-22 positron creates two 511 keV gammas upon annihilation with an electron, thus with two different γ's it produces two Compton edges[⊕⊕]. The Compton edges of the Cs-137, Mn-54, and Na-22 are detailed in Figure 81 through Figure 83 below.

[⊕] Without the presence of the full photo absorption peak, more error is introduced in the calibration process due to the inability to very accurately locate the *true* Compton edge.
[⊕⊕] Due to the high amplification of the DLA (E), the 1274.5 keV Compton edge created by the Na[22] produced a corresponding voltage pulse >10 V and was off the scale of the MCA. It was not used in calibrating the detector's energy response.
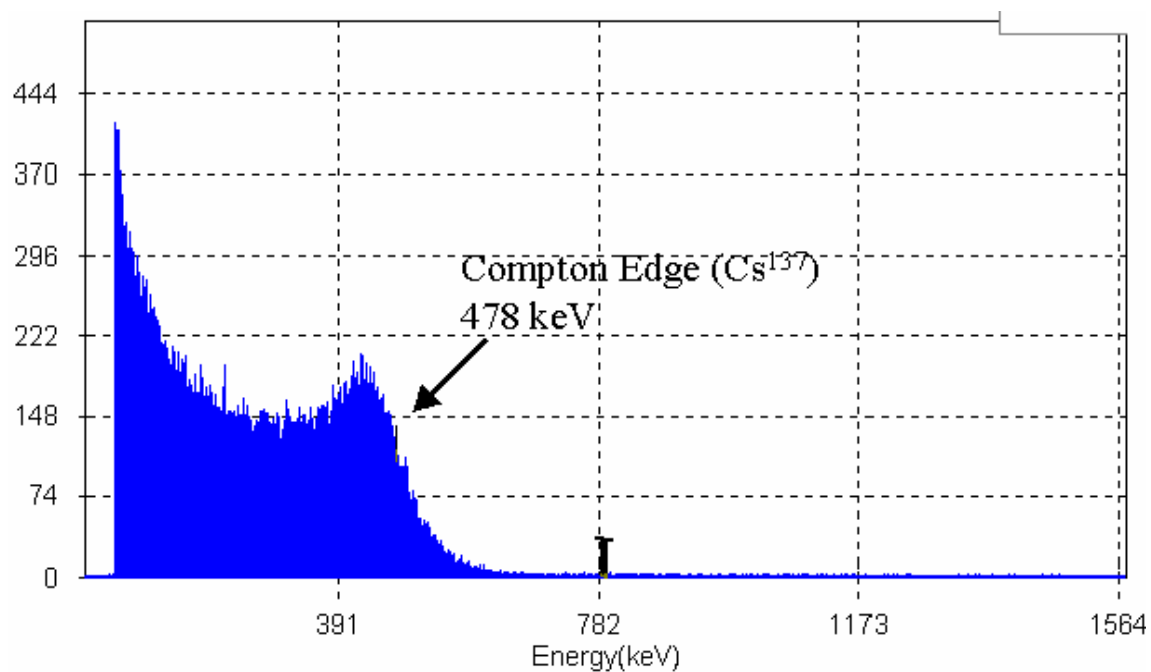
Figure 81: Cs-137 Compton edge
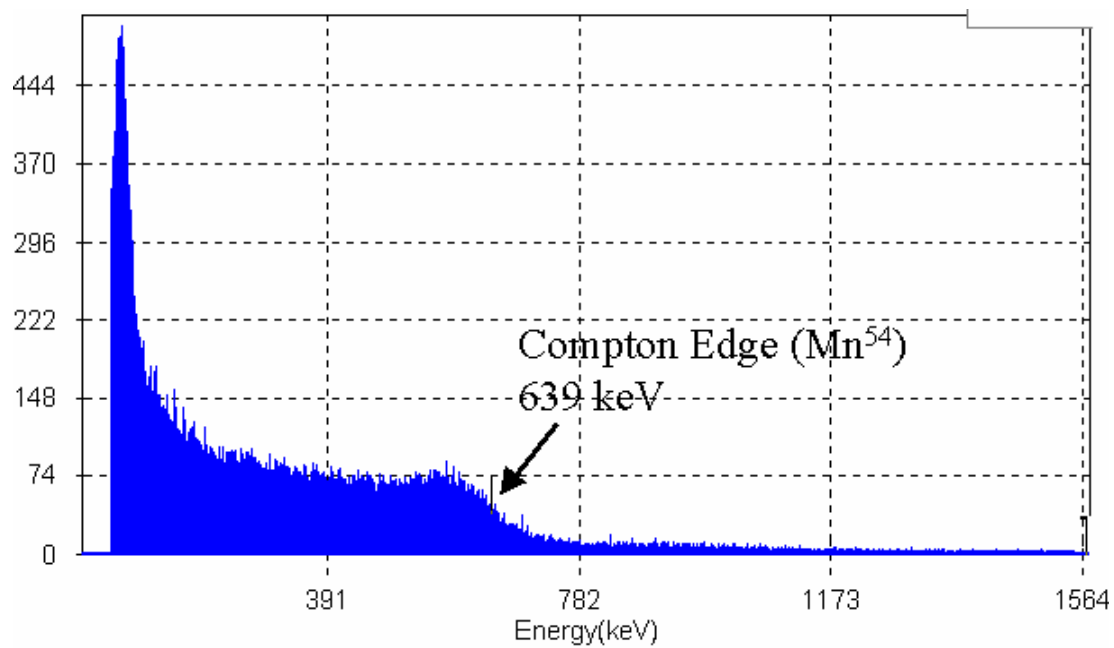
Figure 82: Mn-54 Compton edge

99
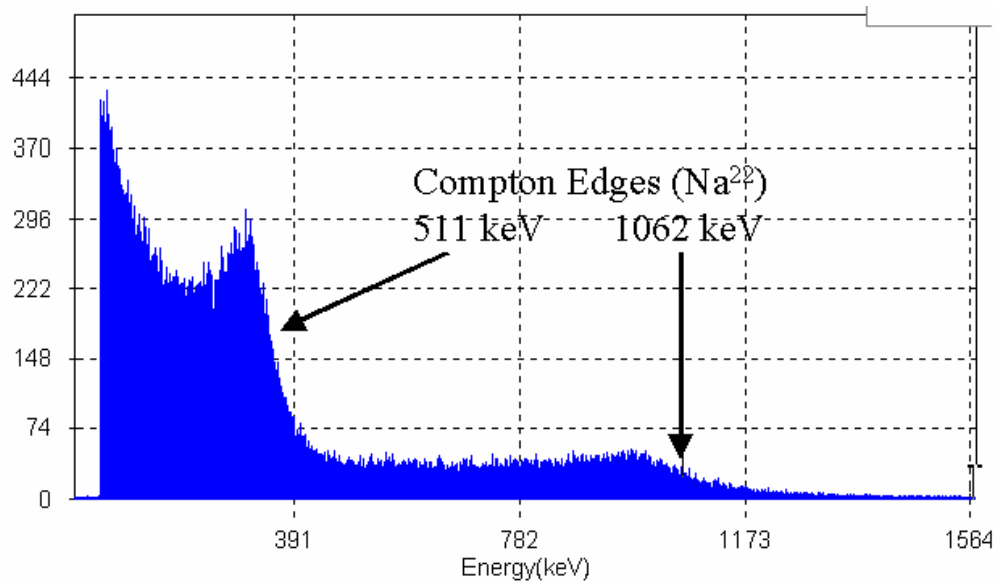
Figure 83: Na-22 Compton edges

Using the "energy only" calibration menu of the MCA software an electron equivalent energy scale was created by which to compare the heavy charged particles created by the neutron events. The linear energy response of the organic scintillator to light charged particles (β-) is evident in MCA energy calibration of Figure 84 below.
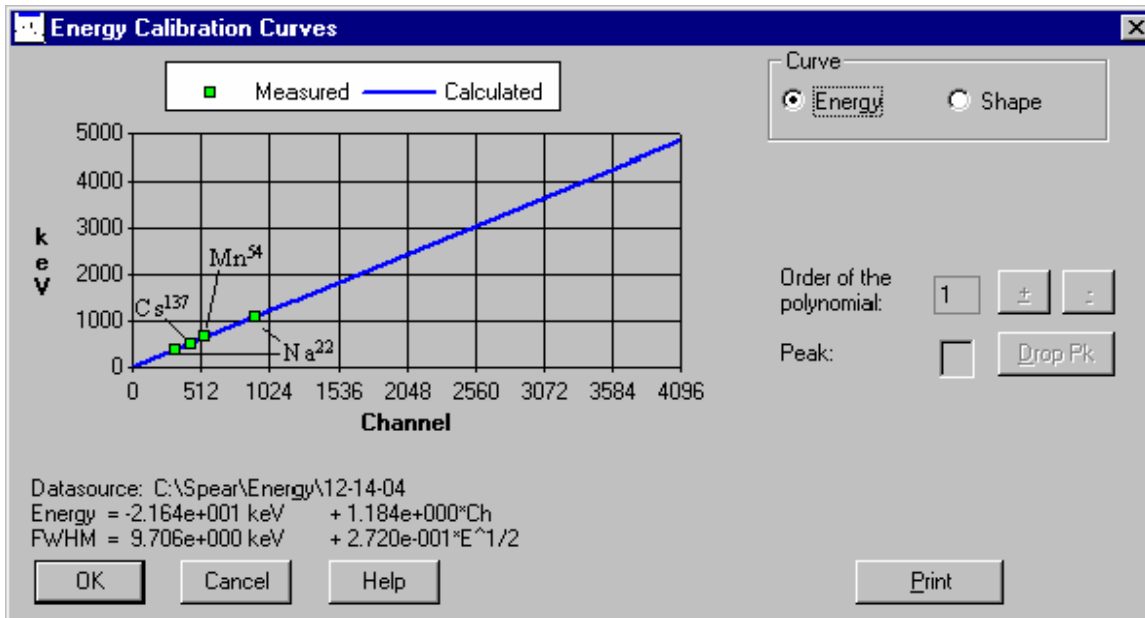
Figure 84: MCA energy calibration output of Cs-137, Mn-54, and Na-22 sources

Appendix G: MATLAB Code

```matlab
%*****************************************************************************
%**Note: This program is designed to read in neutron event .dat files created from**
%**the LeCroy WavePro 7100 Oscilloscope, analyze each time step to determine if    **
%**it is the peak amplitude of a neutron event, then compress the total neutron    **
%**events into the appropriate 10us time bin over the ~3000 us range. This program**
%**requires the timing information gathered from the photodiode .dat file,         **
%**generated one time for each data run. The information is downloaded to Excel    **
%**where further analysis of the raw data for neutron events produces the "forward **
%**edge" spectrum.                                                                 **
%**Version 1 created by Jeff Spear, ENP-05M on 1-12-05                             **
%*****************************************************************************
clc
clear all
close all
Data=[];
Results=zeros(300,2);
q=zeros(300,2);
for j = 1:4
    if (j==1)
        for d = 0:9
            s = ['C20000' int2str(d) '.dat'];
            A=load(s);
            % Code to process the contents of the d-th file
            %Converts the neutron data into 0's and 1's
            B=A; %saves original data for later comparison
            for n=3:25000; %iterates from data cell 3 to 25,000
                if A(n,2)>0.2; %only looks at amplitudes G.T. 200mV (i.e. neutron event)
                    if B(n-1,2) < A(n,2) | B(n-1,2)==A(n,2); %checks if amplitude of current cell is G.T.E. to previous cell
                        if A(n+1,2) < A(n,2) & A(n+2,2) < A(n,2); %checks if value of current cell is G.T. next two cells
                            A(n,2)=1; %if all the above criteria is met (i.e. this is the peak of neutron pulse) assigns value of 1
                        else
                            A(n,2)=0; %if amplitude of current cell is not G.T. next two cells assign value of 0
                        end
                    else
                        A(n,2)=0; %if amplitude of current cell is not G.T.E. to previous cell assign value of 0
                    end
                else
                    A(n,2)=0; %if amplitude of current cell is not G.T. 200mV assign value of 0
                end
            end
            A(1,2)=0;  %assigns 1st cell 0 value
            A(2,2)=0;  %assigns 2nd cell 0 value
            A(25001,2)=0; %assigns 2nd to last cell 0 value
            A(25002,2)=0; %assigns last cell 0 value
            y=A; %returns (25002,2) matrix of timing info and 0's or 1's in former amplitude column

            %redistributes neutron events into 10us time bins ranging from 10-3000us
            i=2000; %cell of neutron data corresponding to peak amplitude of photodiode peak (i.e. 0us start time)
            for n=1:300 %iterates through 10 to 3000 us
                x(n,2)=sum(A(i:i+50,2)); %sums all values over 10us range (50 cells) and assigns to respective time bin
                i=i+50; %steps through each 10us (50 cells)
            end
            x(1:300,1)=0.000010:0.000010:0.003000; %continually sums each neutron data set for a final data set
            if (d==0)
                Data=[Data x];
            else
                Data=[Data x(:,2)];
            end
        end
    end

    if (j==2)
        for d = 10:99
            s = ['C2000' int2str(d) '.dat'];
            A=load(s);
            % Code to process the contents of the d-th file
            %Converts the neutron data into 0's and 1's
            B=A; %saves original data for later comparison
            for n=3:25000; %iterates from data cell 3 to 25,000
                if A(n,2)>0.2; %only looks at amplitudes G.T. 200mV (i.e. neutron event)
                    if B(n-1,2) < A(n,2) | B(n-1,2)==A(n,2); %checks if amplitude of current cell is G.T.E. to previous cell
                        if A(n+1,2) < A(n,2) & A(n+2,2) < A(n,2); %checks if value of current cell is G.T. next two cells
                            A(n,2)=1; %if all the above criteria is met (i.e. this is the peak of neutron pulse) assigns value of 1
                        else
                            A(n,2)=0; %if amplitude of current cell is not G.T. next two cells assign value of 0
                        end
                    else
                        A(n,2)=0; %if amplitude of current cell is not G.T.E. to previous cell assign value of 0
                    end
                else
                    A(n,2)=0; %if amplitude of current cell is not G.T. 200mV assign value of 0
                end
            end
            A(1,2)=0;  %assigns 1st cell 0 value
            A(2,2)=0;  %assigns 2nd cell 0 value
            A(25001,2)=0; %assigns 2nd to last cell 0 value
            A(25002,2)=0; %assigns last cell 0 value
            y=A; %returns (25002,2) matrix of timing info and 0's or 1's in former amplitude column%

            %redistributes neutron events into 10us time bins ranging from 10-3000us
            i=2000; %cell of neutron data corresponding to peak amplitude of photodiode peak (i.e. 0us start time)
            for n=1:300 %iterates through 10 to 3000 us
                x(n,2)=sum(A(i:i+50,2)); %sums all values over 10us range (50 cells) and assigns to respective time bin
                i=i+50; %steps through each 10us (50 cells)
            end
            x(1:300,1)=0.000010:0.000010:0.003000; %continually sums each neutron data set for a final data set
            Data=[Data x(:,2)];
        end
    end

    if (j==3)
        for d = 100:999
```

```
                s = ['C200' int2str(d) '.dat'];
                A=load(s);
                % Code to process the contents of the d-th file
                %Converts the neutron data into 0's and 1's
                B=A; %saves original data for later comparison
                for n=3:25000; %iterates from data cell 3 to 25,000
                    if A(n,2)>0.2; %only looks at amplitudes G.T. 200mV (i.e. neutron event)
                        if B(n-1,2) < A(n,2) | B(n-1,2)==A(n,2); %checks if amplitude of current cell is G.T.E. to previous cell
                            if A(n+1,2) < A(n,2) & A(n+2,2) < A(n,2); %checks if value of current cell is G.T. next two cells
                                A(n,2)=1; %if all the above criteria is met (i.e. this is the peak of neutron pulse) assigns value of 1
                            else
                                A(n,2)=0; %if amplitude of current cell is not G.T. next two cells assign value of 0
                            end
                        else
                            A(n,2)=0; %if amplitude of current cell is not G.T.E. to previous cell assign value of 0
                        end
                    else
                        A(n,2)=0; %if amplitude of current cell is not G.T. 200mV assign value of 0
                    end
                end
                A(1,2)=0;  %assigns 1st cell 0 value
                A(2,2)=0;  %assigns 2nd cell 0 value
                A(25001,2)=0; %assigns 2nd to last cell 0 value
                A(25002,2)=0; %assigns last cell 0 value
                y=A; %returns (25002,2) matrix of timing info and 0's or 1's in former amplitude column

                %redistributes neutron events into 10us time bins ranging from 10-3000us
                %redistributes neutron events into 10us time bins ranging from 10-3000us
                i=2000; %cell of neutron data corresponding to peak amplitude of photodiode peak (i.e. 0us start time)
                for n=1:300 %iterates through 10 to 3000 us
                    x(n,2)=sum(A(i:i+50,2)); %sums all values over 10us range (50 cells) and assigns to respective time bin
                    i=i+50; %steps through each 10us (50 cells)
                end
                x(1:300,1)=0.000010:0.000010:0.003000; %continually sums each neutron data set for a final data set
                Data=[Data x(:,2)];
            end
        end

        if (j==4)
            for d = 1000:3550
                s = ['C20' int2str(d) '.dat'];
                A=load(s);
                % Code to process the contents of the d-th file
                %Converts the neutron data into 0's and 1's
                B=A; %saves original data for later comparison
                for n=3:25000; %iterates from data cell 3 to 25,000
                    if A(n,2)>0.2; %only looks at amplitudes G.T. 200mV (i.e. neutron event)
                        if B(n-1,2) < A(n,2) | B(n-1,2)==A(n,2); %checks if amplitude of current cell is G.T.E. to previous cell
                            if A(n+1,2) < A(n,2) & A(n+2,2) < A(n,2); %checks if value of current cell is G.T. next two cells
                                A(n,2)=1; %if all the above criteria is met (i.e. this is the peak of neutron pulse) assigns value of 1
                            else
                                A(n,2)=0; %if amplitude of current cell is not G.T. next two cells assign value of 0
                            end
                        else
                            A(n,2)=0; %if amplitude of current cell is not G.T.E. to previous cell assign value of 0
                        end
                    else
                        A(n,2)=0; %if amplitude of current cell is not G.T. 200mV assign value of 0
                    end
                end
                A(1,2)=0;  %assigns 1st cell 0 value
                A(2,2)=0;  %assigns 2nd cell 0 value
                A(25001,2)=0; %assigns 2nd to last cell 0 value
                A(25002,2)=0; %assigns last cell 0 value
                y=A; %returns (25002,2) matrix of timing info and 0's or 1's in former amplitude column

                %redistributes neutron events into 10us time bins ranging from 10-3000us
                %redistributes neutron events into 10us time bins ranging from 10-3000us
                i=2000; %cell of neutron data corresponding to peak amplitude of photodiode peak (i.e. 0us start time)
                for n=1:300 %iterates through 10 to 3000 us
                    x(n,2)=sum(A(i:i+50,2)); %sums all values over 10us range (50 cells) and assigns to respective time bin
                    i=i+50; %steps through each 10us (50 cells)
                end
                x(1:300,1)=0.000010:0.000010:0.003000; %continually sums each neutron data set for a final data set
                Data=[Data x(:,2)];
            end
        end
end

Results(:,1)=Data(:,1); %Transfers timing information of Data matrix to final Results matrix

for k=1:300;
    q(k,2)=sum(Data(k,2:3550)); %Sums from 10-3000 us all neutron events for a given 10 us time bin
end

Results=Results+q;
```

Appendix H: Detector Efficiency

Note: The source was considered an isotropic emitter, although an unknown anisotropy factor is associated with the two different axis.

Solid Angle Calculation:

$D_0 = 504.0$; (* Distance between source and detector in mm *)

$s = 10.414$; (* Active radius of sources in mm *)

$a = \left(\dfrac{706.86}{\pi}\right)^{\frac{1}{2}}$ (* Approximate radius of detector *);

$\Omega[\text{d\_}] := \dfrac{4\,\pi\,a}{s}\,\text{NIntegrate}\left[\dfrac{e^{-d\,x}\,\text{BesselJ}[1,\,s\,x]\,\text{BesselJ}[1,\,a\,x]}{x},\,\{x,\,0,\,\infty\}\right]$ (* From Knoll, p119 *)

$\Omega[D_0]$

0.00278

Absolute Efficiency Calculation:

$S = 1.13381*10^7$; (* Estimated neutron flux $\left[\frac{n}{s}\right]$ – See Appendix B: PuBe Source Calculations *)

$R = 324.08$; (* Number of neutron events recorded by detector in 1 second *)

$\epsilon_{abs} = \dfrac{R}{S}$

0.0000285833

Intrinsic Efficiency Calculation:

$\epsilon_{int} = \epsilon_{abs}\left(\dfrac{4\,\pi}{\Omega[D_0]}\right)$

0.129204

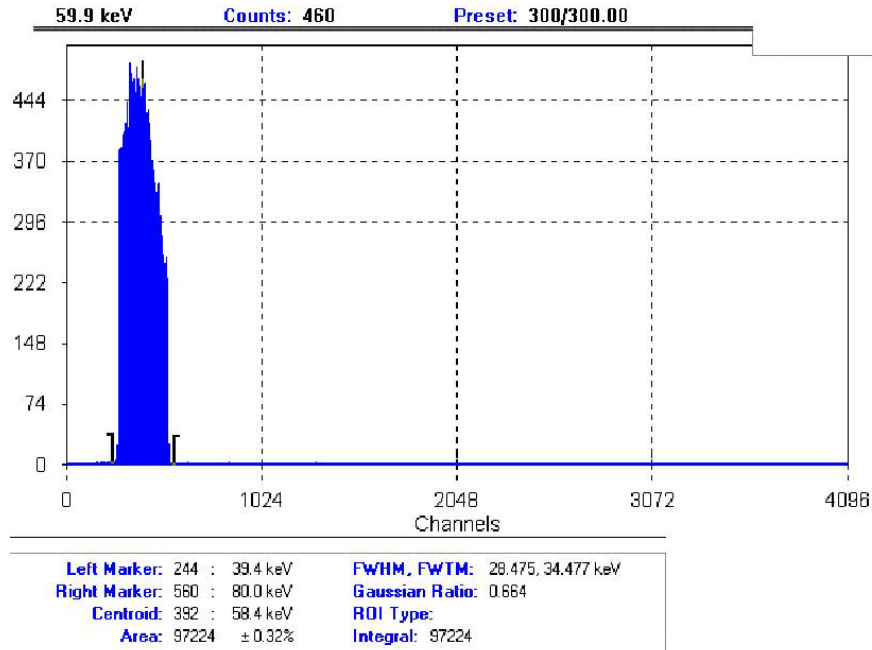Figure 85: Thermal neutron counts used in efficiency calculations

103

$M_{Al} := 0.06024 * 10^{24}$ $(* \frac{atoms}{cm^3} *)$

$\sigma_{T-Al} := 1.72 * 10^{-24}$ (*Total x-sect of thermal neutrons in Al*)

$\Sigma_{T-Al} = M_{Al} * \sigma_{T-Al};$

$\lambda = \frac{1}{\Sigma_{T-Al}}$ "cm"

9.65132 cm

Note: The mean free path of a thermal neutron (0.0253 eV) in Aluminum 6061 is 9.65 cm [35:59].

$\rho_{Air} := 1.293 * 10^{-3} (* \frac{g}{cm^3} *)$

$A_N := 14.0067 (* \frac{g}{mol} *)$

$A_O := 15.9994 (* \frac{g}{mol} *)$

$N_0 := 6.022 * 10^{23} (* \frac{atoms}{mole} *)$

$\sigma_{T-N} := 23.4413 * 10^{-24}$ (*Total x-sect of 0.0005 eV neutron in N*)

$\sigma_{T-O} := 3.89 * 10^{-24}$ (*Total x-sect of 0.0005 eV neutron in O*)

$M_N = \frac{N_0 \, \rho_{Air}}{A_N};$

$M_O = \frac{N_0 \, \rho_{Air}}{A_O};$

$\Sigma_{T-N} = M_N * \sigma_{T-N};$

$\Sigma_{T-O} = M_O * \sigma_{T-O};$

$\lambda = \frac{1}{.8 \, (\Sigma_{T-N}) + .2 \, (\Sigma_{T-O})}$ "cm"

925.617 cm

Note: The mean free path of the slowest neutron (0.00053 eV) in Air is 925.617 cm.

$\rho_{Wax} := 9.3 * 10^{-1} (* \frac{g}{cm^3} *)$

$A_H := 1.00794 (* \frac{g}{mol} *)$

$A_C := 12.0107 (* \frac{g}{mol} *)$

$F_H := 0.143711$ (*By weight fraction of Hydrogen*)

$F_C := 0.856289$ (*By weight fraction of Hydrogen*)

$\sigma_{T-H} := 2.25 * 10^{-24}$ (*Total x-sect for 3.1 MeV neutron in H*)

$\sigma_{T-C} := 1.582 * 10^{-24}$ (*Total x-sect for 3.1 MeV neutron in C*)

$\rho_H = \rho_{Wax} * F_H;$

$M_H = \frac{\rho_H * N_0}{A_H};$

$\Sigma_{T-H} = M_H * \sigma_{T-H};$

$\rho_C = \rho_{Wax} * F_C;$

$M_C = \frac{\rho_C * N_0}{A_C};$

$\Sigma_{T-C} = M_C * \sigma_{T-C};$

$\lambda = \frac{1}{\Sigma_{T-C} + \Sigma_{T-H}}$ "cm"

4.11811 cm

Note: The mean free path of a 3.1 MeV neutron in paraffin (Wax) is 4.11 cm. The MCNP calcuation to find the required thickness of moderation also accounted for attenuation in the active detector volume.

Appendix J: Limit of Rotational Speed

```
r := .09 (*m*)
ρ := 2698.9 (* kg/m³ *)

σ[kips_] = kips (* kips/in² *) * 4448.221 (* (kg*m/s²)/kip *) * 1/0.00064516 (* in²/m² *); (*Pa*)

v[kips_] = √(σ[kips]/ρ) (* m/s *);

ω[kips_] = v[kips]/r (* radians/s *);

RPMs[kips_] = ω[kips] (* rad/s *) * 1/(2π) (* Revolutions/Radian *) * 60 (* seconds/minute *);

RPMs[40] (*Note: 40 kips/in² represents the yield tensile strength*) [36:35]
```

```
33917.6
```

Note 1: Using an 18 cm diameter Alloy 6061 Aluminum Disc allows for a maxium of 33,918 RPM before yield strength is met.

Note 2: The mean free path associated with this type of aluminum alloy (6061) is 9.65 cm, thus nearly two mean free paths exist in the current configuration.

Appendix K: List of Equipment

Make	Model	S/N	Remarks
ORTEC	556 High Voltage Supply	1928	N/A
ORTEC	556 High Voltage Supply	2096	Photodiode supply
Canberra	ND 556 AIM	4F9	N/A
Canberra	9633 ADC	030247	N/A
ORTEC	NIM Bin	N/A	x2
ORTEC	NIM Bin Power Supply 4002D	1751 & 3278	X2
LeCroy	WavePro 7100 Oscilloscope	10258	N/A
ORTEC	542 Linear Gate & Stretcher	1648	LG&S1
ORTEC	542 Linear Gate & Stretcher	1930	LG&S2
ORTEC	551 Timing Single-Channel Analyzer (TSCA)	2271	Energy Branch
ORTEC	551 TSCA	2319	PSA Branch
ORTEC	427 Delay Amplifier	3746	N/A
ORTEC	460 Delay Line Amplifier	1536	Energy Branch
ORTEC	460 Delay Line Amplifier	3210	PSA Branch
ORTEC	552 Pulse Shape Analyzer / TSCA	1141	N/A
ORTEC	566 Time-to-Amplitude Converter	5420	N/A
ORTEC	419 Precision Pulse Generator	1881	N/A
ORTEC	Model 113 Preamplifier	7948	N/A
Saint-Gobain	Model 523A Organic Scintillation Detector	PI077	Boron-Loaded
Sperry	DM-350A Multimeter	N/A	Personally owned
Micron	Pentium III Computer	16285720003	N/A
DeWalt	DW625 Electronic Plunge Cut Router	095848	N/A
Barden	High Precision Bearings	N/A	x3
Statco	3PN1010 Variable Autotransformer	N/A	On loan from fabrication shop
Isotope Products Laboratory	Cesium-137 Source	T-089	10.02 μCi
Isotope Products Laboratory	Manganese-54 Source	T-064	86.3 μCi
Isotope Products Laboratory	Sodium-22 Source	T-106	0.8883 μCi
McMaster-Carr	Aluminum/Stainless Steel construction materials	N/A	See purchase request

Bibliography

1. The White House Office of the Press Secretary, 2002 State of the Union Address. January 29, 2002.

2. Defense Threat Reduction Agency. "Mission Statement." n. pag. http://www.dtra.mil/. 5 July 2004.

3. Department of Defense. DoD General Planning Assumptions for Arms Control Treaties and Agreements, FY 02-07 (Coordination Version 2002) Dec 2001.

4. Benedict, Manson and Pigford, Thomas H. and Levi, Hans W., Nuclear Chemical Engineering. New York: McGraw-Hill Book Company, 1981.

5. Suriano, Mark. "Neutron Leakage Spectra from Outer Surface of 239Pu and 235U spheres and shells". Highspeed Computer Model. Lawerence Livermore National Laboratory. 2003.

6. Allen, William D. Neutron Detection. New York: Philosophical Library Inc., 1960.

7. Kirk, F. W. "Neutron Time-Of-Flight Spectrometers," Nuclear Instruments and Methods, Vol 162, 1979.

8. Cross, William G. and Harry Ing. "Neutron Spectroscopy," The Dosimetry of Ionizing Radiation, Vol. 2, edited by Kenneth Kase. Orlando: Academic Press, 1987.

9. Knoll, Glenn F. Radiation Detection and Measurement. New York: John Wiley & Sons, 2000.

10. Wood, Charles L. Construction, Calibration and Use of a Neutron Time-Of-Flight Spectrometer. MS thesis, AFIT/GNE/ENP/91M-12. Department of Engineering Physics, Air Force Institute of Technology (AU), Wright-Patterson AFB OH, March 1991.

11. Fisher, Harl'O M., A Nuclear Cross-section Data Handbook, LA-11711-M, Los Alamos National Laboratory, Los Alamos, New Mexico, December 1989.

12. Fermi, E., Marshall, J. and Marshall, L. "A Thermal Neutron Velocity Selector and Its Application to the Measurement of the Cross Section of Boron," Physical Review, Vol 72, 1947.

13. Granroth, G.E., Conceptual Design Report for the Multiple Disc Chopper Spectrometer at the Spallation Neutron Source, http://sokol.phys.psu.edu/cncs/Conceptual%20Design%20Report_f.pdf, Oak Ridge National Laboratory, March 2001.

14. Kumar, A. and Nagarajan, P. S. "Neutron Spectra of 239Pu-Be Neutron Sources," Nuclear Instruments and Methods, Vol 140, 1977.

15. Parrington, Josef R., Knox, Harold D., Breneman, Susan L., Baum, Edward M., and Feiner, Frank, editors, Nuclides and Isotopes, 15th Ed. San Jose, California, 1996.

16. Anderson, M. Edward. "Increases in Neutron Yields of Plutonium-Beryllium (α,n) Sources," Nuclear Applications, Vol 4, 1968.

17. Seibyl, Walter L. Radioisotope Training Manual: Part III Neutron Experiments, White Plains, New York: Picker X-Ray Corporation, 1963.

18. http://physwww.physics.mcmaster.ca/phys3h03.res/Neutron%20Moderation/Neutron%20moderation.pdf, December 2004.

19. Beyer, William H. CRC Standard Mathematical Tables, 28th Ed. Boca Raton, Florida: CRC Press, Inc., 1987.

20. Krane, Kenneth S. Modern Physics, 2nd Edition. New York: John Wiley & Sons, 1996.

21. L'Annunziata, Michael F. Handbook of Radioactivity Analysis, 2nd Edition. London: Academic Press, 2003.

22. Turner, James E. Atoms, Radiation, and Radiation Protection, 2nd Ed. New York: John Wiley & Sons, Inc., 1995.

23. http://www.detectors.saint-gobain.com, July 2004.

24. Aoyama, T., Honda, K., and Mori, C., "Energy response of a full-energy-absorption neutron spectrometer using boron-loaded liquid scintillator BC-523", Nuclear Instruments and Methods in Physics Research. Vol. A333, Pg. 492, 1993.

25. Advanced Measurement Technology, Inc. Modular Pulse-Processing Electronics. Oak Ridge, Tennessee, 1999.

26. Advanced Measurement Technology, Inc. Model 460 Delay Line Amplifier Operating and Service Manual. Oak Ridge, Tennessee, 2002.

27. Advanced Measurement Technology, Inc. Model 552 Pulse-Shape Analyzer and Timing Single-Channel Analyzer Operating and Service Manual. Oak Ridge, Tennessee, 2002.

28. Advanced Measurement Technology, Inc. Model 551 Timing Single-Channel Analyzer Operating and Service Manual. Oak Ridge, Tennessee, 2002.

29. Canberra Industries, Inc. Model 9633 Analog-to-Digital Converter User's Manual. Meriden, Connecticut, 1999.

30. DeWalt Industrial Tool Co., Instruction Manual for DeWalt DW625 Electronic Plunge Cut Router. Baltimore, Maryland, 2002.

31. Petrosky, James L. Assistant Professor of Nuclear Engineering, Department of Engineering Physics, Air Force Institute of Technology, Wright-Patterson AFB OH. Personal Interview. 16 December 2004.

32. LeCroy Corporation, WavePro DSO Operator's Manual, Rev C. Chestnut Ridge, New York, 2002.

33. MATLAB. Student Version 6.0, Release 12. Computer software. The Math Works, Inc., Rockville MD, 2001.

34. Monte Carlo N-Particle Transport Code System. Version 4.0, Release C. Computer Software. Radiation Safety Information Computational Center (RSICC), Oak Ridge, Tennessee, 2000.

35. Lamarsh, John R. Introduction to Nuclear Engineering, 3rd Ed. Upper Saddle River, New Jersey: Prentice Hall, 2001.

36. The Aluminum Association. Aluminum Standards and Data, 1st Ed. New York: 1968.

REPORT DOCUMENTATION PAGE

The public reporting burden for this collection of information is estimated to average 1 hour per response, including the time for reviewing instructions, searching existing data sources, gathering and maintaining the data needed, and completing and reviewing the collection of information. Send comments regarding this burden estimate or any other aspect of the collection of information, including suggestions for reducing this burden to Department of Defense, Washington Headquarters Services, Directorate for Information Operations and Reports (0704-0188), 1215 Jefferson Davis Highway, Suite 1204, Arlington, VA 22202-4302. Respondents should be aware that notwithstanding any other provision of law, no person shall be subject to an penalty for failing to comply with a collection of information if it does not display a currently valid OMB control number.
PLEASE DO NOT RETURN YOUR FORM TO THE ABOVE ADDRESS.

1. REPORT DATE *(DD-MM-YYYY)* March 2005	2. REPORT TYPE Master's Thesis	3. DATES COVERED *(From – To)* March 2002 – March 2003

4. TITLE AND SUBTITLE CHARACTERIZING A NEUTRON ENERGY SPECTRUM USING A "FORWARD EDGE" NEUTRON TIME-OF-FLIGHT SPECTROSCOPY TECHNIQUE	5a. CONTRACT NUMBER
	5b. GRANT NUMBER
	5c. PROGRAM ELEMENT NUMBER
6. AUTHOR(S) Spear, Jeffrey S., Major, USA	5d. PROJECT NUMBER 04366
	5e. TASK NUMBER
	5f. WORK UNIT NUMBER

7. PERFORMING ORGANIZATION NAMES(S) AND ADDRESS(S) Air Force Institute of Technology Graduate School of Engineering and Management (AFIT/EN) 2950 Hobson Way, Building 640 WPAFB OH 45433-8865	8. PERFORMING ORGANIZATION REPORT NUMBER AFIT/GNE/ENP/05-14

9. SPONSORING/MONITORING AGENCY NAME(S) AND ADDRESS(ES) Defense Threat Reduction Agency (Attn: 1LT Lakesha Stevenson) 8725 John J. Kingman Road Stop 6201 Fort Belvoir, VA 22060-6201	10. SPONSOR/MONITOR'S ACRONYM(S)
	11. SPONSOR/MONITOR'S REPORT NUMBER(S)

12. DISTRIBUTION/AVAILABILITY STATEMENT

APPROVED FOR PUBLIC RELEASE; DISTRIBUTION UNLIMITED.

13. SUPPLEMENTARY NOTES

14. ABSTRACT
A Fermi-style thermal neutron disc chopper was designed, constructed, and calibrated in conjunction with a boron-loaded organic scintillator for use in creating a *forward edge* neutron time-of-flight spectroscopy technique. The *forward edge* neutron time-of-flight spectroscopy technique inferred the characteristics of a neutron energy spectrum. The system analyzed the spectrum of a moderated and unmoderated PuBe source with the aid of a MATLAB code. Through the use of pulse shape analysis techniques and energy spectroscopy the thermal neutron capture event was identified and isolated. Data analysis provided positive feedback in the disc chopper's ability to partially attenuate higher energy neutrons in the PuBe spectrum. The analyzed data from the MATLAB code indicates the *forward edge* neutron spectroscopy technique works; however, in terms of an application useful for passive interrogation the system's low efficiency and cumbersome size prove too prohibitive.

15. SUBJECT TERMS
Neutron Spectroscopy, Neutron Time-of-Flight, Forward Edge Spectrum

16. SECURITY CLASSIFICATION OF: Unclassified			17. LIMITATION OF ABSTRACT	18. NUMBER OF PAGES	19a. NAME OF RESPONSIBLE PERSON Dr. James C. Petrosky, AFIT-ENP
a. REPORT U	b. ABSTRACT U	c. THIS PAGE U	UU	127	19b. TELEPHONE NUMBER *(Include area code)* (937) 255-6565, ext 4824 (jpetrosky@afit.edu)